Searching for Primordial Gravitational Waves in the B-mode Polarization of the CMB

Benjamin Racine

To cite this version:

Benjamin Racine. Searching for Primordial Gravitational Waves in the B-mode Polarization of the CMB. Cosmology and Extra-Galactic Astrophysics [astro-ph.CO]. Aix-Marseile Université, 2023. tel-04249373

HAL Id: tel-04249373
https://hal.science/tel-04249373v1

Submitted on 19 Oct 2023

NNT/NL : 2020AIXM0001/001ED000

Habilitation à Diriger des Recherches

Soutenue à Aix-Marseille Université
le 14 septembre 2023 par

Benjamin Racine

Searching for Primordial Gravitational Waves in the B-mode Polarization of the CMB

Discipline
Cosmologie (Annexe A)

Spécialité
Univers Primordial et Evolution récente (Annexe A)

Position
Chargé de Recherche Classe Normale

Laboratoire/Partenaires de recherche
Centre de Physique des Particules de Marseille
CNRS/IN2P3

Composition du jury

Sophie Henrot-Versillé IJCLAB	Rapporteur·e
Jim Bartlett APC	Rapporteur·e
Radek Stompor CPB	Rapporteur·e
Jo Dunkley Princeton	Examinateur·rice
Cristinel Diaconu CPPM	Président·e du jury
Dominique Fouchez CPPM	Tuteur

Introduction

In this document, I present my past research about the early Universe using the Cosmic Microwave Background (CMB).

I was very lucky to start my PhD in 2011, just when the first data of the Planck Satellite were beeing analyzed. This was a great introduction to modern cosmology, both in terms of science, Planck being for the past ten years the most important survey, providing the pillars of the current cosmological model, and in terms of environment, Planck being a very large international collaboration, a precursor in our young Era of precision cosmology. After my PhD defense in 2014, I moved to Oslo, at the Institute of Theoretical Astrophysics (ITA) for a first post-doctoral position. I kept working on he Planck data, but also joined a much smaller collaboration, SPIDER, a balloon-borne telescope looking for the primordial B-modes patterns in the polarization of the CMB. I worked both on the development of a new analysis pipeline, as well as some new methods to estimate cosmological parameters. I then moved to the Harvard-Smithsonian Center for Astrophysics (CfA) in Harvard University for a second postdoctoral position, where I joined the Background Imaging of Cosmic Extragalactic Polarization (BICEP) and Keck collaborations, a ground-based telescope at South Pole, with leading measurement in B-mode polarization. I was one of the main contributor to the B-mode cosmology analysis of the BK15 (including all BICEP/Keck data until 2015) paper. We provided the best constraints at the time on the amplitude of primordial gravitational waves. I also joined the CMB-S4 collaboration, which aims at uniting all ground-based CMB projects to reach a factor of 20 improvement in the constraining power. I was one of the most active member of the forecasting working group. Since 2020, I joined the Center of Particle Physics in Marseille (CPPM), where I now work on the recent universe and its accelerated expansion using type-1a Supernovae. I am part of the Vera Rubin Observatory Dark Energy Science Collaboration (DESC) , preparing for the Legacy Survey of Space and Time (LSST). I am also a member of Zwicky Transient Facility (ZTF), working on the photometric calibration of the instrument.

In the current manuscript, I focus on my work on the B-modes science.

The document is organized as follows: In chapter 1 I introduce the standard model of cosmology, in chapter 2 I review the CMB observable and present the experiments I worked on. In chapter 3 I present my work within the SPIDER collaboration on the first part of a data analysis pipeline, from raw data to CMB maps. In chapter 4, I present my cosmological analysis within the BICEP/Keck collaboration, i.e. the next and final stage of the analysis, using power spectra for cosmological inference. At last, in chapter 5, I present my work within the CMB-S4 collaboration, forecasting the measurements of B-modes in the next decade.

Contents

List of Figures

List of Tables

List of acronyms

ACT

Atacama Cosmology Telescope. 82

BICEP

Background Imaging of Cosmic Extragalactic Polarization. 2

BPCM

BandPower Covariance Matrix. 64, 65, 86, 87, 89, 90, 92, 93

CDT

Concept Definition Task force. 84, 88, 95

CfA

Harvard-Smithsonian Center for Astrophysics. 2

CMB

Cosmic Microwave Background. 2, 3, 6, 18–36, 42, 43, 80, 81, 83, 84, 101

CPPM

Center of Particle Physics in Marseille. 2

DOE

Department Of Energy. 84

DSR

Decadal Survey Report. 84, 95

FLRW

Friedmann 1922, Lemaître 1927, Robertson 1935 and Walker 1937. 11, 14

FWHM

Full Width at Half Maximum. 39, 88, 89, 94, 96

ILC

Internal Linear Combination. 85, 92, 94, 103, 105, 106

ITA

Institute of Theoretical Astrophysics. 2

LAT

Large Aperture Telescope. 87, 93–95, 109

NET

Noise-Equivalent Temperature. 85, 87, 89, 90, 95, 96, 100, 107–109

NSF

National Science Foundation. 84

PWV

Precipitable Water Vapor. 36, 88, 109

SAT

Small Aperture Telescope. 85–87, 90, 93, 95, 100, 108, 109

SED

Spectral Energy Distribution. 101, 102

SO

Simons Observatory. 83, 84, 100

SPO

South Pole Observatory. 84

SPT

South Pole Telescope. 37, 82

TOD

Time Ordered Data. 44–52, 54, 56–59, 75

WIMPs

Weakly Interactive Massive Particules. 13

WMAP

Wilkinson Microwave Anisotropy Probe. 19, 35

1 The Standard Model of Cosmology

Sommaire

1.1 Introduction

In this chapter, I will briefly review the current cosmological model. I will also introduce the need for cosmic inflation or other alternatives.

1.2 The Standard Model of Cosmology

At the turn of the 20th century, which saw the development of electromagnetism from Maxwell 1865, the Michelson and Morley 1887 experiment and the death of luminiferous ether theory, as well as the introduction of mathematical concepts from Lorentz 1903, and Poincaré 1906, Einstein introduced special relativity (Einstein 1905), and later general relativity (Einstein 1915; Einstein 1916).

This revolutionary theory was then applied to the Universe's dynamics, with major work from Einstein 1917, de Sitter 1917, Friedmann 1922, or Lemaître 1927. Around the same time, Leavitt and Pickering 1912 observations of the period-luminosity relations of Cepheids, together with Slipher 1915 observations of "nebulae" and the redshifting of their spectra, allowed Hubble 1929 to convince the scientific community of a law linking the redshifts of galaxies to their distances. Lemaître 1931 then interpreted this expansion of the Universe as a result of an initial decay of a "primeval atom", a first version of Big Bang theory.

For a more detail historical background, one can look at my PhD manuscript (Benjamin Racine 2014), or many existing publications.

1.2.1 FLRW and Hubble rate

If we consider a homogeneous and isotropic universe, Friedmann 1922, Lemaître 1927, Robertson 1935 and Walker 1937 (FLRW) showed that one can describe the universe's metric as

$$ds^2 = -dt^2 + a(t)^2 \left[\frac{dr^2}{1-kr^2} + r^2 d\theta^2 + r^2 sin^2\theta d\phi^2 \right], \tag{1.1}$$

where t is the cosmic time, and r, θ are the comoving polar coordinates, $k = -1, 0, 1$ correspond to an open, flat, or closed universe, and $a(t)$ is a dimension-less scale factor, parameterizing the overall expansion of the Universe.

To describe the evolution of this scale factor, one can also define the Hubble rate :

$$H(t) \equiv \frac{\dot{a}}{a} \tag{1.2}$$

The Hubble rate today is noted H_0 and its value has been the subject of debates for a century and is still today (see review in Abdalla et al. 2022).

1.2.2 The Friedmann's equations

Using this metric in Einstein's equations, which describe how matter influences the space time metric (more details in Benjamin Racine 2014), and considering perfect fluids, (solely determined by the pressure and energy density, i.e., with no viscosity, heat conduction, or anisotropic pressure), we get the Friedmann's equations:

$$\left(\frac{\dot{a}}{a}\right)^2 = \frac{8\pi G}{3}\rho + \frac{\Lambda}{3} - \frac{k}{a^2}, \tag{1.3}$$

$$\frac{\ddot{a}}{a} = -\frac{4\pi G}{3}(\rho + 3p) + \frac{\Lambda}{3}, \tag{1.4}$$

where ρ and p are the energy density and pressure of the matter, Λ is the cosmological constant, G is Newton's gravitational constant, and we note $\dot{a} = da/dt$.

1.2.3 Continuity equation and dynamics of perfect fluids

From 1.3 and 1.4, we can derive the continuity equation:

$$\dot{\rho} + 3\frac{\dot{a}}{a}(\rho + p) = 0. \tag{1.5}$$

For a fluid with equation of state $\rho = \omega(z)p$, we can solve the Friedmann's equations, and we obtain:

$$\rho(a) = \rho(a_0) \times \exp\left(-3\int_{a_0}^{a} \frac{da'}{a'}(1+\omega(a'))\right). \tag{1.6}$$

If ω is a constant, we get $\rho(a) = \rho(a_0)\left(\frac{a}{a_0}\right)^{-3(1+\omega)}$. These solutions for different fluids are summarized in table 1.1.

1.2.4 Cosmological redshift

The light emitted from an object will get stretched to higher wavelengths during its propagation in an expanding universe. We note this redshift z:

$$1+z \equiv \frac{\lambda_0}{\lambda_{\mathrm{e}}} = \frac{a_0}{a_e}, \tag{1.7}$$

where λ_0 is the observed wavelength, and λ_{e} is the wavelength at emission. This is this red-shifting of galaxies observed by multiple astronomers in the early twentieth century that allowed them to conclude that the Universe is expanding.

1.2.5 ΛCDM

With the Friedmann's equations introduced earlier, we are able to describe the expansion of the Universe and its history based on its content. In this section, we will describe the main components that drive this expansion.

Baryonic Matter

Baryonic matter is made of the baryons of the standard model of particle physics (and the associated leptons). It represents all the common matter such as atoms, stars or planets. When it is non-relativistic, it is pressure-less, i.e. $\omega = 0$.

Radiation

Radiation corresponds to the relativistic components of the Universe. Early on in history, it includes all components, but when the heavy ones become non-relativistic, we are left with the photons, and the standard neutrinos. In addition to the volume effect on the energy density due to expansion, there is an additional scale factor dependence, as can be intuited for photons, due to the stretching of the wavelength. This corresponds to $\omega = 1/3$.

Component	ω	$a(t)$	$\rho(a)$	$H(t)$
Matter	0	$t^{2/3}$	a^{-3}	$\frac{2}{3t}$
Radiation	1/3	$t^{1/2}$	a^{-4}	$\frac{8}{9t}$
Curvature ($k < 0$)	-1/3	$t^{1/3}$	a^{-1}	$\frac{4}{9t}$
Λ	-1	$e^{H_0 t}$	a^0	H_0
ω	ω	$t^{\frac{2}{3}(1+\omega)}$	$a^{-3(1+\omega)}$	$\frac{2}{3}\frac{1+\omega}{t}$

Table 1.1: Solutions to the Friedmann's equation for a few components.

Dark Matter

Dark Matter corresponds to the non-baryonic matter, which doesn't interact via the electromagnetic force, and is thus non visible. It was introduced by multiple people in order to explain the dynamics of stars in the Milky Way, or of galaxies in clusters, for instance by Oort 1932 and Zwicky 1933, and more clearly by Rubin et al. 1978 using the galaxy rotation curves. It has since then also been revealed by gravitational lensing observations, where the reconstructed mass doesn't correspond to the visible mass (bullet cluster, Clowe et al. 2004). It is also needed to explain the structures of our Universe on large scales. Many candidates exist, for instance Weakly Interactive Massive Particules (WIMPs), primordial black holes, sterile neutrinos, or some modified gravity theories. Observations suggest that this component is "cold", i.e. non-relativistic, and pressure-less, as baryonic matter: $\omega = 0$.

Dark Energy

Dark Energy is a form of repulsive energy with negative pressure, which has been postulated to explain the accelerated expansion of the Universe, observed with high confidence by Riess, Filippenko, et al. 1998 and Perlmutter et al. 1999. To obtain such an expansion, we need a fluid with $\omega < -1/3$.

So far, our Universe seems to be well described by the simplest dark energy model, the cosmological constant Λ, with $\omega = -1$. Ongoing projects are studying this modern acceleration with high precision to challenge this hypothesis. This is in the core of my studies at CPPM but will not be described in this manuscript.

1.2.6 Cosmological Parameters

The evolution of the scale parameter and hence of the expansion history of the Universe depends on the density of the different components of the Universe. We express this with respect to the critical energy density:

$$\rho_c \equiv \frac{3}{8\pi}\frac{H^2}{G}\,. \tag{1.8}$$

These density parameters $\Omega_i = \rho_i/\rho_c$, as well as the contribution of curvature and Λ, $\Omega_k = -\frac{k}{H^2a^2}$ and $\Omega_\Lambda = \frac{\Lambda}{3H^2}$, can be used to re-write Friedman's first equation (1.3) as :

$$\left(\sum_i \Omega_i + \Omega_k + \Omega_\Lambda\right) = 1\,. \tag{1.9}$$

If we define $\Omega_{i,0} = \Omega_i\Big|_{a=a_0}$, we can show that

$$\Omega_i = \Omega_{i,0}\left(\frac{H_0}{H}\right)^2 \exp\left(-3\int_{a_0}^{a}(1+\omega(a'))da'/a'\right), \tag{1.10}$$

and for ΛCDM, we can rewrite equation (1.11) as:

$$H(a)^2 = H_0^2\left(\Omega_{m,0}\left(\frac{a}{a_0}\right)^{-3} + \Omega_{r,0}\left(\frac{a}{a_0}\right)^{-4} + \Omega_{k,0}\left(\frac{a}{a_0}\right)^{-2} + \Omega_{\Lambda,0}\right). \tag{1.11}$$

1.3 Early Universe Physics and initial conditions

In the last section, we reviewed briefly the standard model of cosmology. In this section, we review some aspects of early Universe physics.

1.3.1 Limits of the standard model

If we imagine running the standard model backward in the context of General Relativity, we would encounter a singularity, where quantities would become infinite and the laws of physics would break down. New physics is then needed to avoid these conditions.

Even if we elude this question and consider the Big Bang scenario, other issues arise, which I developed in more details in my PhD manuscript.

- **The Horizon problem**: In a FLRW universe, the size of the causally connected regions is given by the particle horizon, i.e. Hubble radius $R_H \equiv |1/H| = |a/\dot{a}|$ and we can show that at the time of decoupling, this size is much smaller than the size of our observable Universe: in the CMB, this would means that regions distant by more than $\simeq 1.7\,\mathrm{deg}$ have never been in causal contact. This is in contradiction with the fact that the temperature of the CMB is the same in the whole sky (within 10^{-5} relative fluctuations, as explained in the next chapter).

- **The flatness problem**: In a radiation or matter dominated universe, aH decreases, and as we see in 1.2.6, the curvature then increases. To reach the flatness observed today, one would need an extremely flat initial condition.

A recent paper by Peebles reviews other anomalies in physical cosmology (Peebles 2022).

1.3.2 Solutions

Since the work reported in the current document is observational, this introduction aims at being synthetic and pedagogical, but is of course very limited and will not be discussing the rich and sometimes highly debated[1] theoretical and philosophical details. It would be better to remain theory unbiased, even if this is not always the case in the rest of the manuscript.

1.3.2.1 Inflation

Inflation is a period of extremely rapid growth of the size of the Universe (for a nice review on inflation, see Baumann 2009). This growth is due to a scalar field, the inflaton, with potential V, whose dynamics drives the Universe to quasi de Sitter space (similarly to the Dark Energy period, see table 1.1). At the end of inflation, the inflaton field couples to ordinary matter and radiation fields, in a reheating phase. This end of inflation is in some sense the hot Big Bang described above.

It was introduced in the 1980s (Alan H. Guth 1981; Linde 1982; Starobinsky 1980) and is the most popular scenario to solve the issues of the standard model. Both issues above are linked to the increase of the Hubble radius. During the accelerated expansion of inflation, this Hubble radius shrinks and drives Ω_k towards 0. It also means that at early time, the region encompassed in this very small Hubble radius was in causal contact.

It was also realized by Mukhanov and Chibisov 1981 that quantum fluctuations during inflation could be the seeds of the structures we observe in our Universe. These perturbations affect the inflaton field altogether with the metric of space time itself (see Riotto 2002). Perturbations of the metric can be of scalar, vector and tensor type. In simple models of inflation, there is no vorticity, thus no vector perturbations. We can formulate the scalar perturbation in terms of the comoving curvature perturbations $\mathscr{R}$, and introduce the power spectrum of scalar perturbations Δ_s, here following the notations of Baumann 2009:

$$\langle \mathscr{R}_k \mathscr{R}_{k'} \rangle = (2\pi)^3 P_{\mathscr{R}}(k) \delta(\boldsymbol{k} + \boldsymbol{k}'), \qquad \Delta_s^2 \equiv \frac{k^3}{2\pi^2} P_{\mathscr{R}}(k) \tag{1.12}$$

We can here introduce the spectral index n_s and its running α_s:

$$n_s - 1 \equiv \frac{d \ln \Delta_s^2}{d \ln k}, \qquad \alpha_s \equiv \frac{d n_s}{d \ln k} \tag{1.13}$$

---

[1] See for instance this article in scientific American, and the answer from the Planck team and others.

The tensor fluctuations h are ripples of space time that can be interpreted as gravitational waves. We can also introduce their power spectra:

$$\langle h_k h_{k'} \rangle = (2\pi)^3 P_h(k)\delta(\boldsymbol{k}+\boldsymbol{k}'), \qquad \Delta_t^2 \equiv 2\frac{k^3}{2\pi^2}P_h(k) \tag{1.14}$$

where the factor of 2 comes from the fact that gravitational waves have two degrees of freedom, i.e. two polarization modes, "+" and "×". We can define:

$$n_t \equiv \frac{d\ln\Delta_t^2}{d\ln k}, \qquad \alpha_t \equiv \frac{dn_t}{d\ln k} \tag{1.15}$$

We can then rewrite these power spectra as:

$$\Delta_s^2 = A_s\left(\frac{k}{k_0}\right)^{n_s-1+1/2\alpha_s\ln(k/k_0)+\dots}, \qquad \Delta_t^2 = A_t\left(\frac{k}{k_0}\right)^{n_t+1/2\alpha_t\ln(k/k_0)+\dots}, \tag{1.16}$$

where we did not write the higher orders beyond α. k_0 is a pivot frequency, and the amplitudes, tilts and running of the tilt will depend around what pivot scale we define the power spectrum, we did not write this dependence for simplicity. k_0 is often taken as 0.05Mpc^{-1} or 0.002Mpc^{-1}.

We usually quantify the amplitude of the tensor modes relatively to the scalar modes, using the scalar-to-tensor ratio r:

$$r \equiv \frac{\Delta_t^2(k)}{\Delta_s^2(k)}, \tag{1.17}$$

which will also depend on the pivot scale.

Note that the equations above are not specific to inflation, but describe any primordial scalar and tensor perturbations. In my thesis, I derived these expressions for slow-roll inflation and made quantitative predictions for quadratic inflation (which we now ruled out as I explain in chapter 4, where we also show other models in figure 4.7). Note that non-linear evolution of scalar perturbation will also produce tensor modes, estimated to be subdominant if $r > 10^{-6}$ (Mollerach et al. 2004).

1.3.2.2 Problems of Inflation

We will not here pretend to understand in any depth the very large number of publications discussing the inflationary framework. Some of the issues mentioned here can probably be solved in some of the specific models of inflation, but might loose simplicity. We will just mention some of the issues with some non-exhaustive citation of the literature. There are also some good summaries by Caroll or on Wikipedia.

While inflation will flatten the Universe, we still need the small patch in which it started to be flat and homogeneous enough (Ijjas and Paul J. Steinhardt 2016), which is related to the entropy problem from (Penrose 1989). There is also no prediction of the amplitude of density fluctuation (Ijjas et al. 2014). We thus require some fine-tuning (see also Gibbons and Turok 2008). Another problem arises from the fact that in some classes of inflation models the initial states of inflation can be at energies beyond the Planck scale, for which we don't have a good physical theory (see for instance Robert Brandenberger and Peter 2017).

Another issue is that in an inflating universe, the inflaton field itself fluctuates, which means that some parts of the Universe will transition towards a reheating period, while some other parts will keep inflating and dominate the Universe, in which the same phenomenon occurs. This is referred to as the eternal inflation. This was realized by multiple people, in 1983, quickly after inflation was introduced (see Alan H Guth 2007 for a modern review). This produces an infinity of "pocket" universes, and predictions in this multiverse are hard to define.

1.3.2.3 Some alternatives

While inflation is the most popular early universe framework, alternatives have been proposed. A class of models solves most of the hot Big Bang issues together and avoid the singularity problem, with a bounce. For these non-singular bounces, the hot Big Bang is preceded by a slow contraction of the Universe, with an equation of state ω larger than 1, and the Hubble radius decreases fast. Most of the issues of the hot Big Bang and of inflation can be resolved in that case (for a pedagogical introduction, see Ijjas and Paul J Steinhardt 2018, and discussions in Robert Brandenberger and Peter 2017). Many variants of these bouncing models have been studied, and arise from string theory: for instance the ekpyrotic/cyclic model (Khoury et al. 2001), the string gas (R. Brandenberger and Vafa 1989), the matter bounce (Finelli and Robert Brandenberger 2002), and the pre Big Bang (Gasperini and Veneziano 1993) models.

2 Cosmic Microwave Background observations

Sommaire

In this chapter, we will introduce a few specificities of CMB observations, as well as the experiments I worked on since my PhD. In the first section, we will summarize the known microwave foreground emissions, focusing on the polarized ones.

2.1 CMB emission

In the Big Bang theory, introduced in the previous chapter, the Universe was once filled by a photo-baryon plasma, where the ionized matter was interacting with radiation via Thomson scattering. Due to the expansion, the Universe cooled down to a temperature low enough ($T \simeq 3000K$) for the proton and electron to recombine. At the end of the recombination, around 380000 years after the Big Bang (and $z \simeq 1100$), the Universe became transparent. We receive today photons from this last scattering surface, redshifted to $\simeq 3K$.

2.1.1 CMB frequency spectrum

All the interactions in the plasma kept the photons in thermal equilibrium, with an almost perfect[1] black-body spectrum, following the Planck law:

$$\frac{2h\nu^3}{c^2}\frac{1}{e^{h\nu/k_B T}-1} \tag{2.1}$$

where h is the Planck's constant, c is the speed of light, and k_B is the Boltzmann constant. For the CMB, the temperature was measured in 1990 by the COBE FIRAS instrument and the latest analysis gives $T_{\rm cmb} = 2.72548 \pm 0.00057K$ (Fixsen 2009).

Note that this intensity, usually measured as a surface brightness per solid angle in MJy/sr, can be converted to a temperature. Since the CMB follows a black-body spectrum, its temperature uniquely defines the intensity. This is not the case for the other sky emissions. They can still be converted to thermodynamic temperature (K_{CMB} or simply K in this manuscript) or brightness temperature (K_{RJ}) (see BeyondPlanck Collaboration 2020 for a discussion on these units). Unless specified, we will use thermodynamic temperatures in this manuscript.

2.1.2 CMB temperature anisotropies

While the temperature of the CMB is extremely uniform on the sky, there are fluctuations at the level of $T \simeq 10^{-5}K$. These were observed for the first time by the DMR instrument of the COBE satellite (Smoot et al. 1992). Since then it has been measured in greater details by the Wilkinson Microwave Anisotropy Probe (WMAP) and Planck.

2.1.2.1 The CMB temperature power spectrum

To describe the temperature anistropies[2] of the CMB on the sky, we use the spherical harmonics decomposition:

$$T(\theta,\phi) = \sum_{\ell=0}^{\infty}\sum_{m=-\ell}^{\ell} a_{\ell m} Y_{\ell m}(\theta,\phi)\,. \tag{2.2}$$

where ℓ is a multipole, inversely proportional to the angular scale on the sky (angle $\simeq 2\pi/\ell$), and m describes the orientation and shape of the orbital (m is an integer

---

[1] Note that there is a whole sub-field of CMB research using spectral distortions away from the black-body from energy injections pre-recombination (see for instance Chluba et al. 2021)

[2] Here we note $T(\theta,\phi)$ as the temperature anisotropies, to be added to the $T_{\rm cmb}$ mean temperature.

running from $-\ell$ to $+\ell$). If the CMB is Gaussian, all the information is contained in the variance of the spherical coefficients, or angular power spectrum C_ℓ:

$$C_\ell = \langle |a_{\ell m}|^2 \rangle = \frac{1}{2\ell+1} \sum_{m=-\ell}^{\ell} a_{\ell m} a^*_{\ell m}. \tag{2.3}$$

This is the power spectrum of the "observed" CMB and even if we had access to this signal without any noise, we would only have access to one realization of the Universe, and we would not have access to the real ensemble average of these modes. This uncertainty $\mathrm{Var}(C_\ell) = \frac{2}{2\ell+1} C_\ell^2$, is known as cosmic variance.

Note also that we only have access to a limited part of the CMB sky (due to actual limited observable part of the sky from the ground, but also even in the case of a satellite, from masking strong polluting sources, like the galactic plane). We also observe with an instrument with a beam that will only be sensitive to some modes. In that case, we cannot average over all possible modes and we call the resulting spectrum a *pseudo-power spectrum*. We will see in the next chapter how this can complicate the analysis.

2.1.2.2 Origin of the anisotropies

Let us start with scalar and tensor curvature perturbations in the very early Universe, following a nearly scale invariant power spectrum, as introduced in 1.3.2.1. These perturbations will be transferred during rehearing to other fields like the radiation, matter, or dark matter fields. Gravity will start to pull more matter towards over-densities, but this will enhance the radiative pressure on the baryonic matter, which will have a repulsive effect. The primordial plasma then starts to oscillate with spherical "sound" waves around over-densities. While the causal horizon increases, after the hot Big Bang, larger and larger modes of the density field will start oscillating. The CMB is a picture of these Baryon Acoustic Oscillations (BAO) at the last scattering surface. At recombination, the horizon scale corresponds to roughly one degree on the sky (see horizon problem in chapter 1), i.e. a multipole of $\ell \simeq 200$. Larger scales did not have time to oscillate for a full period, and very large scales are not affected by the BAO, and are directly mapped from the initial perturbations. The temperature power spectrum is mostly seeded by the scalar fluctuations and we can write[3]:

$$C_\ell = \frac{2}{\pi} \int dk k^2 \Delta_\ell^2(k) P_{\mathscr{R}}(k), \tag{2.4}$$

where $P_{\mathscr{R}}(k)$ is the scalar power spectrum, from equation 1.12, which depends on primordial universe physics, and $\Delta_\ell^2(k)$ is the transfer function, which contains the physics of the BAO, the geometry, and the energy content of the Universe. Altogether, this makes the CMB an ideal probe of the early Universe and the ΛCDM model in general. In my thesis manuscript, I described in greater details the physical interpretation

---

[3] Lin and Wandelt 2006 derives this for scalar and tensor contributions.

of the features of the CMB power spectrum. For a much more detailed review, see Dodelson and Schmidt 2020 or Baumann 2009.

2.1.3 CMB polarization

One of the main aspect of this manuscript is the study of the polarization of the CMB. We will here introduce some basic concepts about polarization. For a much better and more detailed review, see Dodelson and Schmidt 2020 or Hu and White 1997.

2.1.3.1 The stokes parameters

To describe polarization, we can use the Stokes parameters. If we have an electromagnetic wave with frequency ω, with time varying electric fields $\boldsymbol{E_x} = E_{0x}\cos(\omega t + \phi_x)$ and $\boldsymbol{E_y} = E_{0y}\cos(\omega t + \phi_y)$, we can define:

$$\begin{aligned} I &\equiv \langle E_{0x}^2\rangle + \langle E_{0y}^2\rangle & (2.5)\\ Q &\equiv \langle E_{0x}^2\rangle - \langle E_{0y}^2\rangle & (2.6)\\ U &\equiv 2\langle E_{0x}E_{0y}\cos(\phi_x - \phi_y)\rangle & (2.7)\\ V &\equiv 2\langle E_{0x}E_{0y}\sin(\phi_x - \phi_y)\rangle\,. & (2.8) \end{aligned}$$

I is the intensity of the radiation, Q and U represent the linear polarization, seen in two coordinate systems rotated by 45 degrees, and V is the circular polarization[4]. A schema of these definitions and some conventions is shown in figure 2.1.

Note that under a parity flip, i.e. a reflection about the x-axis, Q is unchanged, whereas U changes sign. Note also that Q and U are coordinate dependent: under a rotation of the coordinate system by an angle ϕ around the z-axis, they transform as a spin-2 field:

$$Q' = Q\cos 2\phi + U\sin 2\phi \qquad U' = -Q\sin 2\phi + U\cos 2\phi \tag{2.9}$$

Note also that the International Astronomical Union (IAU) defines the polarization angle as zero at north and measured east of north, but in the CMB papers and codes, traditionally it is defined east from south, which means that U_{IAU}=-U_{HEALPIX} (Krzysztof M. Gorski et al. 1999). This can be really confusing.

We can also define the polarization vector $\boldsymbol{P}$ (see for instance Kosowsky 1996), with length $P = \sqrt{Q^2 + U^2}$ and angle $\psi = 1/2\tan^{-1}(U/Q)$. Note that because Q and U are spin-2, α and $\alpha + \pi$ are equivalent: only the orientation of the polarization is defined, not its direction. This is why later on we will show maps with headless vectors to represent the polarization.

---

[4] Note that typically, the CMB is not circularly polarized, i.e. $V = 0$. Some constraints have been made both by SPIDER and CLASS collaborations (Padilla et al. 2020; Nagy et al. 2017), where mechanisms to produce such signals are discussed.

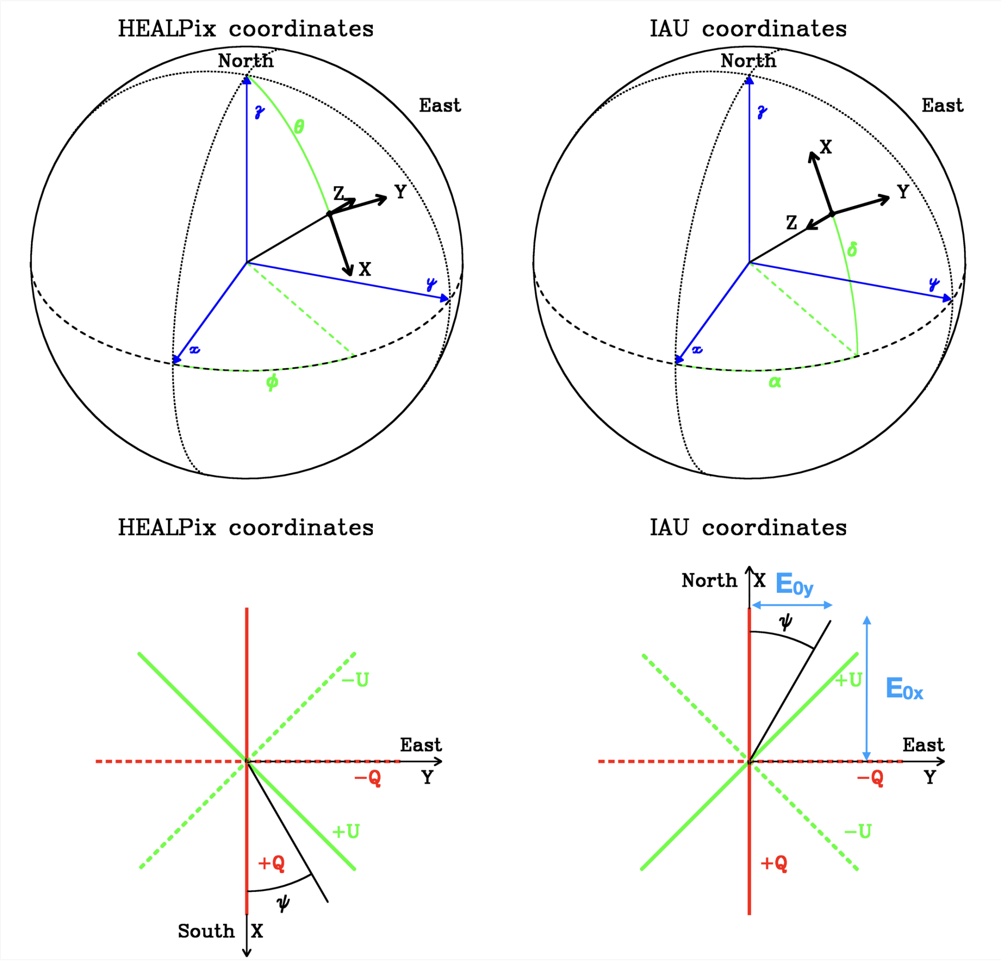

Figure 2.1: On the top, we show the how the coordinate system is defined on the sphere, in the bottom we define Q and U with respect to this system. For `HEALPix` (IAU), the x-axis points southwards (northwards). Figure modified from Krzysztof M. Gorski et al. 1999.

To describe these spin-2 fields on the sphere, similarly to equation 2.10, we can use spin-2 spherical harmonics for the Q and U fields:

$$(Q \pm iU)(\theta,\phi) = \sum_{\ell=0}^{\infty} \sum_{m=-\ell}^{\ell} {}_{\pm 2}a_{\ell m} \, {}_{\pm 2}Y_{\ell m}(\theta,\phi)\,. \tag{2.10}$$

2.1.3.2 The E and B-mode decomposition

As we have seen above, the Stokes parameters are a great basis to describe polarization, but they are defined with respect to a local coordinate system and are not rotationally invariant. As introduced in Zaldarriaga and Uroš Seljak 1997 (see also Uros Seljak and Zaldarriaga 1996), another way to represent this polarization is using the E-mode and B-mode decomposition.

$$a^E_{\ell m} = \frac{{}_{+2}a_{\ell m} + {}_{-2}a_{\ell m}}{2} \tag{2.11}$$

$$a^B_{\ell m} = i\frac{{}_{+2}a_{\ell m} - {}_{-2}a_{\ell m}}{2}\,. \tag{2.12}$$

As shown more explicitly in the review by Kamionkowski and Kovetz 2015 (see also Dodelson and Schmidt 2020), in the flat-sky approximation, we can introduce a tensor field at a position $\boldsymbol{\theta} = (\theta_x, \theta_y)$:

$$\mathscr{P}_{ij} = \frac{1}{\sqrt{2}} \begin{pmatrix} Q(\boldsymbol{\theta}) & U(\boldsymbol{\theta}) \\ U(\boldsymbol{\theta}) & -Q(\boldsymbol{\theta}) \end{pmatrix} \tag{2.13}$$

Taking its gradient and curl, they get E and B modes,

$$E(\boldsymbol{\ell}) = \cos 2\phi_\ell Q(\boldsymbol{\ell}) + \sin 2\phi_\ell U(\boldsymbol{\ell}) \tag{2.14}$$

$$B(\boldsymbol{\ell}) = -\sin 2\phi_\ell Q(\boldsymbol{\ell}) + \cos 2\phi_\ell U(\boldsymbol{\ell}), \tag{2.15}$$

for a wave of wave-vector $\boldsymbol{\ell}$, at an angle ϕ_ℓ with the x-axis. E-modes are a scalar field of even parity, whereas B-modes are a pseudo-scalar fields of odd parity[5]. In the case where $\phi_\ell = 0$, i.e. a wave aligned with the x-axis, a pure E-mode will have $E = Q$ and a pure B-mode will have $B = U$, as shown in figure 2.2.

When multiple wave are superimposed, they can form complicated polarization patterns. In figure 2.3, we show a superposition of planar waves with same amplitude but different angle ϕ_ℓ. This will form a radial wave in the x-y plane.

2.1.3.3 Polarization from Thomson scattering

During the first phase of the Universe, the photons and baryons interact via Thomson scattering (or Compton scattering, see note in Dodelson and Schmidt 2020). In a

---

[5] A flip about the x-axis means $Q \to Q$, $U \to -U$, $\phi_\ell \to -\phi_\ell$, so $E \to E$ and $B \to -B$

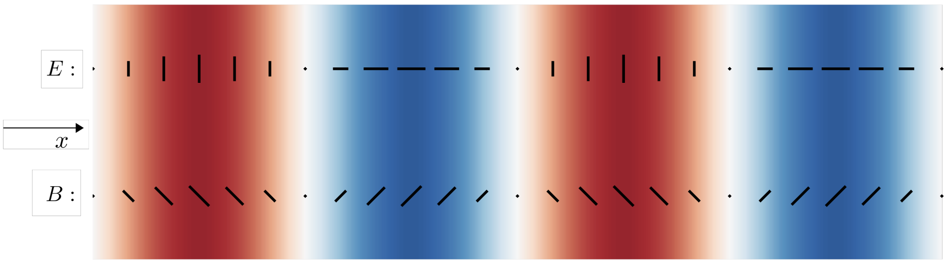

Figure 2.2: Polarization pattern (the lines with length P and angle ϕ) coming out of the page from an E-mode and B-mode plane wave along the x-axis. As seen in equation 2.14, E-mode will then alternate between +Q and -Q, whereas B-modes will alternate between +U and -U. Figure inspired by Dodelson and Schmidt 2020.

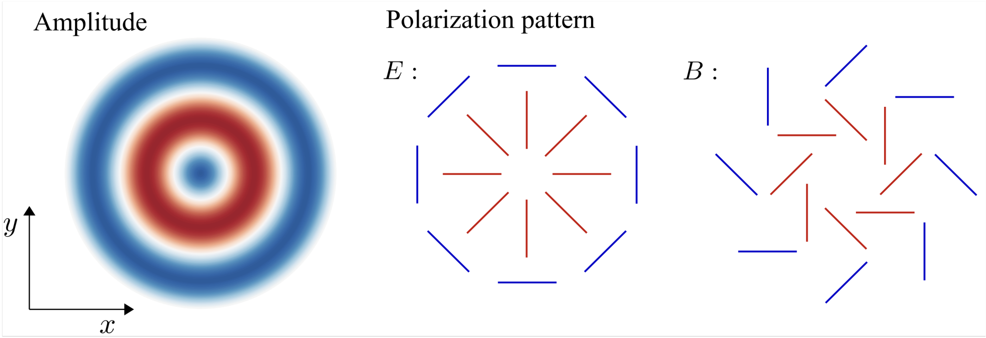

Figure 2.3: Polarization pattern (the lines with length P and angle ϕ) generated from a radial E-mode and B-mode plane wave in the x-y plane. As in figure 2.2, the polarization is for a wave coming out of the page. We see again that for E-modes, the angle is aligned with the minimum of the wave. Figure adapted from Dodelson and Schmidt 2020.

simplistic way, we can imagine that a photon will carry an electric and magnetic field, and that a free electron will then oscillate in the direction of the electric field and re-emit photons. As we can see in figure 2.4, for a single wave coming from the x-direction, a wave emitted in the z-direction will appear polarized. For an isotropic "monopole" radiation, the outgoing radiation is unpolarized. But in the case of a quadrupolar pattern, the outgoing waves are going to be polarized, with a polarization aligned with the direction of the less energetic radiation.

2.1.3.4 Physical origin of the polarization of the CMB at recombination

We just saw how quadrupolar anisotropies in the temperature of the radiation around a photon at last scattering can polarize the light. Here we will show how such quadrupole arise at the last scattering surface. For an intuitive review of how the polarization is generated, see Hu and White 1997.

As we saw in section 2.1.2, the temperature of matter at recombination fluctuates. Let us go back to a simple case with a plane wave of temperature in the x-direction. A photon sitting in a cold trough will see a quadrupolar anisotropy with a rotational symmetry along the x-axis. This quadrupole corresponds to a spherical harmonics with $\ell = 2$, $m = 0$. In figure 2.5, we show what this harmonic looks like, and the polarized angle for different observed angles. If we have a plane wave of temperature fluctuation crossing the surface of last scattering, we will have a polarized emission aligned with the cold troughs, and perpendicular to the hot hills, this will create a pure E-mode similar to figure 2.2. For a given wave, the polarized amplitude will depend on the angle at which it crosses the surface (it will be 0 for a wave coming towards us).

For a random field like the temperature of the CMB, the generated polarization patterns will look like the ones seen in figure 2.3 around hot and cold spots. This means that the E-modes will be spatially correlated with the temperature of the CMB. This E-mode polarization originating in primordial scalar fluctuations has been detected for the first time by the Degree Angular Scale Interferometer (DASI) instrument at South Pole (Kovac et al. 2002).

The other potential source of polarization of the CMB comes from the tensor perturbations. As mentioned in chapter 1, these gravitational waves carry two polarizations, the "+" and the "×" type (for a review of why these two degrees of freedom, see the great review by Tiec and Novak 2017). In figure 2.6, we show how such polarization modes move free falling particles.

These primordial gravitational waves are still present during the recombination. They will compress and stretch space perpendicular to the propagation of the wave, which corresponds to a quadrupole described by $Y_{2\pm2}$. In figure 2.7, we show these spherical harmonics viewed at different angles and the corresponding observed polarization. If we have a gravitational (plane) wave crossing the last scattering surface, a "+"-polarized wave will generate horizontal and vertical polarization patterns along the propagation direction, but a "×"-polarized one will generate patterns that break

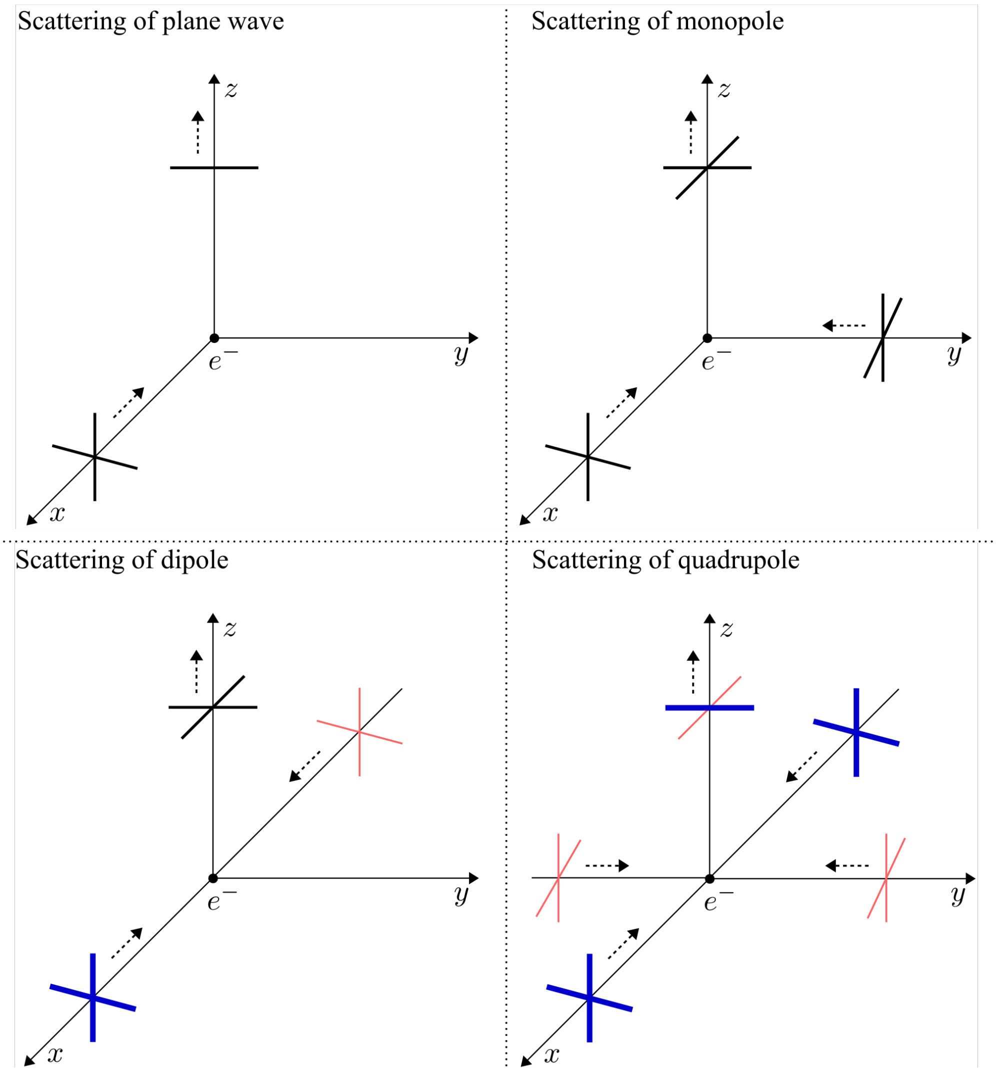

Figure 2.4: On the top left we see the polarized effect on a single wave. On the right, we see that isotropic light (here shown with only two waves), will not produce any polarization. On the bottom left, we see that in the case of a dipolar pattern. Photons coming from -x are less energetic compared to the average radiation, not drawn here, and the ones coming from +x are more energetic. Then the electron will still on average move as much in the x and y-direction. But on the bottom right, we see the quadrupolar case, where the electron will move more in the x-direction, due to the wave coming from the y-direction, than in the y-direction. This will result in a linearly polarized wave in the z-direction. Figure extracted from Dodelson and Schmidt 2020.

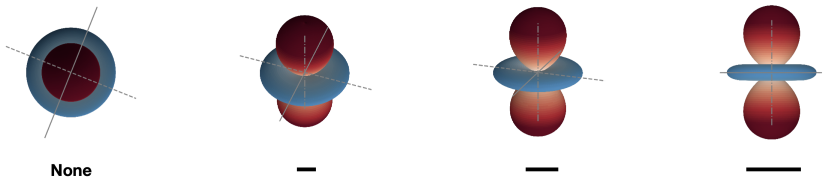

Figure 2.5: Spherical harmonics Y_{20}, due to a scalar temperature perturbation. This is for an electron sitting in a cold trough. The red lobe represents the hot photons, and the blue is for the cold photons. Note the azimuthal symmetry. The outcoming polarized light is aligned with the cold direction. We show how the observed polarization amplitude is modulated depending on the observing angle here for 0, 20, 45 and 90 degrees.

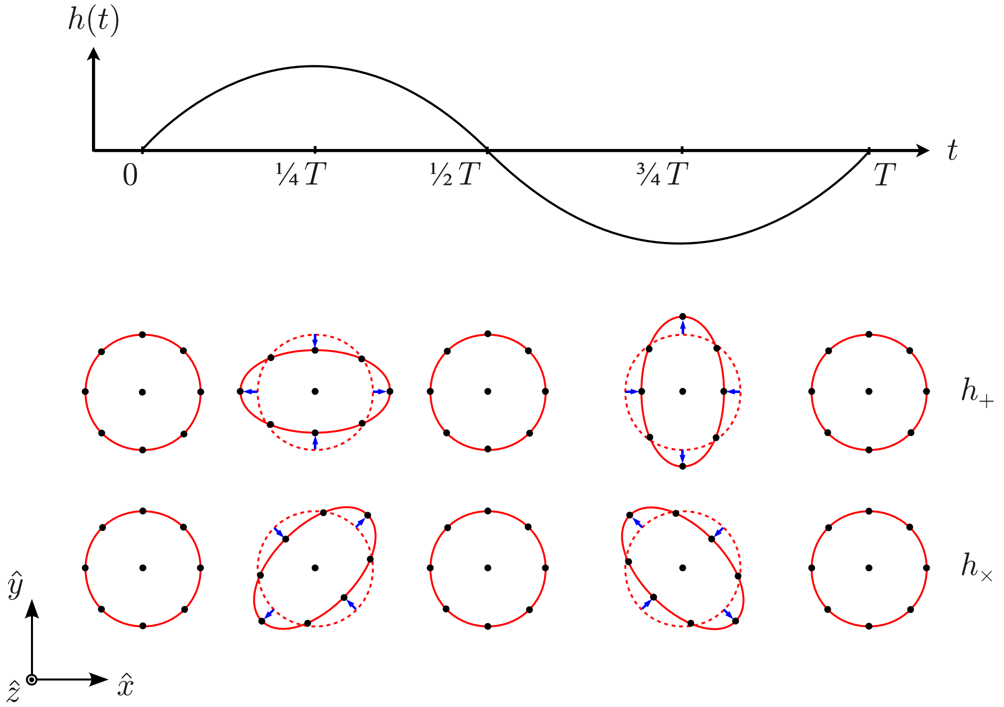

Figure 2.6: Monochromatic gravitational wave, propagating along the z direction, out of the page, with pulsation $\omega = 2\pi/T$. On top, the value of the displacement, or strain, as a function of time. In the bottom, we see an exaggerated case of how free falling particles are displaced in the case of a "+" (along the x- and y-axis) and a "×" type (along x=y and x=-y) polarization. Figure from Tiec and Novak 2017.

this symmetry[6] and generate B-modes as in figure 2.2. In reality, we have multiple waves interfering and we end up with patterns like the right one seen in 2.3.

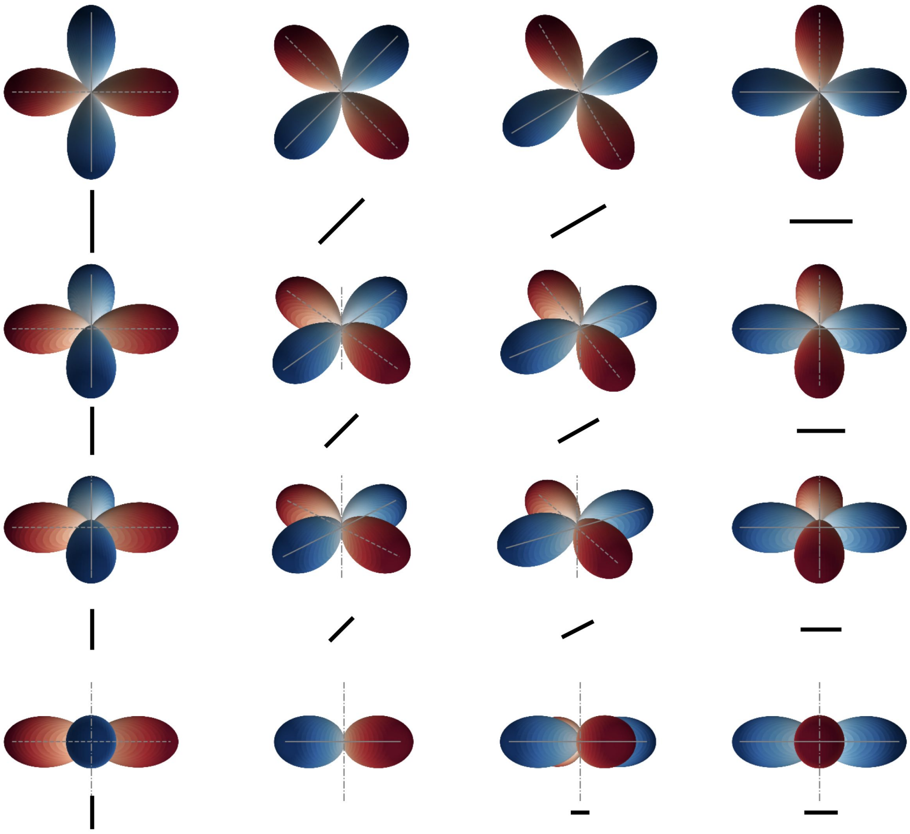

Figure 2.7: Spherical harmonics Y_{22}, due to a gravitational wave. The red lobe represents the compressed "hot" photons, and the blue is for the "cold" photons. Note that there is no azimuthal symmetry anymore. The outcoming polarized light is aligned with the cold direction. We show how the observed polarization amplitude is modulated depending on the observing angle here for an elevation and an azimuth of 0, 45, 60 and 90 degrees.

2.1.3.5 Physical origin of the polarization of the CMB after recombination

Once the CMB photons are emitted, they will travel until we can observe them. They will interact with the rest of the universe in multiple ways, two of which are important for polarization.

---

[6] Note that this will only happen if the wave is crossing the last scattering surface at a non-zero angle, otherwise we will be in the no-polarization case of figure 2.7.

Reionization

After the recombination, the Universe is mostly filled with neutral hydrogen. But as the matter overdensities grow under gravitational forces, the density and energy becomes so important that thermonuclear reactions will start, and the first generation of stars will emit light. The ultraviolet light will break the hydrogen atoms and "re-ionize" the Universe. The free electrons will interact with the surrounding radiation. Due to the expansion of the Universe, the density of free electron is not comparable to the time of recombination and not all photons will interact. This is related to the so-called optical depth to reionization, which is one of the six parameters needed in ΛCDM.

A given free electron will scatter photons from its own CMB sphere, which will have anisotropic fluctuations. Similarly to our own CMB, it can be decomposed on a spherical harmonic basis, and $\ell = 2$ quadrupole component will act as described above, and the scattered photon will be linearly polarized. Once again, temperature fluctuations will only produce a $m = 0$ quadrupole, while primordial gravitational waves will produce $m = \pm 2$ quadrupoles (see for instance Hu 2000[7]). The size of the fluctuation will be determined by the time at which the reionization happened (this is well explained in the thesis by Sébastien Fromenteau 2010), and we can show that $\ell_{\mathrm{reio}}^{\mathrm{obs}} \simeq \sqrt{z_{\mathrm{reio}}}$, i.e. very large scales, since Planck finds an average reionization redshift between 7.8 and 8.8 (Planck Collaboration Int. XLVII 2016).

Gravitational lensing

Along their journey to us, the CMB photons also experience the gravitational field from the structures of our Universe. The line of sight gravitational potential Φ will distort the CMB T, Q and U fields as:

$$\begin{pmatrix} T \\ Q \\ U \end{pmatrix}_{\mathrm{lensed}} (\boldsymbol{\theta}) = \begin{pmatrix} T \\ Q \\ U \end{pmatrix} (\boldsymbol{\theta} + \boldsymbol{\delta\theta}) \simeq \begin{pmatrix} T \\ Q \\ U \end{pmatrix} (\boldsymbol{\theta}) + \boldsymbol{\delta\theta} \nabla \begin{pmatrix} T \\ Q \\ U \end{pmatrix} (\boldsymbol{\theta}) \tag{2.16}$$

where $\boldsymbol{\theta} = (\theta, \phi)$, and $\boldsymbol{\delta\theta} = \nabla(\Phi)$. This means that gravitational lensing will shuffle the fields around. In the T and E-modes field, this can be seen as a smoothing of the harmonic peaks in the power spectra. But another effect is a distortion of the E-mode patterns that will break the symmetry described above. Since the E and B-mode decomposition is orthogonal, any departure from this symmetry leaks to the B-modes. This will create the so-called lensing B-modes (for a computation of the effect, see Lewis and Challinor 2006, and a simple example in flat sky in Kamionkowski and Kovetz 2015).

We will see in the next chapters that we are now entering an era where the lensing contribution will dominate over the primordial signal. The solution is to perform

---

[7] as well as Wayne Hu's lecture notes : `http://background.uchicago.edu/~whu/Courses/Ast448_18/ast448_2.pdf`

"delensing". The modern method uses high-sensitivity, high-angular resolution CMB polarization maps to estimate Φ as well as a low noise E-mode map to predict the B-mode lensing map, which we can subtract from the observed B-modes (Knox and Song 2002; Uros Seljak and Hirata 2004; Carron et al. 2017; Carron and Antony Lewis 2017).

2.1.3.1 The CMB polarization power spectrum

As for the temperature, we can compute the $a^E_{\ell m}$ and $a^B_{\ell m}$ and the auto- and cross-power spectra. Note that in the model described here, the primordial B-modes are independent from all other fields, so we expect the TB and EB power spectra to be zero. On the other hand, the E-modes are correlated to the temperature as described above. In figure 2.8, we show the power spectra for a simple cosmology ($H_0 = 67.5$ km/s/Mpc, $\Omega_b h^2 = 0.022$, $\Omega_b h^2 = 0.122$, $m_\nu = 0.06$eV, $\Omega_k = 0$, $\tau = 0.06$, $A_s = 2 * 10^{-9}$, $n_s = 0.96$). We also show the corresponding maps in figure 2.9. Note that we show the map as would be in theory. In practice the beam of the instrument, the noise, the foregrounds will be present, as we will see next). Smoothed maps are shown for instance in Kamionkowski and Kovetz 2015, where the E and B polarization patterns are even more obvious.

2.2 CMB foregrounds

When observing the CMB, we are poised with other emissions (see figure 2.10). In this section, we will focus on the polarized emissions, which is somehow simpler than the intensity emissions (which are summarized for instance in Planck Collaboration X 2015).

2.2.1 Polarized dust

Dust grains are solid particles in the interstellar medium (ISM), of various size (but typically $0.1\mu m$), produced mostly from exploded stars and are the seeds of planets and other solid bodies[8]. They scatter UV radiation from stars and re-emit in far-infrared. Most grains have oblong shapes and rotate along their short axis, while they emit light with electric field along the long axis. They are also paramagnetic and tend to align with the local magnetic field, which induces a linearly polarized signal (Lazarian and Draine 2000, or see BeyondPlanck Collaboration 2020 and Svalheim et al. 2020 or for a nice summary). While the emissions of the dust grains depend on many things like their temperature, their size, shape, composition etc., it is common to model the dust as a modified black-body law:

---

[8] This talk by Brandon Hensley is a good introduction: `https://www.cita.utoronto.ca/items/rethinking-nature-interstellar-dust/`

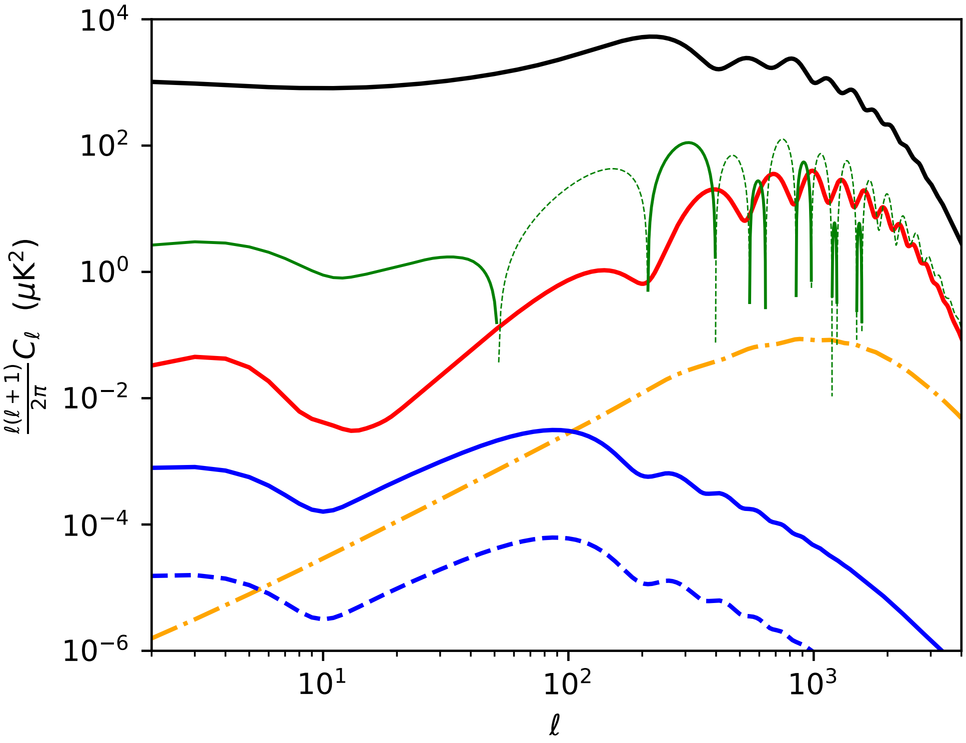

Figure 2.8: CMB power spectrum generated using `CAMB` (A. Lewis et al. 2000). In black we show the TT power spectrum, in red EE, and in green TE (the negative part in dashed thin lines). For the tensor modes, we show in blue the BB power spectrum for $r = 0.001$ (full) and $r = 0.05$ (dashed) and in yellow we show the $r = 0$ lensing contribution. We see the polarization bump due to reionization at very low ell.

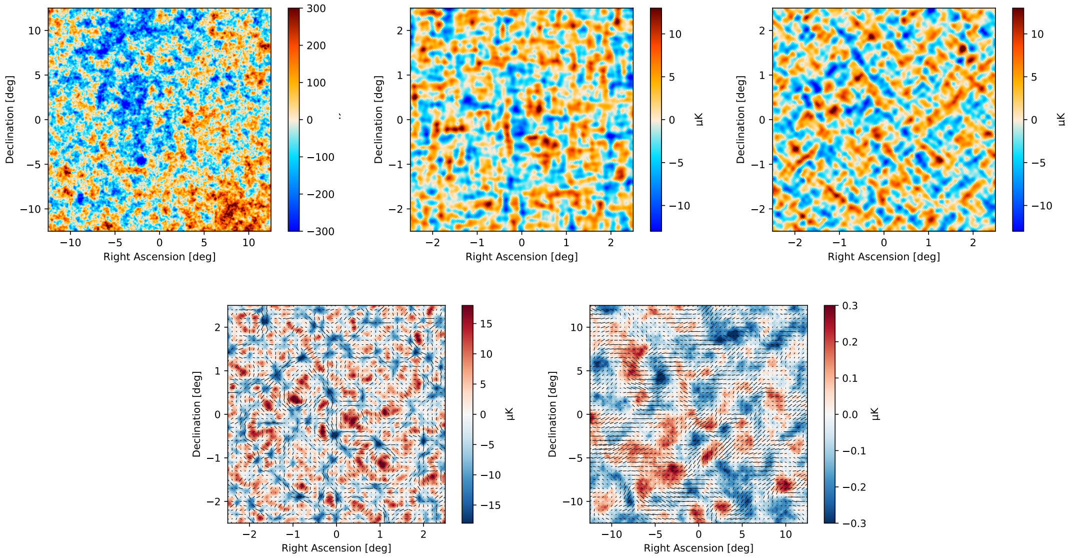

Figure 2.9: CMB maps generated from the power spectrum of figure 2.8, using `healpy` (Zonca et al. 2019; K. M. Gorski et al. 2005). On the top row, T, Q and U maps, on the bottom E and B maps. T, Q, U and E are here generated from scalar fluctuations (B=0), while B is a pure B map (E=0, r=0.1). Note the different scales, both in temperature and in size. We set the color scale extrema to roughly three times the standard deviation of the maps ($\sigma(T) \simeq 100\mu K$, $\sigma(Q) = \sigma(U) \simeq 4\mu K$, $\sigma(E) \simeq 6\mu K$,$\sigma(B) \simeq 0.1\mu K$). Since the temperature and B-modes maps have most power at degree scale, we show a 25 per 25 degrees map, while Q, U and E are mostly at smaller scale so we show a 5 by 5 degrees map. The diagonal U and horizontal/vertical Q are typical of a E map. We can also see the radial polarization patterns around E extrema, and curly ones around B extrema.

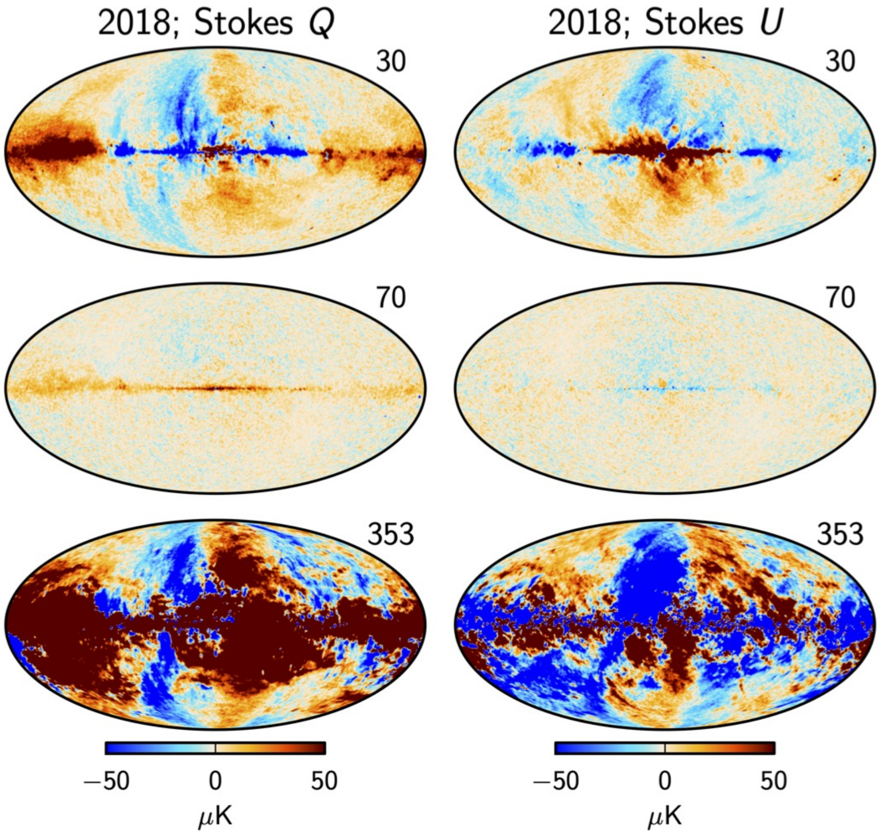

Figure 2.10: Q and U maps at 30, 70 and 353 GHz. We clearly see a strong emission at low frequency, due to polarized synchrotron emission, and at high frequency, due to dust emission. At 70 GHz, we are near the foreground minimum and it is mostly located in the galactic plane. Part of the noise-like features away from the galactic plane is the polarized CMB. Extracted from Planck Collaboration 2020a.

$$s_d(\nu) = A_d \left(\frac{\nu}{\nu_0}\right)^{\beta_d+1} \frac{e^{h\nu_0/k_B T_d} - 1}{e^{h\nu/k_B T_d} - 1} \tag{2.17}$$

where A_d is the amplitude of the emission (which can vary along the line of sight), β_d is the spectral index ($\beta_d \simeq 1.5$), T_d is the temperature of the dust, usually taken around 20K (in BICEP/Keck modeling we will use 19.6K). ν_0 is the reference or pivot frequency (which will be 353 GHz on our later analysis).

Even in this simplified model, the dust temperature can change due to changes in the local radiation of a given dust cloud. This means that the dust emmission on different part of the sky will be different. This creates what is called dust decorrelation. This means that even if we had a perfect measurement of a dust polarization at a given frequency, we could not extrapolate it to other frequencies with the simple model above. This can complicate the component separation.

While Planck Collaboration Int. L 2016 claimed a detection of such decorrelation using Planck data at 217 and 353 GHz, Sheehy and Slosar 2017 found no evidence using the same data. Later on, Planck Collaboration 2020b found no evidence using a multi-frequency analysis.

As we will see in chapter 4, we did not find any evidence for dust decorrelation in BICEP/Keck data.

While the galactic dust emission is obviously not isotropic and is expected to be non-Gaussian, it seems like when restricting to the diffuse emission far from the galactic plane, it is well described by an angular power spectrum modelled as a power law: $C_\ell = A_d(\ell/\ell_{\text{pivot}})^{\alpha_d}$ (with $\alpha_d \simeq -2.4$, see Planck results on polarized dust[9]: Collaboration et al. 2014).

2.2.2 Polarized Synchrotron

Synchrotron emission is due to relativistic electrons (mostly ejected by Supernovae) spiralling in our Galaxy's magnetic fields (Rybicki and Lightman 1985). These electrons emit light in the acceleration direction and it is linearly polarized. As reviewed for instance in BeyondPlanck Collaboration 2020, the emission law depends on the energy distribution of the electrons which is itself a power law. Therefore we model it as:

$$s_s(\nu) = A_s \left(\frac{\nu}{\nu_0}\right)^{\beta_s} \tag{2.18}$$

where A_s is the amplitude of the emission and β_s is the power law index ($\beta_s \simeq -3$) and ν_0 is the pivot frequency (which will be 23 GHz in our later analysis). Note that some more complex models have been used in the literature with a curved power law (eg. BeyondPlanck Collaboration 2020).

The spatial distribution of cosmic ray electrons, as well as some line of sight effects could also create varying spectral indices of the synchrotron , causing some

---

[9] Note that these results are on C_ℓ whereas in the BK analysis, we use D_ℓ, and $\ell_{\text{pivot}} = 80$.

decorrelation of the signal (see Krachmalnicoff et al. 2018).

As shown in Krachmalnicoff et al. 2018, similarly to the case of polarized dust, synchrotron can be well approximated with a power law angular power spectrum.

2.2.3 Component separation

Since these foregrounds can mimic some of the cosmological signals we are looking for, one of the main efforts in the CMB community is to perform component separation, where CMB emission is disentangled from foreground emissions, using observations at multiple frequency bands. In figure 2.11 we show a summary of the CMB and polarized foreground emissions. This would deserve its own chapter but here we will refer for instance to the different Planck papers (eg. Planck Collaboration 2020a).

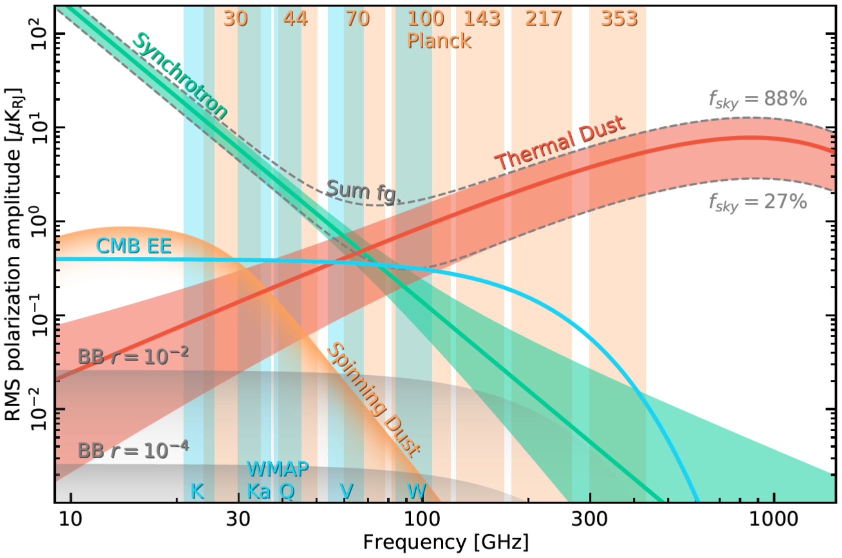

Figure 2.11: Foreground emission in terms of polarization amplitude root mean square (RMS) as a function of frequency, vertical bands indicate the frequency ranges of Planck and WMAP. The dust and synchrotron bands limits correspond to different masking of the highest emissions, as constrained by the Beyond Planck project, from which this figure is taken (BeyondPlanck Collaboration 2020). The cyan CMB line is the best fit EE emission from Planck. The expected BB emission is shown for two values of r (note that we are here in "map RMS space" not in "power spectrum" space). The spinning dust is using an upper limit from the Beyond Planck collaboration.

2.2.4 Atmosphere

One of the other difficulties of observing the CMB is due to the atmosphere (see Errard et al. 2015 for instance). It has several effects[10]:

- Opacity: the oxygen is not transparent at microwave frequencies. There is a large absorption band form oxygen around 60 GHz, an oxygen line around 119 GHz and some water vapor lines around 22, 183, 325, and 380 GHz (Errard et al. 2015). Above 100, there is also a continuum from water vapor.
- Loading: for bolometric detection, which we will summarize briefly in section 2.3, we are limited by photon noise, which is dominated by the Poisson fluctuation in the number of photons (shot noise). The CMB black-body itself will be a source of loading, as well as the instrument emission. But for ground-based telescopes, the main external source of noise is the atmosphere[11]. It will be proportional to the emission of the atmosphere, which can be very roughly estimated as a black-body, multiplied by the opacity. For a typical opacity of 5 percent and $T_{\mathrm{atm}} = 250K$, we have an equivalent background emission of order $10K$.
- Correlated noise: temporal and spatial variations of the atmosphere emission will produce noise in the observed time ordered data, which will dominated over the signal on large scales. This is the $1/f$ noise discussed in the next chapter (see equation 3.10).

This is the main reason why ground-based telescopes observing bands are limited to a few typical frequency windows (see for instance figure 2.15 for the SPIDER coverage or 5.4 for CMB-S4)

To mitigate these effects, there are three options. One is to go to space, where there is no atmosphere. There all frequencies are accessible, and the noise is reduced to CMB and instrument loading, such that one detector in space is equivalent to roughly 100 detectors on the ground. Another option is to send balloon-borne experiments to avoid most of the atmosphere, this is what we will see with SPIDER next. The other option is to stay on the ground but look for a place with low Precipitable Water Vapor (PWV), i.e. a dry, cold, high altitude site, to have less atmosphere and as stable as possible to reduce variations of the correlated noise. As we will see in chapter 5, the current main observing sites are in the Atacama desert in Chile and at the South Pole.

---

[10] Note that it depends also on the elevation of the telescope and the corresponding airmass we observe through. See for instance this posting we made for CMB-S4: http://bicep.rc.fas.harvard.edu/CMB-S4/analysis_logbook/20190220_S4_NET_forecasts_III/

[11] See for instance a typical loading from a BK-like instrument computed using NETLib.py, which we will use in chapter 5 here: http://bicep.rc.fas.harvard.edu/dbarkats/postings/NET_calculator/NET_details.html.

2.3 The BICEP/Keck experiments

The South Pole Amundsen-Scott Station provides an ideal environment for radio and microwave observations. It is one of the driest place on earth, at more than 2800 meters, and with a really stable atmosphere during the winter night, when it can continuously observe from March to November.

At this exquisite site, the telescopes from the BICEP/Keck (BK) collaboration are targeting the large scale B-modes, using refractive telescopes with a beam of roughly half a degree (depending on frequency and/or the aperture size and optical design of the telescopes). The whole optical elements are in a helium cryostat at 4K, and the whole telescope rotate around the boresight every 2 days to modulate the incoming polarization and disentangle it from polarization generated within the telescope. The light is then focused on a focal plane with Transition Edge Sensor bolometers (TES) cooled to 300mK with an adsorption refrigerator.

BICEP1, 2 and now 3 are built on the Dark Sector Laboratory[12] (DSL), whereas Keck Array (and now BICEP Array) are on the nearby Martin A. Pomerantz Observatory (MAPO), as can be seen in figure 2.12. Keck Array reused a mount from the QUaD experiment, itself reusing the one from DASI, which allowed the first discovery of the CMB polarization (Kovac et al. 2002). The South Pole Telescope (SPT), with its 10m mirror, is also at the DSL.

We will here focus on BICEP2 and Keck Array until 2015 since these are the data I worked on during my postdoc in Harvard. BICEP2 observed three years from 2010 to 2012 at 150 GHz, with 256 pairs of bolometers. Keck Array is basically a slightly improved version of five BICEP2 telescopes on the large DASI mount. Keck Array observed at 150 GHz for two year, then replaced 2 receivers by 95 GHz for two years, and two by 220 GHz receiver in 2015. Since then it has been mostly observing at higher frequency while BICEP3 observed at 95 GHz. During all these years, it focused on a small patch of the sky (1 percent effectively), this can be seen in figure 2.13.

For a complete review of the BICEP/Keck instrument and analysis, see Justin Willmert's thesis (Willmert 2019).

In chapter 4, I will present my main contribution to the analysis of BK data.

2.4 The SPIDER telescope

SPIDER (Suborbital Polarimeter for Inflation Dust and the Epoch of Reionization) is a balloon-borne experiment, sent in Antarctica in January 2015. It flew for 16 days around the South Pole at an altitude of roughly 36 kilometers. It is really similar to Keck array, with six small aperture refractive telescopes and uses the same detectors (see figure 2.14). For the first flight, three tubes were observing at 90 GHz, and three at 150 GHz (slightly offset but similar width as the Planck channels, see figure 2.15), containing each respectively 144 and 256 pairs of bolometers. A stepped half-wave

---

[12] Area near the Pole station with really little electromagnetic pollution.

Figure 2.12: Top: a picture of the DSL, where we see the BICEP ground shield and the SPT, with a zoomed top view of the BICEP2 telescope, photos from Steffen Richter. Bottom: A picture of the MAPO from Willmert 2019, where we see the Keck Array ground shield, as well as a top view on the telescope. Picture from Robert Schwarz.

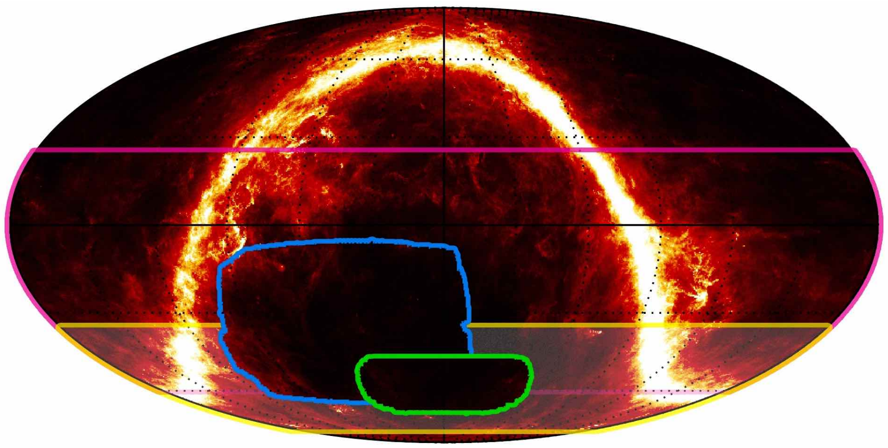

Figure 2.13: Observed region (BICEP2/Keck Array in green, SPIDER in blue) superimposed on a map of the galactic dust from Planck. Plot from Jon Gudmundsson. The yellow and pink show respectively what is accessible from South Pole and From Chile.

plate is mounted on top of each receiver and rotated twice a day. Its goal is to modulate the incoming polarization to disentangle it from polarization generated within the instrument (A. S. Rahlin et al. 2014). These telescopes provide low resolution images with a beam of Full Width at Half Maximum (FWHM) 42 (30) arc-minutes for the 95 GHz (150 GHz) receivers. SPIDER covered 12 percent of the sky in a region of low foreground, a bit offset compared to the smaller BICEP/Keck region (see figure 2.13). A second flight (SPIDER2) just happened this winter 2022-2023 with three receivers at 285 GHz and three at 150 GHz. For a complete review of the SPIDER instrument and analysis, see Sasha Rahlin's thesis (A. Rahlin 2016).

Figure 2.14: Left: a picture of the SPIDER balloon in Antarctica, before launch. Right: A picture taken from a camera on board of the balloon.

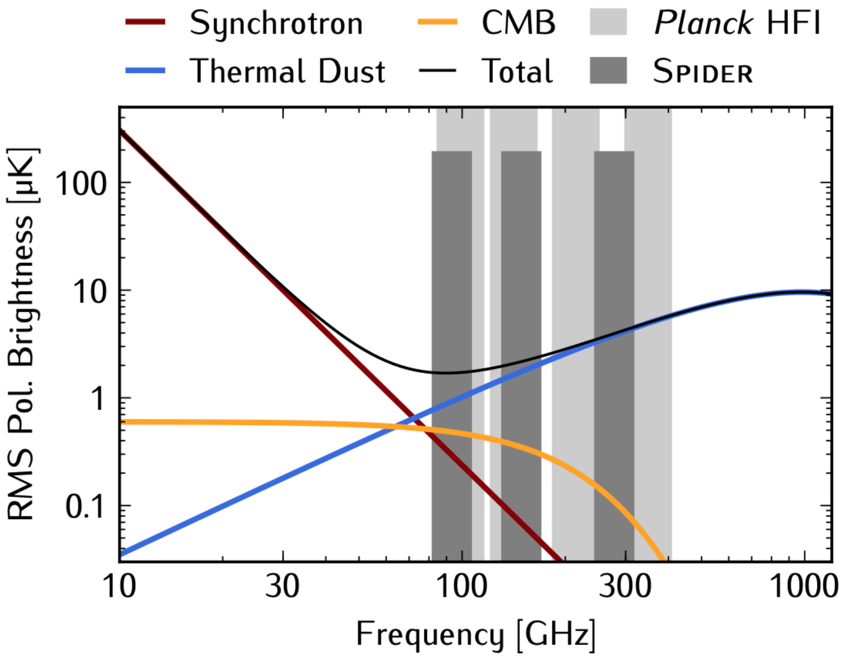

Figure 2.15: The frequency coverage of SPIDER versus some of the known polarized foreground emissions. The highest band is the SPIDER2 band at 285 GHz, which just flew in December 2022. Plot from Sasha Rahlin's thesis.

The official SPIDER analysis published results on B-modes in SPIDER Collaboration 2021, putting constraints of r<0.11 and r<0.19 with two methods, both using Planck data to constrain the dust contamination.

In chapter 3, I will show my contribution to an alternative pipeline to analyze SPIDER data.

2.5 My Contributions

In figure 2.16, I sketched how to go from the CMB photons to cosmological parameters. I worked in different aspects of this "pipeline".

- During my PhD, I worked on detecting the kSZ emission using the relative velocity of pairs of galaxies Benjamin Racine 2014.
- I also worked on measuring the non-Gaussianity of the Planck data, looking for primordial non-Gaussianity, but also studying the effect of instrumental systematics (from cosmic rays) and comparing different methods of component separation (Planck Collaboration XXIV 2014; Planck Collaboration XVII 2015; Collaboration et al. 2019; Benjamin Racine 2014).
- I helped developing a method to estimate the bispectrum of the CMB and extract the f_{NL} parameter (see Bucher et al. 2015).

- Using this method, we also studied the bispectrum of the CMB foregrounds Jung et al. 2018.

While these works are mostly related to my PhD work, and will not be described in this manuscript, I will describe the following points in the next chapters.

- I worked on the development of a full low level analysis pipeline going from raw data to CMB maps, using SPIDER data, (see chapter 3).
- I did the full cosmological analysis from power spectra to cosmological parameters with BICEP/Keck data (see chapter 4).
- I was one of the main person in charge of the forecasting of the detection of primordial gravitational waves from CMB-S4 (see chapter 5).

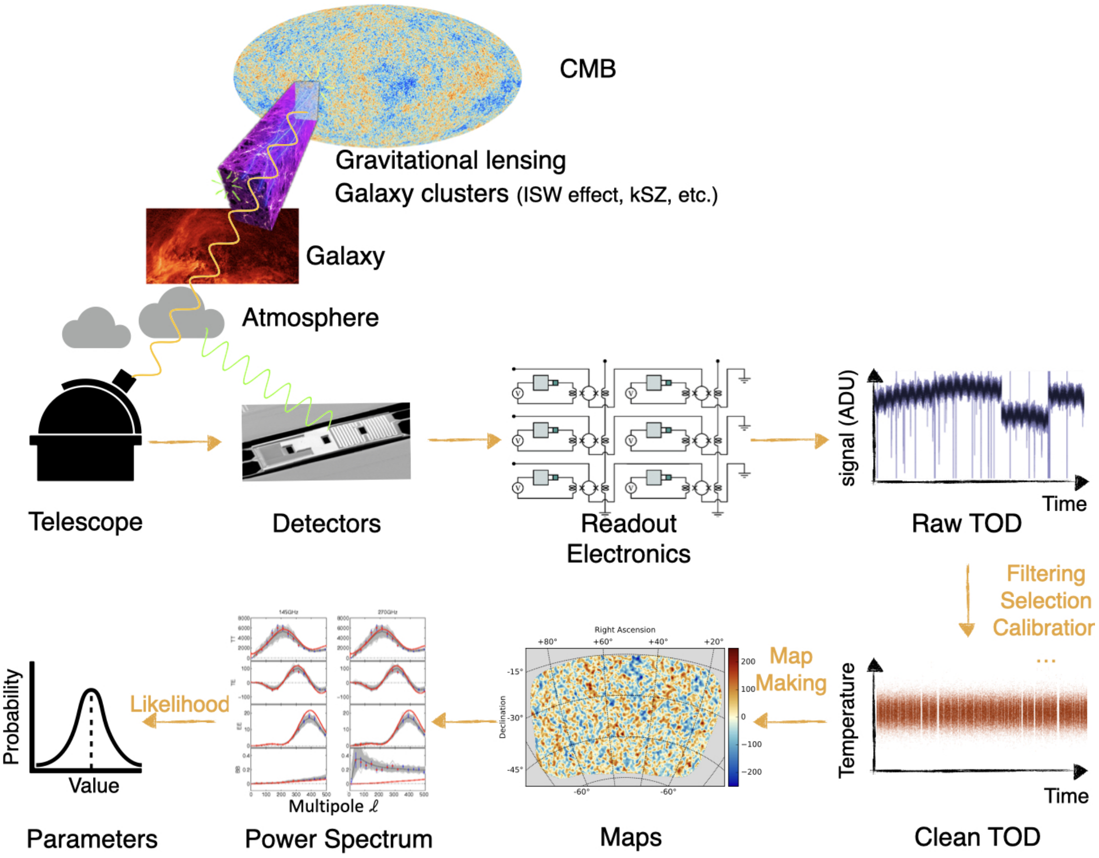

Figure 2.16: From CMB to cosmology. After recombination, the CMB photons (illustrated here by the temperature map from Planck satellite) go through the universe and interact in many ways with the large scale structures: gravitationnal lensing, (here illustration from ESA), kSZ, tSZ etc., and until they enter our Galaxy. The Galaxy itself is a major foreground in the microwave frequencies (illustrated here by a cutout of the Planck dust intensity map). The CMB photons nonetheless enter our atmosphere, which absorbs some of these photons and also acts as an additional source of noise. They then go through the telescopes optics and in the case of BICEP, get absorbed by the antennas. The signal then heats a transition edge sensor (here illustrated by a BICEP2 150 GHz bolometer). The numerous detectors are then read by a multiplexed SQUID based readout electronic which delivers our raw signal. We can then clean and calibrate this signal that we project into CMB maps. At this stage, we can compress it to power spectra and use a likelihood to compare it to our cosmological model, or use map based algorithm to extract the signal directly from the map.

3 From raw data to maps using SPIDER data

Sommaire

3.1 Introduction

In this chapter, we will go through the first stage of a CMB pipeline. We will focus on a pipeline we developed together with a PhD student, Tone Ruud, in Hans Kristian Eriksen's group in Oslo, to analyze data from the SPIDER telescope. A brief description of the telescope was given in chapter 2. There was already a pipeline developed mostly in Princeton, making CMB maps in a biased way, needing bias corrections. Our pipeline was designed to use a maximum likelihood unbiased mapmaker on SPIDER data. This chapter goes a bit in the dirty part of data analysis and shows some of the consecutive and almost chronological tricks applied to data to be able to exploit it.

3.2 SPIDER raw data

As explained in chapter 2, most CMB experiment observe microwave radiations using cryogenic bolometers. In the case of SPIDER or BICEP/Keck, these are antenna-coupled transition-edge sensor (TES) bolometers (BICEP2 and SPIDER Collaborations 2015), while Planck had feed-horn coupled ones. BICEP/Keck and SPIDER have co-located orthogonal oriented antennas, which allows a direct measurement of the polarization of the incoming light. The analog signal coming out from these bolometers is read in parallel using multichannel electronics, which use time ordered multiplexing, i.e. samples one channel at a time in the same wire. The signal is then amplified and converted to digital units or ADUs (analog-to-digital units).

These raw data are then stored in the form of what we will call here Time Ordered Data (TOD). Sasha Rahlin's thesis (A. Rahlin 2016) provides very extensive details of the cryogenic detectors and readout system, as well as a summary of the scanning strategy, gain estimation, etc., that we will not reproduce here. The simpler strategy from BICEP/Keck is summarized at the end of this chapter.

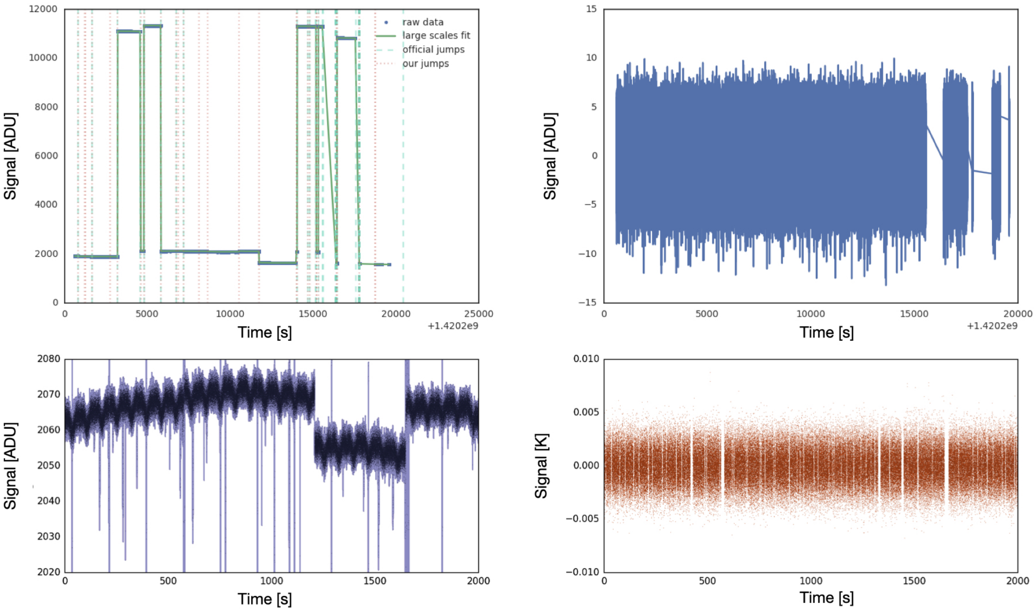

Figure 3.1: Top left: a raw TOD from the SPIDER telescope over 5 hours. Top right: the same TOD filtered and cleaned by our algorithms described in this chapter. In the bottom, we have a zoom on 30 minutes, with raw data on the left and on the right the final TOD in Kelvin, after calibration.

In figure 3.1 we show a raw TOD of a given detector from SPIDER. On the top left, we see more than 5 hours of data. We see that the baseline level jumps many time during this time frame. We see large jumps that are thought to be due to a change of regime on the electronics due to the large signal deposited when data is sent to Earth with the iridium antenna. The smaller jumps are due to large jumps in other detectors on the same multiplexing wire. For a review of this effect as well as many other noise pathologies, we can read Ed Young's thesis (Young 2018). In the bottom row, we see a zoom on this TOD, where we clearly see a modulation, which is mostly due to the CMB dipole, but could be also due to any other scan-synchronous signal, for instance from cloud emission pickup from side-lobes of the beam. We also see larger scale drifts probably due to changes of the temperature of the focal planes, as well as strong lines, mostly due to cosmic rays hitting the detectors, or antenna transmissions.

3.3 Mapmaking

In the main pipeline, data was cut into 10 minutes chunks to avoid the slow drift of the signal average, and an aggressive fifth order polynomial filtering was applied to remove the dipole and the scan-synchronous noise. All the short glitches were just flagged and removed from the analysis. The gain was computed using a new technique introduced by Filippini et al. 2022, where a stepped electrical bias was applied to the bolometers, to precisely measure the electrical gain, which can be transferred to the optical gain (see A. Rahlin 2016 thesis).

SPIDER uses information from star cameras to construct a pointing matrix. This matrix contains the position in the sky where the telescope is pointing, but also the polarization angle for the telescope and a given detector with respect to the sky (see previous chapter and Willmert 2019 thesis for a discussion on the very annoying IAU versus `HEALPix` conventions).

The signal from a TOD of a given detector can then be written as :

$$d = g(T + \gamma(Q\cos(2\phi) + U\sin(2\phi)) + n \tag{3.1}$$

where T, Q and U are the Stokes parameters at the position of the sky we are pointing at, g is the gain of the detector, γ is the polarization efficiency of the detector, ϕ is the angle of the detector with respect to the +Q coordinate convention, and n is the noise.

This equation can be written in a matrix form as :

$$\boldsymbol{d_t} = \mathbf{P}\boldsymbol{m_p} + \boldsymbol{n_t} \tag{3.2}$$

where $\boldsymbol{d_t}$ and $\boldsymbol{n_t}$ now have a dimension of (number of samples), $\boldsymbol{m_p}$ is a map vector of dimension (3 × number of pixels) and $\mathbf{P}$ is the sparse pointing matrix, of dimension (number of samples × 3 × number of pixels). In case of a Gaussian noise, the likelihood for the observed map is then:

$$\mathscr{L}(\boldsymbol{m}) = P(\boldsymbol{d}|\boldsymbol{m}) = \frac{e^{-\frac{1}{2}(\boldsymbol{d}-\mathbf{P}\boldsymbol{m})^{\mathrm{T}}\mathbf{N}^{-1}(\boldsymbol{d}-\mathbf{P}\boldsymbol{m})}}{\sqrt{2\pi|\mathbf{N}|}}, \tag{3.3}$$

where $\mathbf{N}$ is the noise covariance matrix $\mathbf{N} =< \boldsymbol{n_t}\boldsymbol{n_t}^{\mathrm{T}} >$. To get an optimal and unbiased estimate of $\boldsymbol{m}$ we then maximize this likelihood, which leads to :

$$\hat{\boldsymbol{m}} = (\mathbf{P}^{\mathrm{T}}\mathbf{N}^{-1}\mathbf{P})^{-1}\mathbf{P}^{\mathrm{T}}\mathbf{N}^{-1}\boldsymbol{d} \tag{3.4}$$

The map/pixel domain noise covariance is given by :

$$\mathbf{M} = (\mathbf{P}^{\mathrm{T}}\mathbf{N}^{-1}\mathbf{P})^{-1} \tag{3.5}$$

In a real world case, the noise is not simply Gaussian, white, etc. After flagging bad data and filtering some of the modes (with filter **F**), we can still recover an unbiased map, and the equations become

$$\hat{\boldsymbol{m}} = (\mathbf{P}^{\mathrm{T}}\mathbf{F}\mathbf{N}^{-1}\mathbf{P})^{-1}\mathbf{P}^{\mathrm{T}}\mathbf{F}\mathbf{N}^{-1}\boldsymbol{d} \tag{3.6}$$

with covariance:

$$\mathbf{M} = (\mathbf{P}^{\mathrm{T}}\mathbf{F}\mathbf{N}^{-1}\mathbf{P})^{-1}\mathbf{P}^{\mathrm{T}}\mathbf{F}\mathbf{N}^{-1}\mathbf{F}\mathbf{P}(\mathbf{P}^{\mathrm{T}}\mathbf{F}\mathbf{N}^{-1}\mathbf{P})^{-1} \tag{3.7}$$

This is the unbiased mapmaker that was used by the QUIET experiment (see Sigurd Naess' thesis: Naess 2012), which was developed in Oslo.

Solving for these equations is very intensive and many approximations can be used. For instance Planck uses a destriping mapmaker (see Planck Collaboration 2014) where they fit for offsets between different observation rings (when the satellite is rotating) that do not have the same baseline due to 1/f noise variations. For a nice review of many possible mapmaking variations, see Poletti et al. 2017.

One possible approximation is to consider the noise uniform and white, i.e. **N** is a diagonal matrix, with a constant noise σ^2 for each detector. The equation then becomes a simpler binning and for each pixel p we have:

$$\begin{pmatrix} I_p \\ Q_p \\ U_p \end{pmatrix} = \left[\sum_{\text{sample}_{ij}\in p} \frac{1}{\sigma^2_{ij}} \begin{pmatrix} 1 & c_{ij} & s_{ij} \\ c_{ij} & c^2_{ij} & c_{ij}s_{ij} \\ s_{ij} & c_{ij}s_{ij} & s^2_{ij} \end{pmatrix} \right]^{-1} \left[\sum_{sample_{ij}\in p} 1/\sigma^2_{ij} \begin{pmatrix} d'_{ij} \\ d'_{ij}c_{ij} \\ d'_{ij}s_{ij} \end{pmatrix} \right] \tag{3.8}$$

where we here bin a sample of detector i at time j into a pixel p where it is pointing. We omitted the gain and polarization efficiency for simplicity. c_{ij} and s_{ij} are respectively the cosine and sine from equation 3.1, d' is the filtered TOD. As long as we have a good enough coverage, the matrix will be invertible and easy to compute.

For the Gaussian uncorrelated (diagonal) white noise approximation to be acceptable, an aggressive filtering is applied and the estimation is no longer unbiased. This *binned mapmaking* is still extremely useful to do quick checks of maps from TODs and can be implemented in a few lines of code. It is also what is used in the main SPIDER analysis pipeline (see SPIDER Collaboration 2021). This requires a debiasing at the power spectrum level, based on Monte-Carlo simulations (as described in Hivon et al. 2002. See also next chapter).

3.4 Alternative Pipeline

The goal of our involvement in SPIDER was first to use the QUIET maximum likelihood map-maker (see Naess 2012 or Tone Ruud's thesis), which provides unbiased maps and pixel noise covariance matrices. The QUIET mapmaker was designed for data from radiometers, not bolometers. These detectors, though more noisy, have much less nasty glitches, jumps, etc. A lot of our effort then went into generating well behaved TODs. Note that for our pipeline, we built upon the already existing metadata, like gain variations, flags, instrument beams, pointing solution, etc. Note also that we average every 5 samples to reduce the data memory, going from a sampling at 119 Hz to 23.8 Hz.

This section is based on many postings we shared online for the SPIDER collaboration on a private wiki[1]. While the text is original and simplified, most figures are extracted from these postings and from extensive notes we wrote with Tone for the people taking over our effort in the Oslo group. The codes were shared on a private github but mine could be shared on request.

3.4.1 Filtering and noise modelling

One of the first steps of the QUIET map-making processing is to apply a bandpass filter (the filter of equation 3.6, shown in figure 3.2), given by:

$$F_{bp}(f) = \left[\left(1+\left(\frac{f}{f_{hp}}\right)^{\alpha_{hp}}\right)\left(1+\left(\frac{f}{f_{lp}}\right)^{\alpha_{lp}}\right)\right]^{-1} \tag{3.9}$$

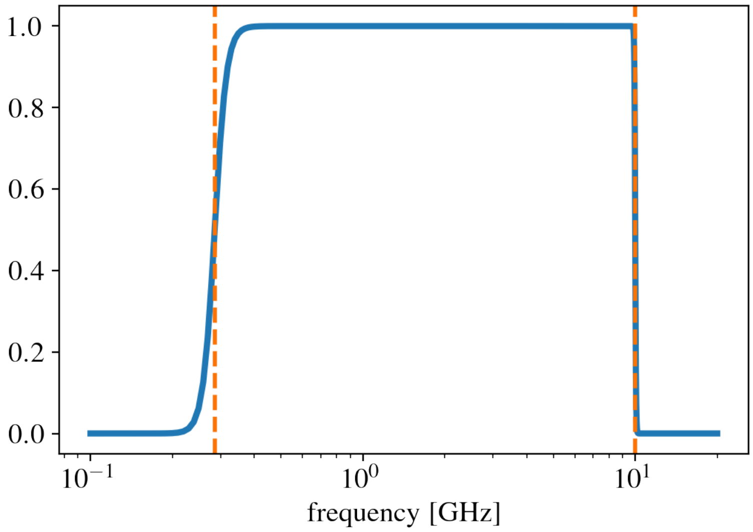

Figure 3.2: The bandpass filtered applied to data (see equation 3.9), where the dotted orange lines represent f_{hp}, 20 times the scanning frequency of 1/70 Hz and f_{lp} = 10Hz, while the apodization slopes are $\alpha_{lp} = -300$ and $\alpha_{hp} = -20$.

---

[1] All are available on this password protected wiki: http://spiderwiki.princeton.edu

The goal of this bandpass filter in QUIET was to remove very slow scan-synchronous noise due to weather as well as high-frequency features. It is a safe conservative filter to apply, even though it removes some of the large scale signal[2].

The second step is to measure the noise parameters that are then used to construct the noise matrix **N**. We fit a 1/f noise model:

$$\mathcal{N}(f) = \sigma_0^2 \left[1 + \left(\frac{f}{f_{knee}} \right)^{\alpha} \right] \tag{3.10}$$

We can fit this model to the power spectrum of the TODs (using the nice trick from Naess 2012 thesis).

With the features seen in figure 3.1, Fourier space filtering creates many ringing, edge effects, etc. In figure 3.3, we show four short TODs between to turnarounds of the telescope, and we see, for instance for detector x1r01c07, that the jump in the original noise creates ringing after filtering. We also have edge effects, due to applying a bandpass filter on a TOD in which some of the larger modes can not be well evaluated, and thus remain in the filtered TOD. This is barely visible in the TODs but much more when binning all the 12s TODs into a map, as shown in figure 3.4.

In figure 3.3, the noise model is also shown, and we see that with such short TODs it is hard to measure the slow variations.

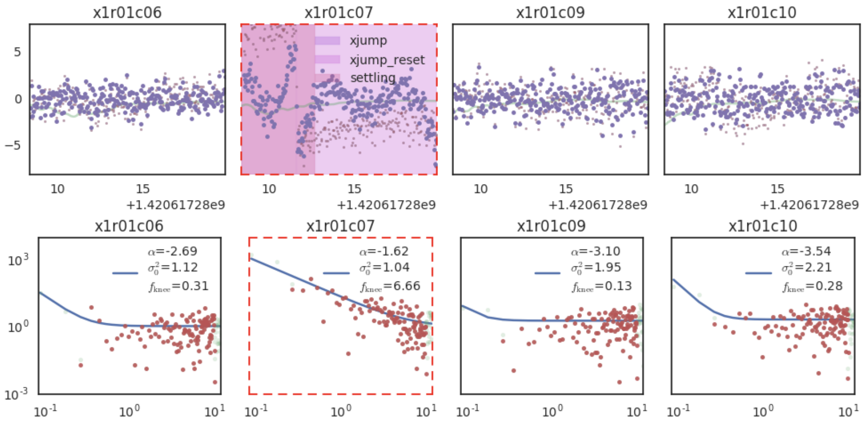

Figure 3.3: On top we have 4 TODs (ADU versus time) of naturally continuous data from SPIDER, with the name of the detector on top. In green we show the Planck signal converted to ADUs, which is removed from the data to get noise only TODs in light red. In purple we show the filtered TOD. The shaded colors corresponds to flags from the official pipeline, the red axes mean this region is removed from the official analysis, and the dotted means we also detected it in our flagging from noise parameters thresholding. In the bottom we see the power spectrum (in ADU^2 units versus Hz), as well as the fitted noise model.

---

[2] The mapping between TOD-level frequencies and map multipoles is complex, and can be recovered with simulations, which I did to check how the different filters affect the multipole space.

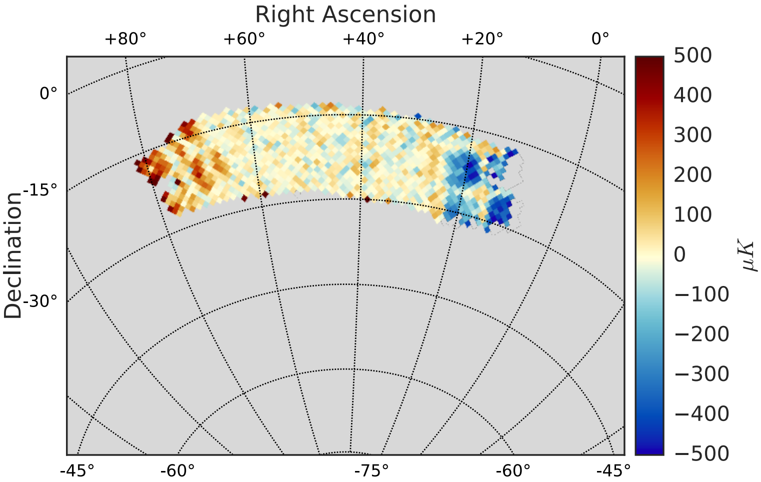

Figure 3.4: Here we show a simply binned map of 12s of data filtered using the same filter as figure 3.3. We see a residual dipole due to a bad evaluations of the larger modes on these short TODs.

3.4.2 Merging and large-scale fitting

To avoid the shortcomings introduced above, we decided to try to generate long, well-behaved TODs. For this, we merged data into much longer timestreams, two between two recurring long gaps (between two fridge cycles, explained in figure 6.3 of A. Rahlin 2016), i.e. roughly 6 per days. Of course then we are back to the original issue shown in figure 3.1, with very large jumps, drifts, oscillations, etc.

We can then separate the signal into two regimes, one being on scales $\boldsymbol{d_{LS}}$ much larger than our targeted cosmological scales, and one on smaller scales $\boldsymbol{d_{SS}}$:

$$\boldsymbol{d} = \boldsymbol{d_{LS}} + \boldsymbol{d_{SS}} = \boldsymbol{Ta} + \boldsymbol{d_{SS}} \tag{3.11}$$

where $\mathbf{T}$ is a matrix with a set of n template functions, each of the length the number of samples. $\boldsymbol{a}$ is the amplitude of these templates. Here our data $\boldsymbol{d_{SS}}$ can be considered as a Gaussian noise and we can use least-squares fitting, similar to equation 3.4:

$$\hat{\boldsymbol{a}} = (\mathbf{T}^{\mathrm{T}}\mathbf{N}^{-1}\mathbf{T})^{-1}\mathbf{T}^{\mathrm{T}}\mathbf{N}^{-1}\boldsymbol{d} \tag{3.12}$$

In our case, we considered a constant noise, so the noise matrices cancel. Note that solving this equation can be slow for large TODs with full resolution data. Since we only want to fit for large scales, we decided to "decimate" the data by averaging every 100 samples on top of the 5 samples decimation mentioned above.

The template matrix can incorporate any templates we want. We used 4 types of templates: offsets $\mathbf{O}$, drifts $\mathbf{D}$, cosines $\mathbf{C}$ and sines $\mathbf{S}$. While the sinusoidal functions are on the full TOD range, offsets and drifts are fitted on subregions of the TOD where the data is continuous, i.e. between jumps. Examples of these templates are shown in figure 3.5:

$$\mathbf{O} = \begin{pmatrix} 1 & 0 & \dots & 0 \\ 1 & 0 & \ddots & \vdots \\ \vdots & \vdots & & \\ 1 & 0 & \ddots & \vdots \\ 0 & 1 & \ddots & \\ \vdots & \vdots & & \\ 0 & 1 & & \\ 0 & 0 & & \\ & \vdots & & 1 \\ & & & 1 \end{pmatrix} \quad \mathbf{D} = \begin{pmatrix} d_1^{(1)} & 0 & \dots & 0 \\ d_2^{(1)} & 0 & \ddots & \vdots \\ \vdots & \vdots & & \\ d_l^{(1)} & 0 & \ddots & \vdots \\ 0 & d_1^{(2)} & \ddots & \\ \vdots & \vdots & & \\ 0 & d_m^{(2)} & & \\ 0 & 0 & & \\ & \vdots & & d_{n-1}^{(n_j)} \\ & & & d_n^{(n_j)} \end{pmatrix} \quad \mathbf{C} = \begin{pmatrix} c(\delta_0) & c(2\delta_0) & \dots & c(n_c\delta_0) \\ c(\delta_1) & c(2\delta_1) & \ddots & \vdots \\ \vdots & \vdots & \ddots & \vdots \\ c(\delta_{n_t}) & c(2\delta_{n_t}) & \ddots & c(n_s\delta_{n_t}) \end{pmatrix}$$

where for the drifts, $d^{(i)}$ run from -1/2 to 1/2, here for inter-jump regions of length l, m and n. For the cosine matrix, we use $c(\delta_n)$ to represent $\cos\left(2\pi\frac{i+1/2}{n_t}\right)$. We do not show **S** but it has the same structure as **C**, with sinuses. The template matrix **T** is just a stack of these four matrices.

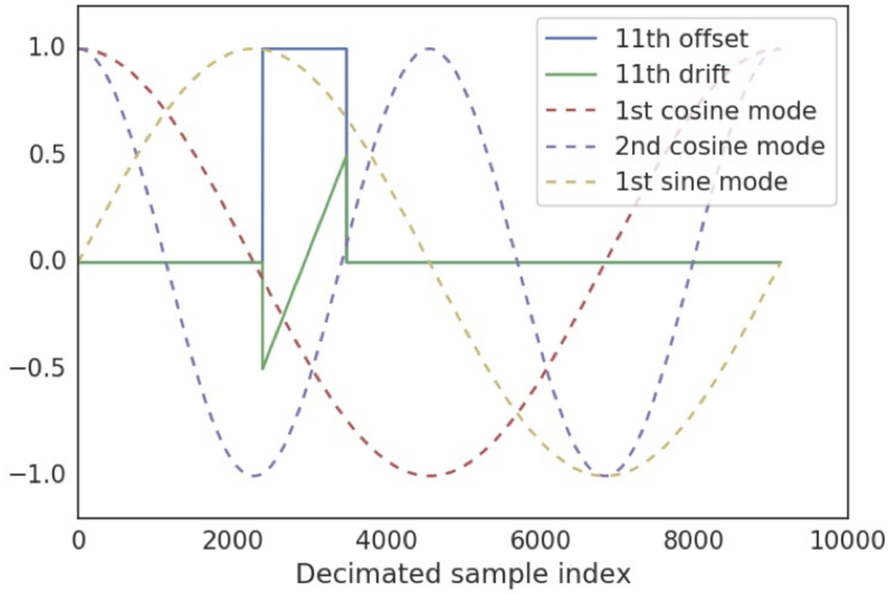

Figure 3.5: Examples of templates used in our matrix.

To choose the maximum frequency we want to fit using our sinusoidal functions, we looked at the improvement of the χ^2 as a function of maximal frequency. This is shown in figure 3.6. We chose to use 4 times the scanning frequency as a maximum frequency. This is far from the lowest frequency of the bandpass filter from figure 3.2.

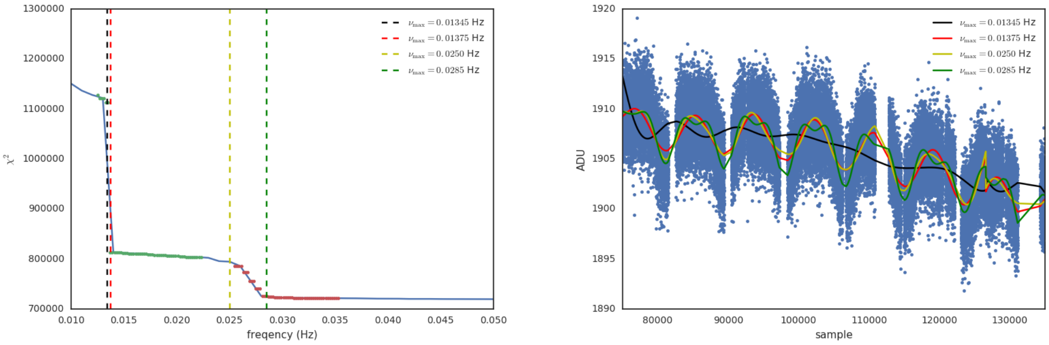

Figure 3.6: left: fit residual χ^2 as a function of maximal frequency. Right: TOD and best fit large scale for different maximum frequency. We see how the black curve did not catch the dipole oscillations, while the red one does. The green curve catches the scan-synchronous noise probably due to cloud pickup.

3.4.3 Jump finding

One of the steps necessary to define our templates is to find all the discontinuities in the data, which define the boundaries of the different columns of the **O** and **D** templates. We first used the "jump flags" from the official pipeline, but there were still many residual jumps. We designed a new algorithm where we use the residuals after large scale fitting and compute a running standard deviation. As can be seen in figure 3.7, the running standard deviation is stable for most data but has a discontinuity at jump positions. If it exceeds a given threshold, we flag the region as a jump. These jumps are added to our list and we iterate. We can see in figure 3.1 some of our jumps found on a long TOD.

3.4.4 Two-step least-squares fit

The issue with adding drifts and offsets to a sinusoidal basis is that it breaks the orthogonality of the basis. Some of the large harmonic modes are sometimes very degenerate with the drifts, especially when the inter-jump region is small. For many of our TODs the condition number of our $(\mathbf{T}^{\mathrm{T}}\mathbf{N}^{-1}\mathbf{T})$ matrix was above 10^{12} which made the solution numerically unstable.

We switched to a two-step fit, where we first fitted for the offset and drift terms, i.e. using a template matrix $\mathbf{T_{OD}} = [\mathbf{OD}]$ to get the best fit amplitude $\mathbf{a}_{\mathrm{OD}}$.

We then went on to fit for full template matrix with a prior on the offsets and drifts:

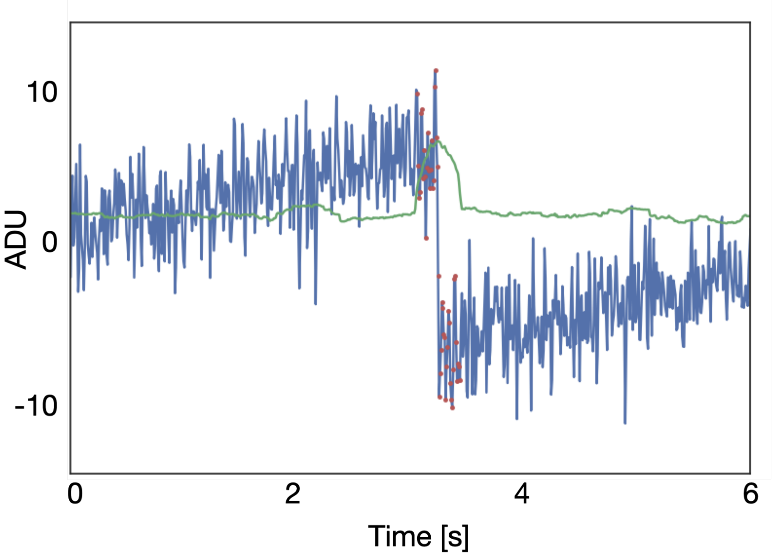

Figure 3.7: In blue we show a zoom on a TOD from which a first pass of the large scale residuals were removed. We clearly see a discontinuity. In green we compute the running standard deviation, with a window of 50 samples, the red dots around the jump are flagged in further steps of the processing.

$$\hat{\boldsymbol{a}} = (\mathbf{S}_{\mathrm{OD}}^{-1} + \mathbf{T}^{\mathrm{T}}\mathbf{N}^{-1}\mathbf{T})^{-1}(\mathbf{T}^{\mathrm{T}}\mathbf{N}^{-1}\boldsymbol{d} + \mathbf{S}_{\mathrm{OD}}^{-1}\mathbf{a}_{\mathrm{OD}}) \tag{3.13}$$

where $\mathbf{S}_{\mathrm{OD}}$ is the prior, built from the covariance of the first fit: $\mathbf{S}_{\mathrm{OD}} = (\mathbf{T}_{\mathrm{OD}}{}^{\mathrm{T}}\mathbf{N}^{-1}\mathbf{T}_{\mathrm{OD}})^{-1}$ We left a bit more freedom in the fit by using 10 * $\mathbf{S}_{\mathrm{OD}}$ in the prior. This clearly helped having more "physical" solutions, as can be seen in figure 3.8, but the condition number remained poor for some of the TODs.

3.4.5 Gap filling

The TODs that had the worst condition number after the two-step fit where the ones with larger gaps. We then designed a gap-filling algorithm for the second step of the fit. We used the results of the first step as a baseline, to which we added a fake signal generated from Planck maps (including the dipole) and the local noise from the estimated local standard deviation. We also did a linear interpolation to account for a drift within the gap, using data from which we removed Planck signal (to avoid for the cropped dipole oscillations to mimic a drift). This gap filling can be seen in figure 3.9. It reduced the condition numbers to below $O(10^4)$ in most cases.

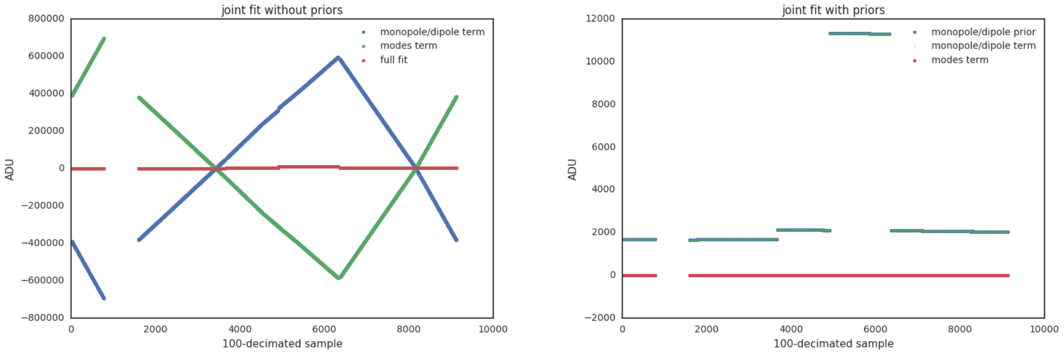

Figure 3.8: Left: contribution of the offset/drift modes versus the sinusoidal modes when doing a joint fit. We can clearly see the huge degeneracy of the large sinusoidal modes and the drifts. Right: same, but with a two-step fit.

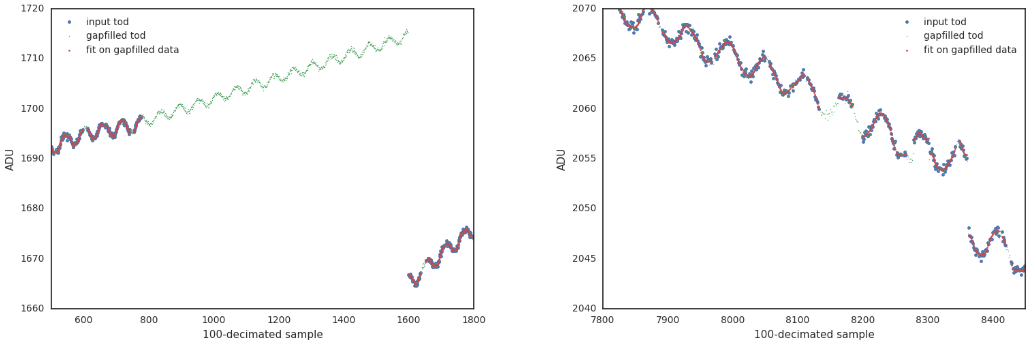

Figure 3.9: Zooms of the gap filled data and the fit projected on the unflagged part, as used in the algorithm, for the same data as shown in figure 3.8. Left: On big gaps, if there is a jump at one of the edge, the drift and dipole term can sometimes dominate visually the gap filling data, but since this is used as a prior and fitted out, it should not be a problem. Right: an example with a smaller gap, and a clear jump.

3.4.6 Preliminary SPIDER Maps

With all the effort described above, we have a way to generate long stable TODs, as can be seen comparing the left to right column of figure 3.3.

Using the official pointing and gain, we can then use a binned mapmaker to produce T, Q and U maps. These maps are shown in figure 3.10. Note that these are really similar on small scales to the map from the official pipeline, but have large modes left. These are preliminary maps from our effort with Tone Ruud. Further study was needed, for instance to know if these remaining modes were cosmological or systematics from the analysis. A work to relax our cuts in a controlled way would have also been great: we were also applying very conservative cuts, for instance only allowing 3 iterations of the jump finder and flagging the whole TOD if it did not converge. And of course, our goal of using the QUIET mapmaking was not yet full-filled. Some of these issues were solved from students that took over this project, we can see some in the thesis from Harald Thommesen (Thommesen 2019). While we were advancing on this project, the group in Oslo became more and more interested in performing a fully Bayesian pipeline, going from raw TODs to cosmology, propagating all aspects of data selection, filtering, etc. This is the core of a project called Cosmoglobe[3], which uses the `Commander` framework (Eriksen et al. 2004; Eriksen et al. 2008. This project is supported by multiple ERC, and Norwegian national funding. An update on the SPIDER analysis, based on our work was made recently and the video can be found online[4].

3.5 Short summary of the BICEP/Keck pipeline from raw data to maps

Here we summarize how the BK pipeline goes from raw data to maps. Note that this pipeline is fully independent from the SPIDER pipeline, and coded in matlab, while SPIDER is in python, but many aspects are similar due to common origins of the projects. For a great thesis on the data analysis, see Justin Willmert's thesis (Willmert 2019).

BICEP/Keck instruments were introduced in chapter 2. Here we can just consider that BICEP is a cousin of SPIDER, with same detector technology and a very similar optical design, but on the ground, at the South Pole. The advantage at Pole is that we can follow the same patch of sky during the whole winter season, just scanning in azimuth. The telescope scans back and forth 100 times at constant elevation for 50 minutes (called a *scanset*), then elevation is changed by 0.25 degrees (see BICEP2 Collaboration 2014).

After every *scanset*, a relative calibration is possible using a 1 degree elevation "nod", i.e. observing up and down through more or less airmass in a controlled way to fit

---

[3] `https://www.cosmoglobe.uio.no/`

[4] `https://www.youtube.com/watch?v=KMVJ8F1bOqA`

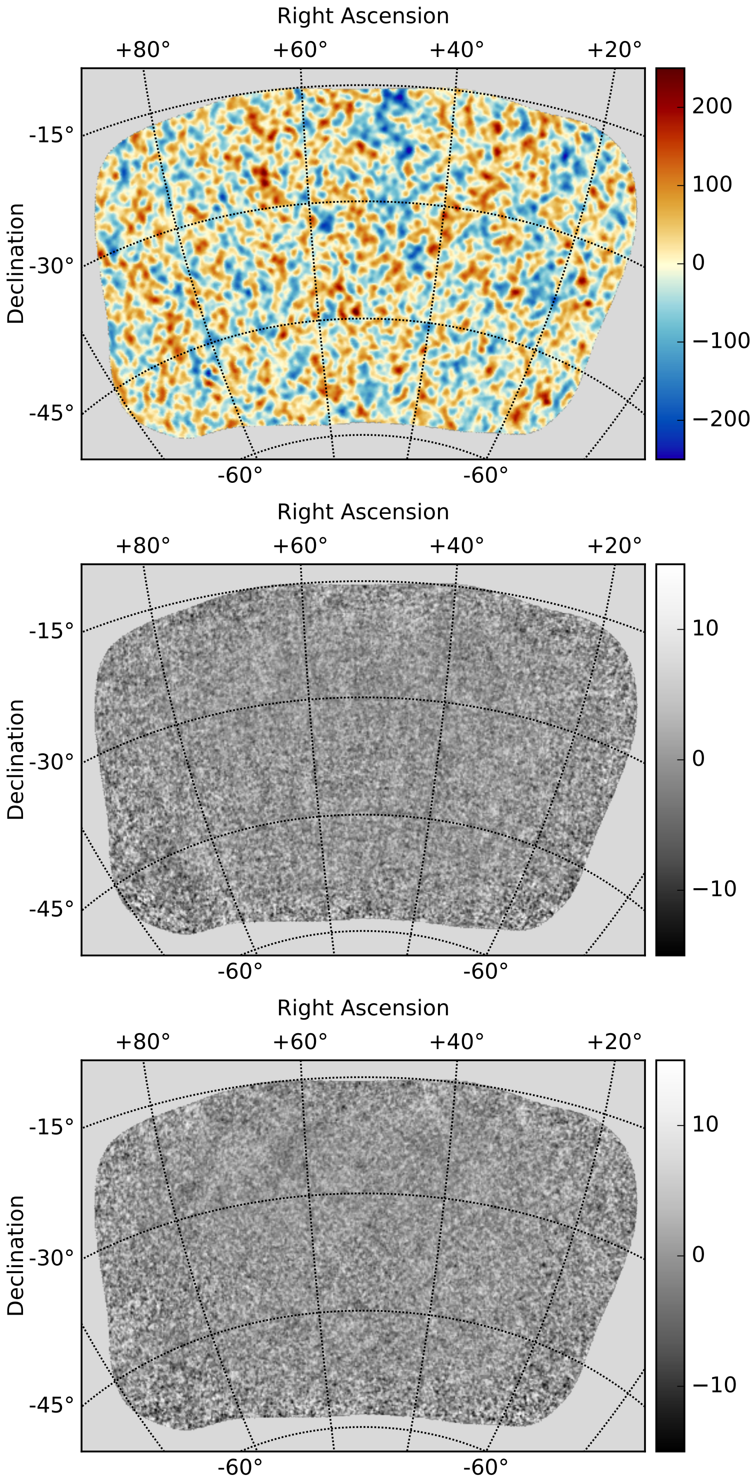

Figure 3.10: SPIDER T, Q and U maps (in μK) generated using a simple binned map-maker from equation 3.8, using all the filtering algorithm described above.

for a relative gain. One of the main differences with SPIDER is that BICEP/Keck uses the differential signal of co-located orthogonal detectors. The common temperature signal cancels and we are left with polarization only "pair-difference" TODs. Note that SPIDER had too many broken pairs and solved for polarization by knowing the orientation of each single antennas in the map-making equation.

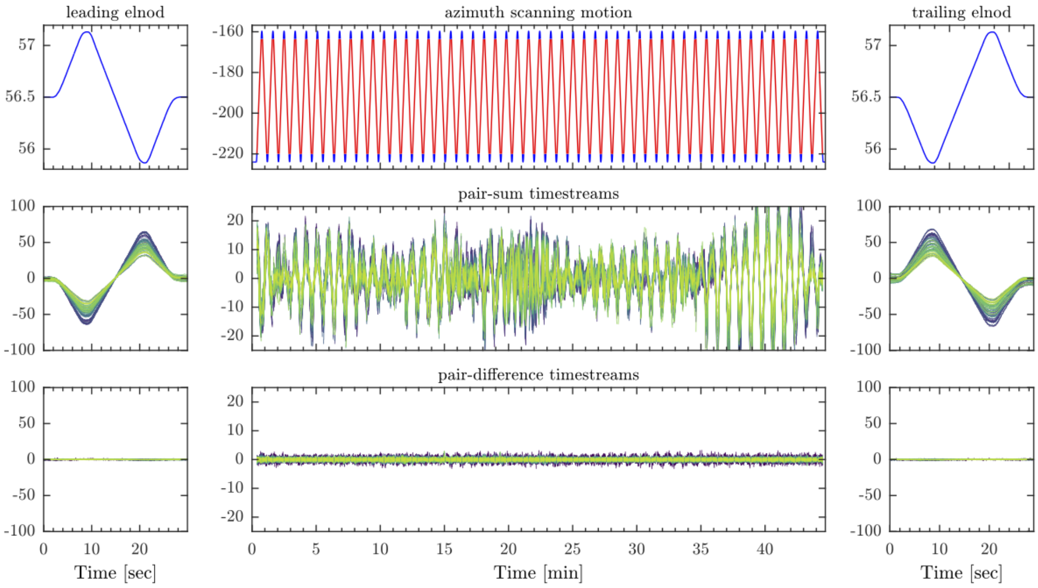

Figure 3.11: A TOD from BICEP/Keck. See text.

An example of a TOD is shown in figure 3.11. On top, we see the elevation nod (left and right), and constant elevation, azimuth scanning in degrees (center), as a function of time. In the middle row, we see the pair-sum TOD after relative calibration and offset (in some arbitrary units). In the bottom we see the pair-difference TOD. We can see effects of atmosphere in the pair-sum, while the pair-difference is quiet, the atmosphere being very weakly polarized. Note that this figure is a high definition plot from Justin Willmert's thesis (Willmert 2019), but a low resolution version is part of diagnostic plots that are checked for all the data every week by members of the collaboration, which is very unique and extremely valuable.

First, glitches (spikes, cosmic rays, etc.) are removed. Then these pair-sum and pair-difference TODs are filtered with a third order polynomial. Using a stack of the 50 scans in each direction, in which the sky rotated but the ground is fixed, an estimate of ground pickup is removed from the data. This is also a big difference with SPIDER, where this large scale scan-synchronous signal was much harder to estimate.

Using a pointing matrix reconstructed using the star cameras, the TODs are then projected onto a grid with a noise weighting to create T, Q and U maps (see equation 3.8). To suppress temperature to polarization leakage due to beam misalignment, beam width or ellipticity misscalibration, etc., a technique called deprojection (see BICEP2 Collaboration 2015) is performed, where the much higher signal of the T map is used to predict what effect these would have on the polarized TOD. Maps at 150 GHz can be seen in figure 3.12, extracted from Keck Array and BICEP2 Collaborations et al. 2018, with on the left the signal and on the right, the noise estimated by randomly assigning positive and negative signs while binning the TODs during mapmaking. More recent maps are available in the latest BICEP publication using data until 2018, see Keck Array and BICEP2 Collaborations 2021.

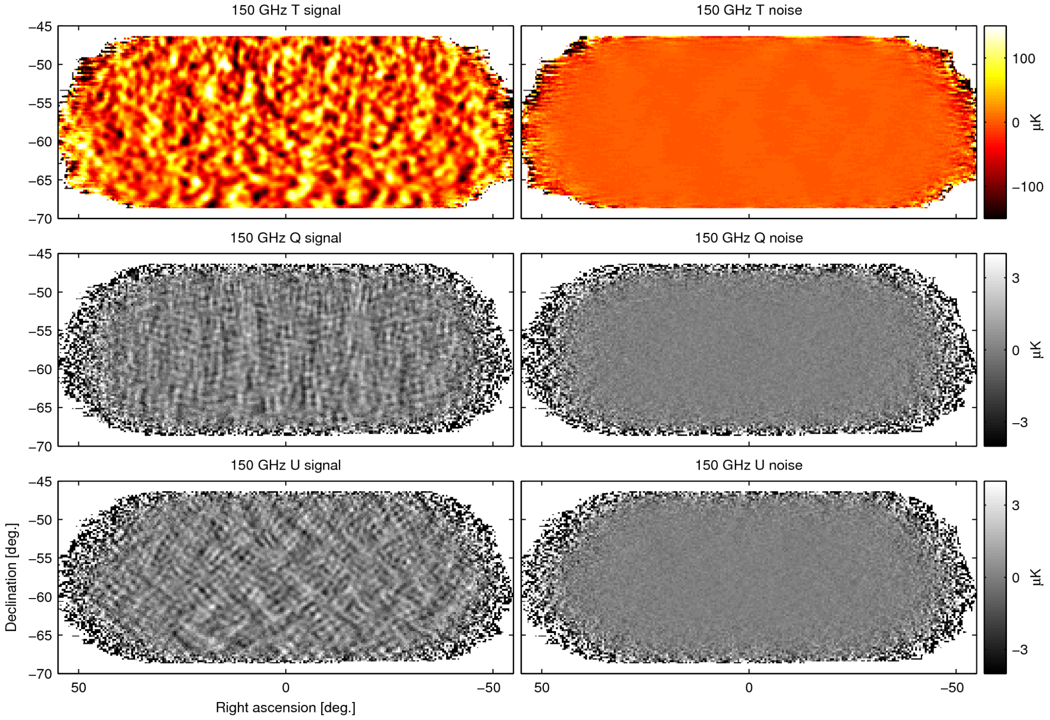

Figure 3.12: 150 GHz maps from the BK15 paper.

3.6 My contributions

Within our Oslo-based SPIDER alternative pipeline, I developed and wrote all the python code for the algorithms discussed in this section: the filtering and noise modelling, the large scale least-squares fitter, the design of the template matrix and its optimization, the jump finder, the two-step solution with prior and the gap filling algorithm. I also wrote the binned mapmaker used to make the maps shown here. Together with Tone Ruud, who was an expert of the QUIET mapmaker, we also developed all the parallelized pipeline to put all of these algorithms together to analyze all SPIDER data from raw TOD to maps, using the OWL computer cluster in Oslo.

4 From maps to Cosmology using BICEP/Keck data

Sommaire

In this chapter, I will describe some of the work I did in John Kovac's group in Harvard, within the BICEP/Keck (BK) collaboration. Most of this work was done with a PhD student in the group, Victor Buza.

This chapter is based on many html postings we shared online for the BK collaboration on a private website[1].

4.1 Maps to power spectra

In the previous chapter, we summarized the BK pipeline from raw data to map (see 3.5). Once these maps are obtained, they are transformed into Fourier space[2] to create E-modes, as explained in Willmert 2019 and seen in figure 4.1. At that stage, a clever technique is applied to avoid E-to-B leakage due to sky cuts and TOD filterings (matrix purification[3] - see Keck Array and BICEP2 Collaborations 2016a).

---

[1] All are available on this password protected website: http://bicep.rc.fas.harvard.edu/bkcmb

[2] This is possible for a small map like BICEP where the small angle approximation allows to use flat-sky Fast Fourier Transforms instead of spherical harmonics.

[3] See also my preliminary work to adapt this code to CMB-S4: http://bicep.rc.fas.harvard.edu/CMB-S4/analysis_logbook/20190130_Matrix_first_try/

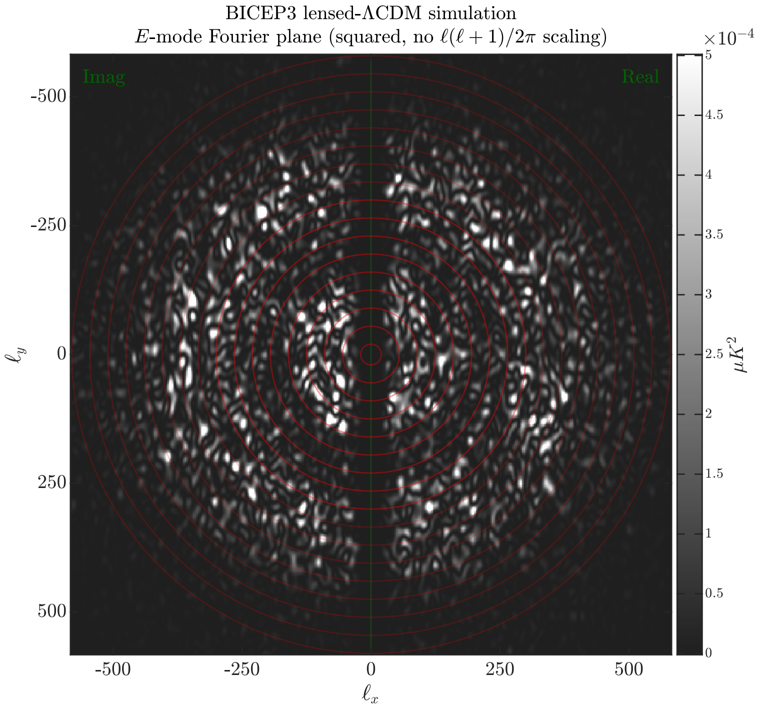

Figure 4.1: A representation of the Fourier plane of E-modes from a BICEP3 simulations, from Willmert 2019, with square of the imaginary part on the left and real part on the right. We see the first and second acoustic peak. Due to the filtering mentioned in the previous chapter, the large modes in the "x" axis are not measurable. The red circles are the annuli in which we compute the bandpowers.

To obtain the angular power spectrum we average this Fourier plane in annuli of radius $\Delta\ell = 15$[4] to get 17 bandpowers between $\ell = 20$ and $\ell = 580$. These bandpowers are biased, as mentioned in the previous chapter. We use 499 sign-flip noise simulations (see 3.12) to estimate the mean noise bias and remove it from the data (as introduced in Hivon et al. 2002). These noise simulations are also used to estimate the variance of these bandpowers.

Since we just briefly introduced our noise simulations, we will here divert a little to introduce the signal simulations. These are 499 `HEALPix` maps generated from a theoretical power spectrum using `CAMB`, reobserving them using the pointing matrix, and passing the resulting simulated TODs through the whole pipeline. We have 4 sets of simulations: unlensed ΛCDM, lensed ΛCDM, Gaussian dust only, and r=0.2 B-modes simulations.

Another effect we need to take into account is the effect of the beam and the filtering (see previous chapter) on the power spectrum. For that, we simulate $\delta\ell = 1$ maps to which we apply a beam, go through the same steps as the data and compute the corresponding power spectrum. We can then reconstruct a mixing ma-

---

[4] We first multiply by $\ell(\ell+1)/2\pi$ to produce D_ℓ bandpowers.

trix or bandpower window function (BPWF – see for instance the ones from CMB-S4 on my public posting: http://bicep.rc.fas.harvard.edu/CMB-S4/analysis_logbook/20181127_bpwf_DC4/). The integral of these functions corresponds to how much a given bandpower has been suppressed. Note that these suppression factors apply both to the signal and noise, so it is not a measure of the loss of signal-to-noise. We then divide all the bandpowers by these suppression factors to get an estimate of the signal bandpower. The raw signal+noise bandpowers are shown in figure 4.2. In that plot, we see how the noise bias is negligible in the signal dominated EE bandpowers, but important in BB, except for the cross-frequency spectra where the noises are independant. We see also the large effect of the suppression factor on EE.

This is also at this stage that the absolute calibration is performed. In the previous chapter we explained how the detectors are relatively calibrated, using elevation "nods". But to go from a relative calibrate ADU to μK, we compute the ratio between a cross-spectrum of a BICEP map to the closest Planck frequency (say BK95 and Planck90) and a cross-spectrum of that same Planck map to a reference Planck map (say Planck143). Since the Planck maps are calibrated, if we take into account the beam, filtering, etc., the cross-spectrum should be a constant, which is the calibration factor.

Once all the data has been processed, we test for possible systematics using jackknives, i.e. differences of splits of the dataset that should be consistent with noise. These splits are created to test for specific possible systematics, for instance splitting according to the scan direction, or between high moon phase and low moon phase. We then check that all of the bandpowers from these difference maps are consistent with noise. A full table is for instance shown in Keck Array and BICEP2 Collaborations et al. 2018.

4.2 Achieved performance

It is important to have a way to measure our achieved performance across several seasons of observations, both to keep track of the evolution of our datasets, as well as to use these to forecast future observations. Here we show a condensed summary statistics of the achieved performance, based on our noise simulations. Having these produced by other teams would be very beneficial in order to have a fair comparison of the information content of a dataset. In this section, I introduce a study I made based on some preliminary work from Colin Bischoff.

The noise spectrum of a given experiment can be modeled from a few parameters (Knox 1995 and Tegmark 1997):

$$N_\ell = \frac{\Omega}{N}\frac{\sigma^2}{B_\ell^2} = \frac{f_{sky}}{\omega B_\ell} = \frac{4\pi f_{sky}\sigma^2}{N_{pix}B_\ell^2} \tag{4.1}$$

The beam B_ℓ is unit-less, σ is the noise of a given pixel, in μK, Ω is the size of the

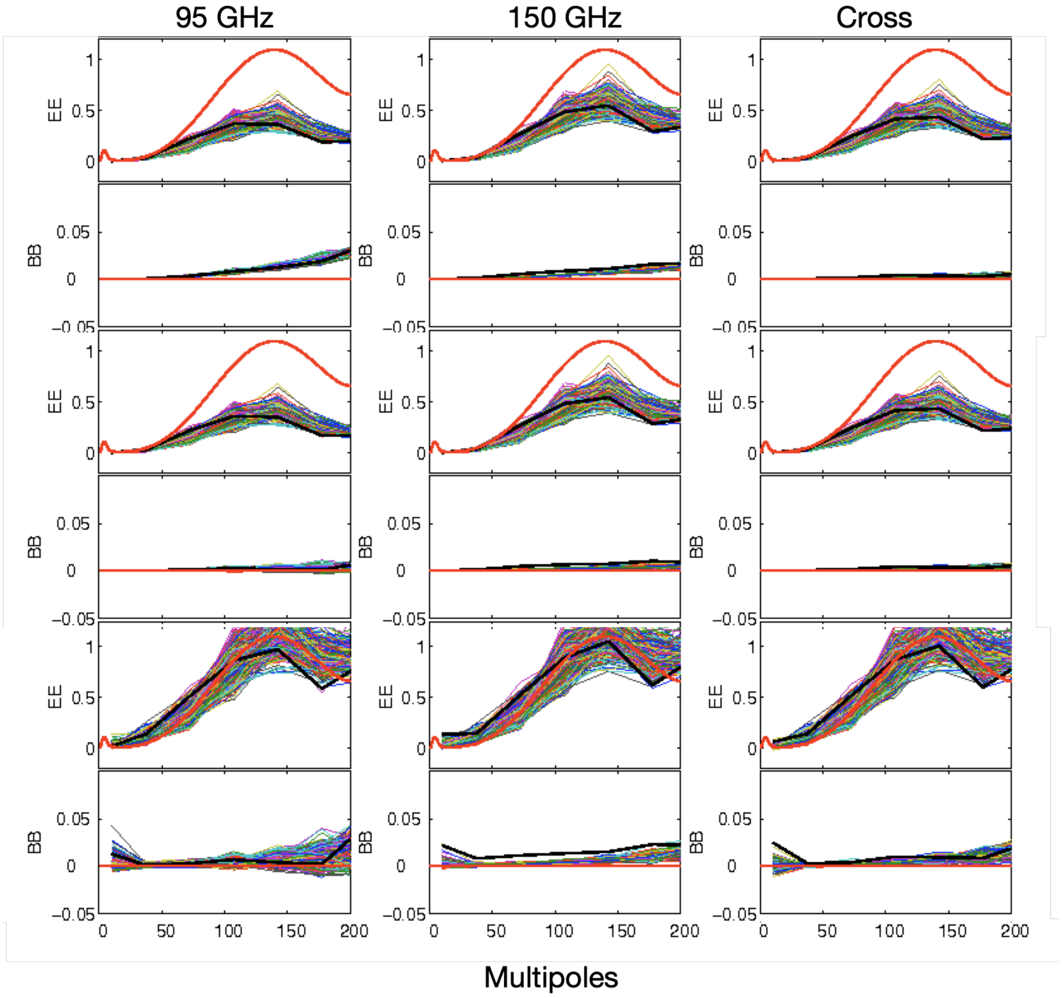

Figure 4.2: BK15 selected bandpowers ($\ell(\ell+1)C_\ell/2\pi[\mu K^2]$). On top, we have the raw bandpowers of the data (black), the model (red) and the 500 colored simulations, both for EE and BB. In the middle we have applied the noise bias correction, and in the bottom we also applied the filter/beam suppression factor correction. On the left we have the 95 GHz from BK15, in the middle the 150 GHz, and on the right the 95x150 cross-spectrum. This is taken from a private posting from Justin Willmert summarizing all the bandpowers of the BK15 dataset and many other statistics.

observed patch in steradian, and N is the number of pixels. ω is the raw sensitivity in $\mu K^{-2}\,\mathrm{deg}^{-2}$, and f_{sky} is the fraction of sky observed.

One of the usual figure reported by experiment is the map depth, in μK- arcmin, which is defined so that it does not depend on the size of a pixel. If you have many more smaller, noisier pixels, or a few big pixels with low noise, the depth should be the same. The variance of a given pixel σ^2 varies linearly as 1 over the pixel area, we have

$$\sqrt{\sigma^2 \frac{\Omega}{N}} = \sqrt{N_\ell B_\ell^2} \left(= \sqrt{\frac{f_{sky}}{\omega}} \right) \tag{4.2}$$

We define the map depth directly from the noise bandpowers N_{bp}:

$$\text{map depth} \equiv \sqrt{N_{\mathrm{bp}}} \tag{4.3}$$

The noise bandpowers have had a suppression factor applied, including filtering and beam effects, which is why we do not convolve with the beam. With this definition, the map depth represents how "deep" our data are for a given multipole. Note that this is in μK- radian, that we multiply by $(180/\pi)$ to get μK- deg (and multiply by 60 for μK- arcmin). This is what we plot in the top pannel of figure 4.3.

As explained in Tegmark 1997, for an unfiltered observation of the CMB over a fraction of the sky, the sample variance of our noise bandpowers N_{bp} is:

$$\sigma(N_{\mathrm{bp}}) = \sqrt{\frac{2}{\Sigma_{\ell \in bp}(2\ell+1) f_{sky}}}\, \bar{N}_{\mathrm{bp}}, \tag{4.4}$$

where here the $\ell \in bp$ represents the averaging in annuli of size $\Delta\ell = 35$. We can then estimate the effective f_{sky} per multipole due to filtering and beam effect using the mean and standard deviation of the bandpowers of the 499 noise simulations:

$$\text{effective } f_{sky} = \frac{2}{\Sigma_{\ell \in bp}(2\ell+1)} \left(\frac{\bar{N}_{\mathrm{bp}}}{\sigma(N_{bp})} \right)^2 \tag{4.5}$$

In the middle pannel of figure 4.3, we report these areas both in terms of percent and in deg^2, by multiplying by $4\pi(180/\pi)^2$.

We then compute the survey weight, defined with the ratio:

$$\text{Survey Weight} = 2 \times \frac{\text{Effective Area}}{(\text{Map Depth})^2} \tag{4.6}$$

Survey weight increases linearly with integration time or detector count. It is a good metric for comparing the information content of surveys. The factor of 2 here comes from the fact that we report the survey weight for total Q and U polarization, whereas we only used the BB bandpowers here.

A caveat is that here we use the bandpowers from the noise simulations that are already binned $\mathcal{D}_\ell$'s, instead of C_ℓ's. We do an approximative correction, multiplying

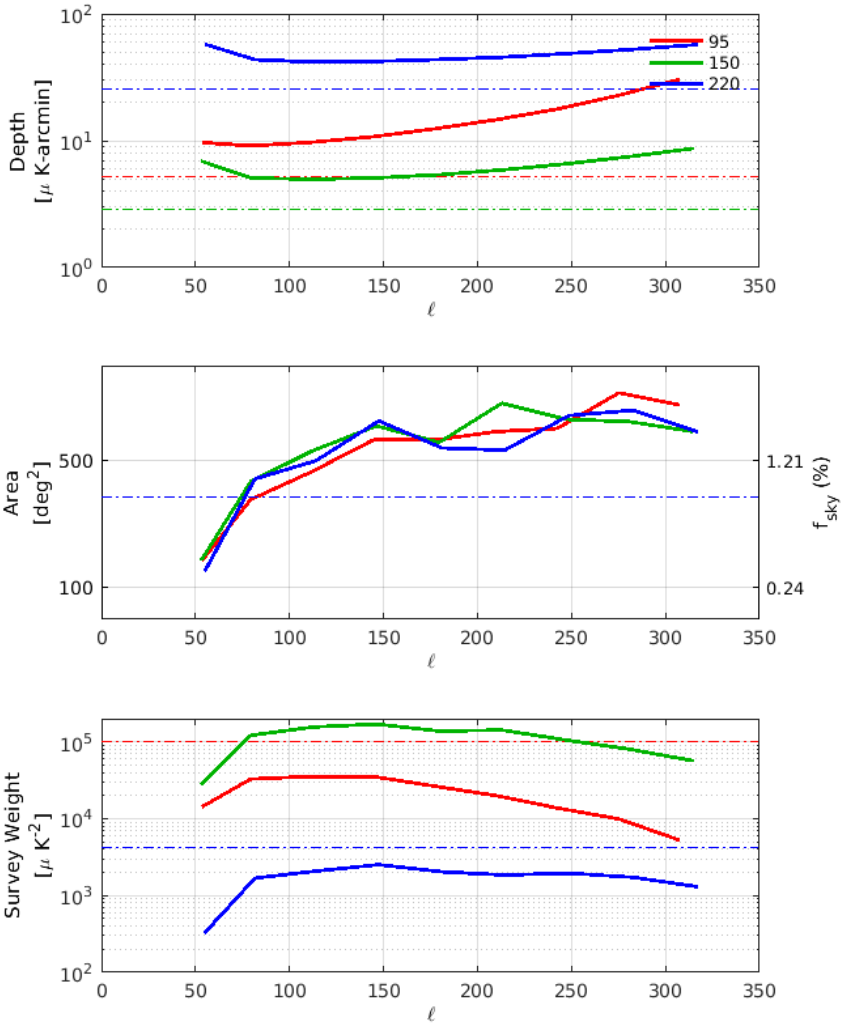

Figure 4.3: (Top row) Map depth, in μK- arcmin. (Middle row) Map area in square degrees and f_{sky} in %, i.e. the observed number of B-mode degrees of freedom divided by the nominal full-sky number. The turn-down at low ℓ is due to mode loss to the timestream filtering and matrix purification. These two rows are shown in Keck Array and BICEP2 Collaborations et al. 2018. (Bottom row) Survey weight in μK^{-2}. We show the 9 baseline bandpowers used in the analyses. The dot-dashed lines show the map based estimated of these performance measurements, not presented here.

the bandpowers by $\frac{2\pi}{\ell_{bin}(\ell_{bin}+1)}$. We briefly studied how the noise spectra change when using different definition of ℓ_{bin} in `http://bicep.rc.fas.harvard.edu/CMB-S4/analysis_logbook/20190220_noiseparams_bk15_forS4`. Here we used the flat-C_ℓ weighted bandpowers.

While here we focused only on the full BK15 dataset, I did a finer study of all the datasets of the BK team, including the ones after BK15, all the way to 2020. I showed the poor performance of some of the 150 GHz receivers in early Keck Array years, as well as good performance of 95 GHz receivers in general. 210 and 220 GHz turned out to be stable over years, but the first years of 270 GHz had poor performance.

4.3 BICEP/Keck multi-component likelihood analysis

As mentioned in chapter 2, one of the main difficulties on the road to B-mode detection is the handling of polarized galactic foregrounds. Since the first BICEP2 paper (BICEP2 Collaboration 2014) and the following BICEP/Keck and Planck analysis (BKP, Keck Array, BICEP2 and Planck Collaborations 2015), we know that there is indeed a B-mode signal, but compatible with a pure dust emission. To analyze the Planck data together with BICEP2 data, a multi-frequency bandpower based likelihood was developed, modeling both the cosmological and the galactic components. For a detailed review on this, refer to the thesis by Buza 2019. In this section, we will describe the likelihood used for the BK15 paper (Keck Array and BICEP2 Collaborations et al. 2018).

4.3.1 The Hamimeche-Lewis likelihood

As first brought up in the BICEP1 analysis (Barkats et al. 2014), the number of degrees of freedom per bandpower is small on large scales. This is visible in the middle panel of figure 4.3, where less that half a percent of the modes available on full sky are observed. While for smaller scales (or for full sky observations), where many modes are averaged, the central limit theorem applies and the likelihood is Gaussian, here we need to take into account its non-Gaussianity. For our analysis, we use the Hamimeche-Lewis (HL) likelihood (Hamimeche and Antony Lewis 2008)[5].:

$$-2\log\mathscr{L}(\boldsymbol{D}_b|\hat{\boldsymbol{D}}_b) = X_g^T \mathscr{M}^{-1} X_g, \tag{4.7}$$

where $\mathscr{M}$ is the fiducial model's (BandPower Covariance Matrix (BPCM)) defined below, and $\boldsymbol{X_g}$ are bandpowers transformed to correct for their non-Gaussian likelihood:

$$[\boldsymbol{X_g}] = \mathrm{vecp}\left((\boldsymbol{D}_b^f)^{1/2} g\left(\boldsymbol{D}_b^{-1/2}\hat{\boldsymbol{D}}_b\boldsymbol{D}_b^{-1/2}\right)(\boldsymbol{D}_b^f)^{1/2}\right). \tag{4.8}$$

Here $\boldsymbol{D}_b$ are the model bandpowers (integrated into the BPWF to obtain bandpowers, to which we add the noise bias), $\hat{\boldsymbol{D}}_b$ are the raw data bandpowers. They are organized in a matrix of all auto or cross-bandpowers, i.e. cross-bandpowers of fields (TT, EE, BB,

---

[5] We will use a mix of notations from (Barkats et al. 2014) and the HL paper

TE, EB, TB), and data (BK95xBK95, BK95xBK150, ..., BK150xPlanck353, etc.). See Buza 2019 for an example of such matrix. $\mathrm{vecp}(\boldsymbol{A})$ gets the vector of distinct components of a symmetric matrix $\boldsymbol{A}$. $g(\boldsymbol{A})$ is a function applied to the eigenvectors of $\boldsymbol{A}$, with :

$$g(x) = \mathrm{sign}(x-1)\sqrt{2(x-\ln x-1)} \tag{4.9}$$

X_g is then a vector with the dimension of all possible (N) auto and (N(N-1)/2) cross-bandpowers times the number of bandpowers (here, M=9), i.e M N(N+1)/2.

The BPCM $\mathcal{M}$ is computed from the signal S and noise $\mathcal{N}$ simulations, described previously. It is composed of six terms of possible signal and noise combination:

- sig = signal-only terms $\mathrm{Cov}(S_i \times S_j, S_k \times S_l)$;
- noi = noise-only terms $\mathrm{Cov}(\mathcal{N}_i \times \mathcal{N}_j, \mathcal{N}_k \times \mathcal{N}_l)$;
- sn1 = signal×noise terms $\mathrm{Cov}(S_i \times \mathcal{N}_j, S_k \times \mathcal{N}_l)$;
- sn2 = signal×noise terms $\mathrm{Cov}(S_i \times \mathcal{N}_j, \mathcal{N}_k \times S_l)$;
- sn3 = signal×noise terms $\mathrm{Cov}(\mathcal{N}_i \times S_j, S_k \times \mathcal{N}_l)$;
- sn4 = signal×noise terms $\mathrm{Cov}(\mathcal{N}_i \times S_j, \mathcal{N}_k \times S_l)$.

The indices i, j, k, l run over the experimental frequency channels. The average signal bandpowers from the simulations is stored. For a new fiducial model and noise model, we can compute new bandpower expectation values and rescale the corresponding terms of the BPCM by the appropriate power of the ratio of the new to old bandpower[6]. With only 499 simulations, some of the noisy estimates in the covariance matrix are set to zero. All this is described in CMB-S4 collaboration 2022, or in great details in Victor's thesis (Buza 2019).

4.3.2 BK15 likelihood analysis

The previous section described the generic likelihood used in BK analysis. Here we will describe some specificities of its implementation for BK15 (Keck Array and BICEP2 Collaborations et al. 2018). In BK15, the likelihood model has a cosmological component and a foreground component.

The cosmological component is

$$\mathcal{D}_{\ell,BB}^{\nu_1\times\nu_2} = \frac{r}{0.1}\mathcal{D}_{\ell,BB}^{\mathrm{tensor}} + A_L\mathcal{D}_{\ell,BB}^{\mathrm{lensing}} \tag{4.10}$$

where $\mathcal{D}_{\ell,BB}^{\mathrm{lensing}}$ and $\mathcal{D}_{\ell,BB}^{\mathrm{tensor}}$ are generated using `CAMB` (A. Lewis et al. 2000).

The foreground model contains a dust, synchrotron and a correlated dust-synchrotron component :

---

[6] Note that, after checking its negligible impact, when sampling the likelihood, we do not update the BPCM for every parameter step, just once for a given model.

$$\mathscr{D}_{\ell,BB}^{\nu_1\times\nu_2} = A_{\rm d}\Delta'_{\rm d} f_{\rm d}^{\nu_1} f_{\rm d}^{\nu_2}\left(\frac{\ell}{80}\right)^{\alpha_{\rm d}} + A_{\rm sync}\Delta'_{\rm s} f_{\rm s}^{\nu_1} f_{\rm s}^{\nu_2}\left(\frac{\ell}{80}\right)^{\alpha_{\rm s}} + \epsilon\sqrt{A_{\rm d}A_{\rm sync}}(f_{\rm d}^{\nu_1} f_{\rm s}^{\nu_2} + f_{\rm s}^{\nu_1} f_{\rm d}^{\nu_2})\left(\frac{\ell}{80}\right)^{(\alpha_{\rm d}+\alpha_{\rm s})/2} \tag{4.11}$$

where ν_1 and ν_2 are two given frequencies, $f_{\rm d}$ and $f_{\rm s}$ are the spectral scaling of the dust and synchrotron (see eq 2.17 and 2.18), defined precisely for instance in CMB-S4 Collaboration 2020. Since dust and synchrotron polarization arise from complex galactic processes that are to some unknown extent correlated, we model this with a correlation parameter ϵ. $\Delta'_{\rm d}$ and $\Delta'_{\rm s}$ are decorrelation parameters. $A_{\rm d}$ is the dust power in μK^2 at a pivot frequency of 353 GHz. $A_{\rm sync}$ is the synchrotron power at a pivot of frequency of 23 GHz. both are defined at $\ell = 80$. and the ℓ dependence is a power law with slope $\alpha_{\rm d}$ and $\alpha_{\rm s}$, defined in terms of $\mathscr{D}_\ell \equiv \ell\,(\ell+1)\,C_\ell/2\pi$. Note also that we do not fit for synchrotron decorrelation in BK15.

In BK15, we ignore CMB temperature and mostly only use BB spectra. In some variants of the likelihood we also include EE and EB spectra, in which case we model the E foregrounds the same way as the B ones, but scaling the dust and synchrotron powers $A_{\rm d}$ and $A_{\rm sync}$ by EE/BB = 2, which is compatible with observation by Planck and SPASS (Planck Collaboration 2020b and Krachmalnicoff et al. 2018).

4.4 BK15 results

4.4.1 Baseline analysis

In the baseline analysis of BK15, we use all BICEP2 and Keck data until 2015, i.e as we have seen in 2.3, 14 receiver-years at 150 GHz, 4 at 95 GHz and 2 at 220 GHz. We also use the 23 and 33 GHz bands of WMAP and the seven polarized bands from Planck (30, 44, 70, 100, 143, 217 and 353 GHz). We only use the first nine bandpowers described above. The bandpowers are shown in figure 4.4.

We use the eight-parameter likelihood defined above, which we explore using a Markov Chain Monte Carlo (MCMC), specifically `COSMOMC` (Antony Lewis and Bridle 2002). The parameters and priors are summarized in table 4.1. We apply priors on the spectral indices of dust β_d (Keck Array, BICEP2 and Planck Collaborations 2015 and P. A. R. Ade et al. 2015) and synchrotron β_s (Fuskeland et al. 2014). In `COSMOMC`, we can not use a model with non-physical r<0 values. As discussed briefly in the BK15 paper, these priors could induce biases. We illustrate this in figure 4.5.

To check that our priors do not introduce any biases, we run `COSMOMC` on our 499 simulations, and we see that half of the results were peaking at 0 and the other half was peaking above 0 (see figure 19 of Keck Array and BICEP2 Collaborations et al. 2018). Note that we also fix the tensor spectral index $n_T = 0$, and the lensing amplitude A_L to the one predicted by ΛCDM. We also assume no dust nor synchrotron decorre-

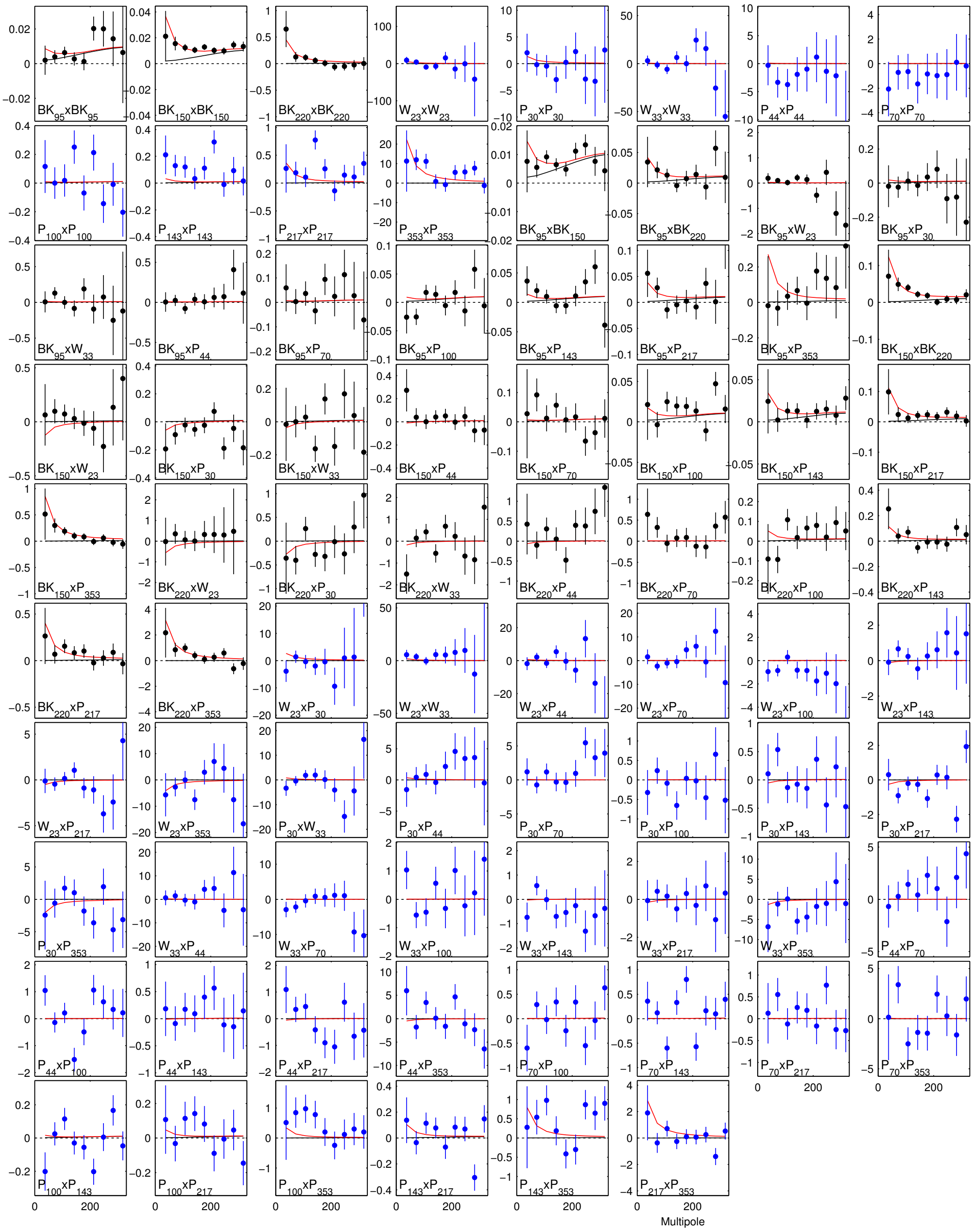

Figure 4.4: Full set of BB bandpowers ($100\ell C_\ell/2\pi$ in μK^2). Black spectra involve BK data, blue are fully external data. The black curve is a lensing only signal, whereas the red one includes a foreground model. Figure extracted from Keck Array and BICEP2 Collaborations et al. 2018.

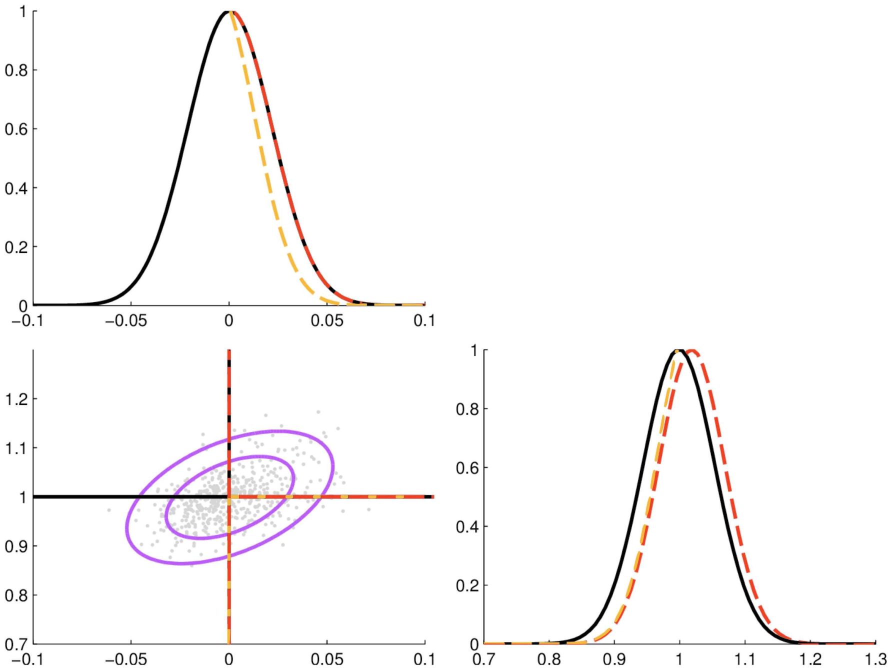

Figure 4.5: In this toy model, we have a distribution of two correlated parameters. If we marginalize over the full range, we have unbiased measurements, but if we restrict to the positive part of the top parameter (red), we can bias the fit of the parameter on the right. If we restrict to the top>0 and right<1, we can bias both parameters (yellow).

lation. The full `COSMOMC` parameter file, defining all of these including convergence parameters are available here `http://bicepkeck.org/bk15_2018_release.html`.

Another much quicker algorithm is used in our pipeline, which finds the maximum of the likelihood using `MINUIT` (James and Roos 1975). This can be run on our suite of 499 simulations (lensed-ΛCDM+dust+noise) to check that we recover the input cosmology. This is indeed the case, as see in figure 20 of the BK15 paper.

In the following, we will report the peak value of the likelihood as well as lower and upper limit obtained from the 1D marginal likelihoods, i.e. the parameters boundaries for which the integral of the curve encompasses 68% of the curve, going down from the peak. We also find the 95% limit from the cumulative distribution of the normalized marginal distribution. We sometimes report the ratio R of the likelihood at 0 and at peak, Wilks theorem (Wilks 1938) tells us that $\chi^2 = -2\log(R)$, we can then get the probability to exceed PTE = 1/2 (1-cdf), from which we can obtain the significance using the quantile function. The description of these results is largely taken from the BK15 paper.

A selected projection of this 8 dimensional likelihood is shown in figure 4.6. We get $r_{0.05} = 0.020^{+0.021}_{-0.018}$, with $r_{0.05} < 0.072$ at 95% confidence, $A_{\mathrm{d},353} = 4.6^{+1.1}_{-0.9}\,\mu\mathrm{K}^2$, and $A_{\mathrm{sync},23} = 1.0^{+1.2}_{-0.8}\,\mu\mathrm{K}^2$, ($A_{\mathrm{sync},23} < 3.7\,\mu\mathrm{K}^2$ at 95% confidence). For r, the zero-to-peak

Parameter	Unit	Description	Prior
r	-	Tensor to scalar power ratio, at a pivot scale of 0.05 Mpc^{-1}	Flat prior [0,0.5]
$\boldsymbol{A_d}$	[μK^2]	Dust amplitude, at $\ell = 80$ and ν=353 GHz	Flat prior [0,15] μK^2
$\boldsymbol{A_s}$	[μK^2]	Synchrotron amplitude, at $\ell = 80$ and ν=23 GHz	Flat prior [0,50] μK^2
$\boldsymbol{\beta_d}$	-	Dust spectral index	Gaussian prior $\mathcal{N}(1.59, 0.11)$ x flat prior [1.04,2.14]
$\boldsymbol{\beta_s}$	-	Synchrotron spectral index	Gaussian prior $\mathcal{N}(-3.1, 0.3)$ x flat prior [-4.5,-2.0]
$\boldsymbol{\alpha_d}$	-	Dust power spectrum power law index	Flat prior [-1,0]
$\boldsymbol{\alpha_s}$	-	Synchrotron power spectrum power law index	Flat prior [-1,0]
$\boldsymbol{\epsilon}$	-	Dust-Synchrotron correlation	Flat prior [-1,1]

Table 4.1: Table of the baseline likelihood parameterization of BK15

likelihood ratio is 0.66, i.e. we have a probability to get a likelihood ratio smaller than this is 18% if, in fact, r = 0. This was at the time by far the strongest limit put on r, and from B-modes alone!

The maximum likelihood model, using the same priors, but without the $r > 0$ physical constraint, has parameters $r_{0.05} = 0.020$, $A_{\mathrm{d},353} = 4.7\,\mu\mathrm{K}^2$, $A_{\mathrm{sync},23} = 1.5\,\mu\mathrm{K}^2$, $\beta_\mathrm{d} = 1.6$, $\beta_\mathrm{s} = -3.0$, $\alpha_\mathrm{d} = -0.58$, $\alpha_\mathrm{s} = -0.27$, and $\epsilon = -0.38$. This model has a probability to exceed the χ^2 of 0.19, which is acceptable. When running maximum likelihood searches on the 499 signal+noise simulations we find that $\sigma(r) = 0.020$.

4.4.2 Analysis variations

We also explored many variations from the baseline analysis choices and data selection and these did not significantly change the results. All of this is detailed in the appendices of Keck Array and BICEP2 Collaborations et al. 2018 and the summary here is inspired by the one we wrote in the main part of the paper.

Lifting the Gaussian prior on β_d slightly broadens the r constraint curve and we get $r_{0.05} < 0.079$ (95%).

We also checked what constraint we get with BK data only. While the curve is of course larger, the peak position shifted down to zero resulting in $r_{0.05} < 0.063$. For this model, BK data is already at least as constraining as Planck for the high frequency "dust" channels, but still needs external low frequency "synchrotron" data.

Concerns have been raised by the referee that the known problems with the LFI maps (P. A. R. Ade et al. 2016) might affect the analysis—excluding LFI the r constraint

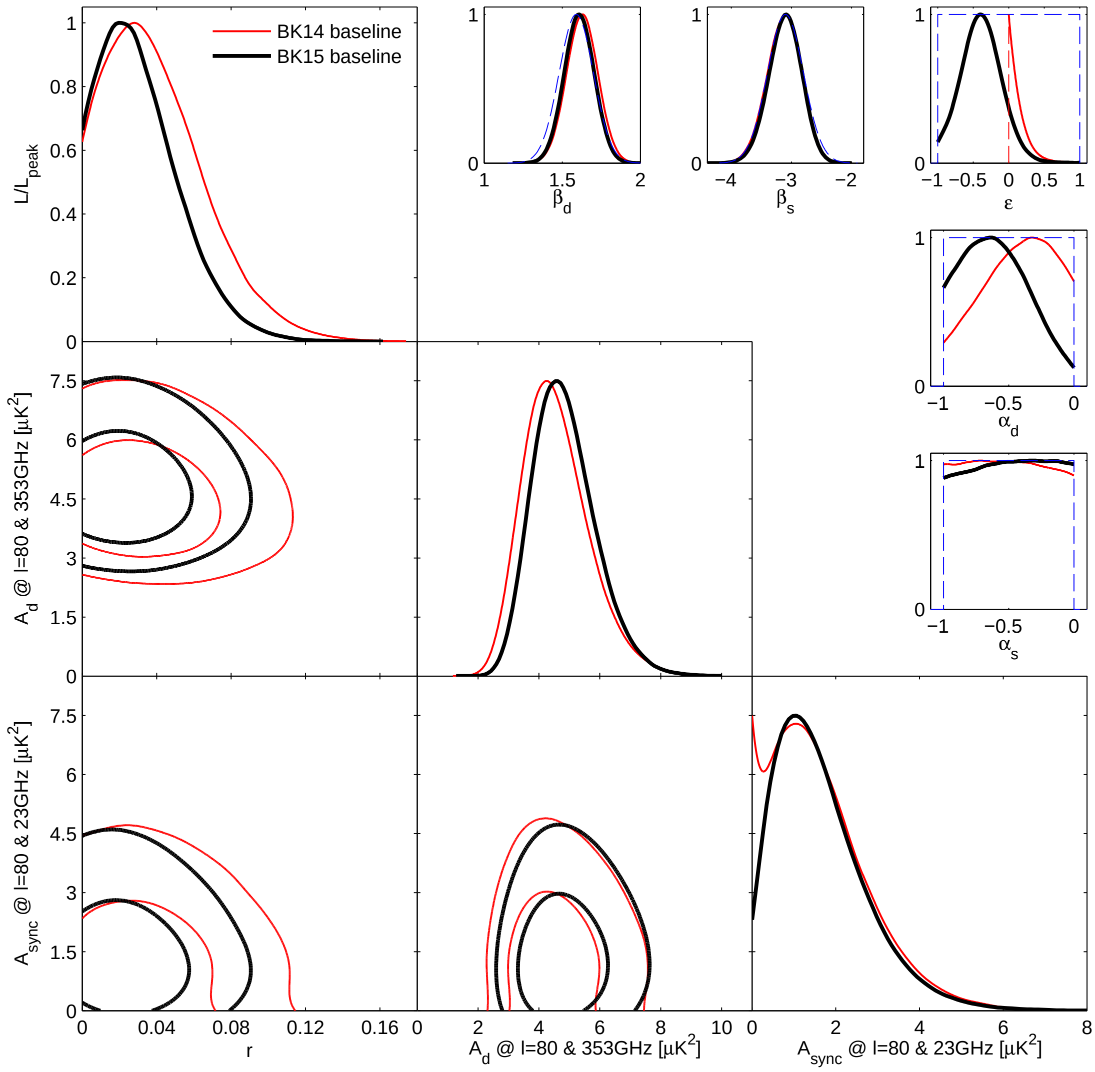

Figure 4.6: Projections of the BK15 `COSMOMC` likelihood. In thin red we show the previous results from Keck Array and BICEP2 Collaborations 2016b and in thick black, the BK15 results. The lower left corner plot shows the 2D marginalized constraints on r, A_d and A_s, whereas the other plots show the five other parameters, and their imposed prior in dashed blue. Figure extracted from Keck Array and BICEP2 Collaborations et al. 2018.

curve peak position shifts down to $r = 0.012^{+0.022}_{-0.012}$ ($r_{0.05} < 0.065$, with zero-to-peak likelihood ratio of 0.90, and 32% probability to get a smaller value if $r = 0$), while the constraint on $A_{\mathrm{sync},23}$ becomes $2.4^{+1.9}_{-1.4}\,\mu\mathrm{K}^2$.

We also checked many other dataset variations, and the shifts (e.g. omitting Planck) are not statistically significant when compared to shifts seen in our lensed-ΛCDM+dust+noise simulations.

Freeing the amplitude of the lensing power we obtain $A_{\mathrm{L}} = 1.15^{+0.16}_{-0.14}$, and detect lensing at 8.8σ significance, which was the strongest detection from B-modes alone at the time.

To check if a mis-parameterization of the foreground could induce biases, we used more complex foreground simulations from the PySM (Thorne et al. 2016 Hensley 2015) and some based on MHD simulations (Kritsuk et al. 2017). These models are not generated according to our foreground parameterization, and this could in general produce a bias on r. However, for the models considered we find that such bias is small compared to the instrumental noise.

Spatial variation of the frequency spectral behavior of dust leads to a decorrelation of the dust patterns as observed in different frequency bands. As introduced in section 2.2.1, while this decorrelation should exist, its level is unknown and debated, and here the question is how it compares to the current experimental noise. The baseline parametric model assumes a fixed dust pattern as a function of frequency, so such variation should lead to a bias on r.

We added a model variant, as seen in 4.11 that includes a decorrelation parameter. To check our framework, We generated a simulation with high decorrelation according to our model and were able to recover the input parameter in our likelihood analysis. Using this new model variant only increases $\sigma(r)$ from 0.020 to 0.021, but for the present dataset this parameter is partially degenerate with r and including it results in a downward bias on r in simulations.

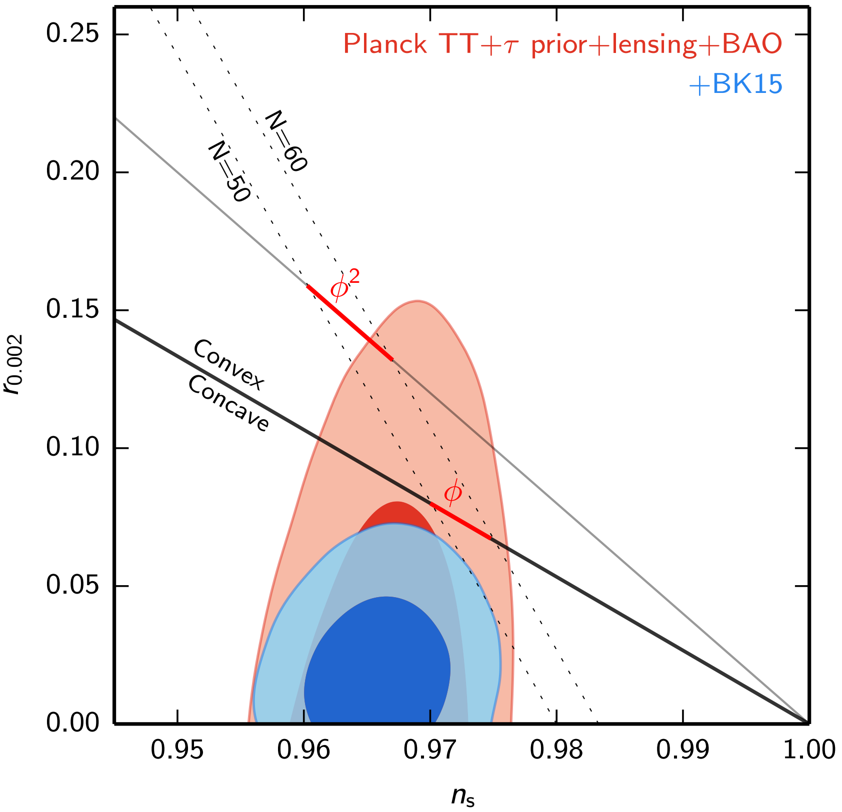

Figure 4.7: r versus n_s constraints from BK15 data together with external data from the Planck 2015 chains (Planck Collaboration XII 2016), but with a τ prior from N. Aghanim et al. 2016 instead of the use of large scale polarization, as recommended by the Planck team, before the Planck 2018 was out.

Another very important work, done by Victor Buza, is to combine the BB data presented here with the Planck + BAO chains. This allows to put joint constraints on r and n_s, which is a one of the parameter spaces where different models of inflation behave differently[7]. Figure 4.7 shows the constraints in the r versus n_s plane for Planck 2015 plus additional data ($r_{0.05} < 0.12$) and when adding in also BK15 ($r_{0.05} < 0.062$). These were at the time the strongest constraints on r. For the first time, the $V \propto \phi^2$ and $V \propto \phi$ inflation models now were entirely outside of the 95% contour.

---

[7] As explained in chapter 1, we are here theory biased by focusing on inflation models, but constraining this parameter space is important for any early universe physics.

4.5 Going from maps to cosmology without explicit likelihood evaluation

Note that I here focused on the BK pipeline since this is what I worked on, the official SPIDER pipeline to go all the way to cosmology is different but follows the same principle: binned maps, absolute calibration using Planck, pseudo-spectrum that need to be bias corrected, jacknives studies, and then a multi-frequency multicomponent likelihood analysis. This is the most common way to measure cosmological parameters from maps.

Here I will very briefly summarize a project we did in Oslo together with Jeff Jewell from JPL. The goal was to avoid these different steps and estimate the cosmological parameters from the data without likelihood approximations.

As very well summarized in Ducrocq et al. 2022:

> An entire slew of very diverse methods have been designed to produce estimates of the temperature or polarization power spectra or estimates of the cosmological parameters from a set of noisy CMB maps. We can divide these in three broad categories. The first one includes the so-called pseudo-C_ℓ approaches, e.g., Upham et al. 2019; Hamimeche and Antony Lewis 2008; Hamimeche and Antony Lewis 2009; Grain et al. 2009; Hivon et al. 2002, which compute the power spectra directly from the observed noisy maps of the CMB sky. See Gerbino et al. 2020 for a review. The second category involves the maximum likelihood methods Gjerløw et al. 2015; Tegmark and Oliveira-Costa 2000, which maximize the likelihood of the observed CMB maps with respect to the sought-after coefficients of the CMB power spectra. The third category comprises the Bayesian approaches using Markov chain Monte Carlo (MCMC) sampling methods, which directly target the posterior distribution of the estimated parameters, such as power spectra, given the observed data. A number of such techniques exist and some have been applied either for the power spectra or cosmological parameter estimation. These include the Metropolis-Hastings sampler, (Antony Lewis and Bridle 2002; Wraith et al. 2009; Eriksen et al. 2008), the Hamiltonian Monte Carlo sampler (Taylor et al. 2008, Hajian 2007), or the Gibbs sampler (Eriksen et al. 2004; Larson et al. 2007; B. Racine et al. 2016; J. B. Jewell et al. 2009; Wandelt et al. 2004).

While BK analysis uses pseudo-C_ℓ approach, our method in B. Racine et al. 2016 was in the third category, trying to directly estimate for cosmological parameters from the "map" data.

We can model our data vector $\boldsymbol{d}$ in pixel space, i.e. our observed CMB map, as:

$$\boldsymbol{d} = \mathbf{A}\boldsymbol{s} + \boldsymbol{n} \tag{4.12}$$

where $\mathbf{A}$ is a transformation matrix (simplest case would be beam filtering, but masks could be here too). $\boldsymbol{s}$ is the CMB signal with power spectrum C_ℓ which depends on cosmological parameters θ. $\boldsymbol{n}$ is the instrumental noise, with covariance $\boldsymbol{N}$. Our goal is to reconstruct $P(C_\ell|d)$. Using Bayes' theorem, the problem boils down to sampling $P(C_\ell, \boldsymbol{s}|\boldsymbol{d})$.

The basic idea behind Gibbs sampling is to draw a sample from the joint posterior $P(C_\ell, \boldsymbol{s}|\boldsymbol{d})$ by iteratively sampling from the corresponding conditional probabilities,

$$\boldsymbol{s}^{i+1} \leftarrow P(\boldsymbol{s}|C_\ell^i, \boldsymbol{d}) \tag{4.13}$$

$$C_\ell^{i+1} \leftarrow P(C_\ell|\boldsymbol{s}^{i+1}, \boldsymbol{d}). \tag{4.14}$$

These distributions can be computed, (see for instance in J. B. Jewell et al. 2009):

$$P(C_\ell|\boldsymbol{s}) \propto P(C_\ell) \frac{e^{-\frac{1}{2}\boldsymbol{s}_\ell^t \boldsymbol{S}_\ell^{-1} \boldsymbol{s}_\ell}}{\sqrt{|\boldsymbol{S}_\ell|}} = P(C_\ell) \frac{e^{-\frac{2\ell+1}{2}\frac{\sigma_\ell}{C_\ell}}}{C_\ell^{\frac{2\ell+1}{2}}}, \tag{4.15}$$

which is the inverse Gamma distribution as a function of C_ℓ. $\sigma_\ell = \frac{1}{2\ell+1}\sum_m |a_{\ell m}|^2$ denotes the observed power spectrum of $\boldsymbol{s}$.

As shown in J. Jewell et al. 2004 the conditional sky signal density can be written as

$$P(\boldsymbol{s}|C_\ell, \boldsymbol{d}) \propto e^{-\frac{1}{2}(\boldsymbol{s}-\hat{\mathbf{s}})^t(\mathbf{S}^{-1}+\mathbf{A}^{\mathrm{t}}\mathbf{N}^{-1}\mathbf{A})(\boldsymbol{s}-\hat{\mathbf{s}})}, \tag{4.16}$$

where $\hat{\mathbf{s}} \equiv (\mathbf{S}^{-1} + \mathbf{A}^{\mathrm{t}}\mathbf{N}^{-1}\mathbf{A})^{-1}\mathbf{A}\mathbf{N}^{-1}\boldsymbol{d}$ is the mean-field map (or Wiener filtered data). Thus, $P(\boldsymbol{s}|C_\ell, \boldsymbol{d})$ is a Gaussian distribution with mean equals to $\hat{\mathbf{s}}$ and a covariance matrix equals to $(\boldsymbol{S}^{-1} + \boldsymbol{A}^t\boldsymbol{N}^{-1}\boldsymbol{A})^{-1}$. J. Jewell et al. 2004 also introduces a way to generate such samples.

The issue arises when we want to draw C_ℓ's. When sampling equation 4.15, the step size is determined by the C_ℓ themselves or rather their cosmic variance. This works well in high signal-to-noise, but not in the low signal-to-noise, where the width of the posterior is determined by a mix of cosmic variance and instrumental noise. This is illustrated in figure 4.8.

In our method, we replaced the step from 4.15 by a joint move where we generate C_ℓ and rescale the map generated with eq. 4.16 according to :

$$\boldsymbol{s}^{i+1} = \hat{\boldsymbol{s}}^{i+1} + \sqrt{\frac{\boldsymbol{C_\ell}^{i+1}}{\boldsymbol{C_\ell}^{i}}}(\boldsymbol{s}^i - \hat{\boldsymbol{s}}^i) \tag{4.17}$$

Instead of sampling the C_ℓ multipole-by-multipole, we can even directly sample at cosmological parameter level using the proposal :

$$w(\theta^{i+1}|\theta^i) = e^{-\frac{1}{2}(\theta^{i+1}-\theta^i)^t\mathbf{C}_{\boldsymbol{\theta}}^{-1}(\theta^{i+1}-\theta^i)}, \tag{4.18}$$

where $\mathbf{C}$ can be a parameter covariance matrix derived from some earlier cosmological analysis.

Overall, as written in B. Racine et al. 2016, the full sampler therefore works as follows:

1. Propose some initial parameter vector θ^0, and generate a power spectrum C_ℓ^0 with `CAMB`. Solve Eq 4.16, or rather equations 11 and 12 of the paper to get the map $\boldsymbol{s}(\theta^0)$.
2. Propose a new parameter vector θ^1 according to the proposal rule w, and compute the corresponding power spectrum C_ℓ^1.
3. Compute the deterministically rescaled map using equation 4.17, and evaluate the accept probability according to equation 18 of the paper; accept or reject the proposal according to the usual Metropolis-Hastings rule.
4. Given the most recent parameter sample, make a standard conditional Gibbs step for the sky map, according to equation 4.16, and compute a new map.
5. Iterate 2–4.

The algorithmic trick presented above allows us to sample our distribution with steps that are now following the real shape of the posterior in any signal over noise regime, as sketched in figure 4.8. We validated our algorithm on simulations using our own MCMC sampler. For more details, refer to B. Racine et al. 2016.

With this method, we do not need to correct for biases as we do in the pseudo-C_ℓ case, we do not need to approximate likelihoods like is needed in the maximum likelihood methods. And this novelty of directly sampling cosmological parameters makes it more physical (even though we could switch to sampling the C_ℓ if needed). This is also well suited for a full Bayesian analysis including component separation, or even TOD filtering. It is used in the `Commander` framework (see `https://docs.beyondplanck.science/#/05_bibliography/index?id=commander-method-papers`), mentioned in the SPIDER chapter.

4.6 My contributions

When I joined the Kovac Lab, the BK15 data were ready to be analyzed. No-one had looked at the B-mode data in detail yet. Before unblinding the data, Victor Buza and I ran the full multicomponent analysis on a few selected simulations of the BK15 dataset. We tested the effect of applying different priors on the decorrelation parameter, introduced for the first time in the model (by Victor Buza and Colin Bischoff), and of new priors on the dust-synchrotron correlation. We also designed all the plots we wanted to put in the BK15 paper, what kind of variations of the data, the model, etc. we wanted to show.

I then ran the analysis on the real BK15 data. This led to figures 3, 4, 15 to 18, and 20 to 22 of Keck Array and BICEP2 Collaborations et al. 2018 and the content of the corresponding text. This is what is also summarized in section 4.4

I then did a few studies, for instance:

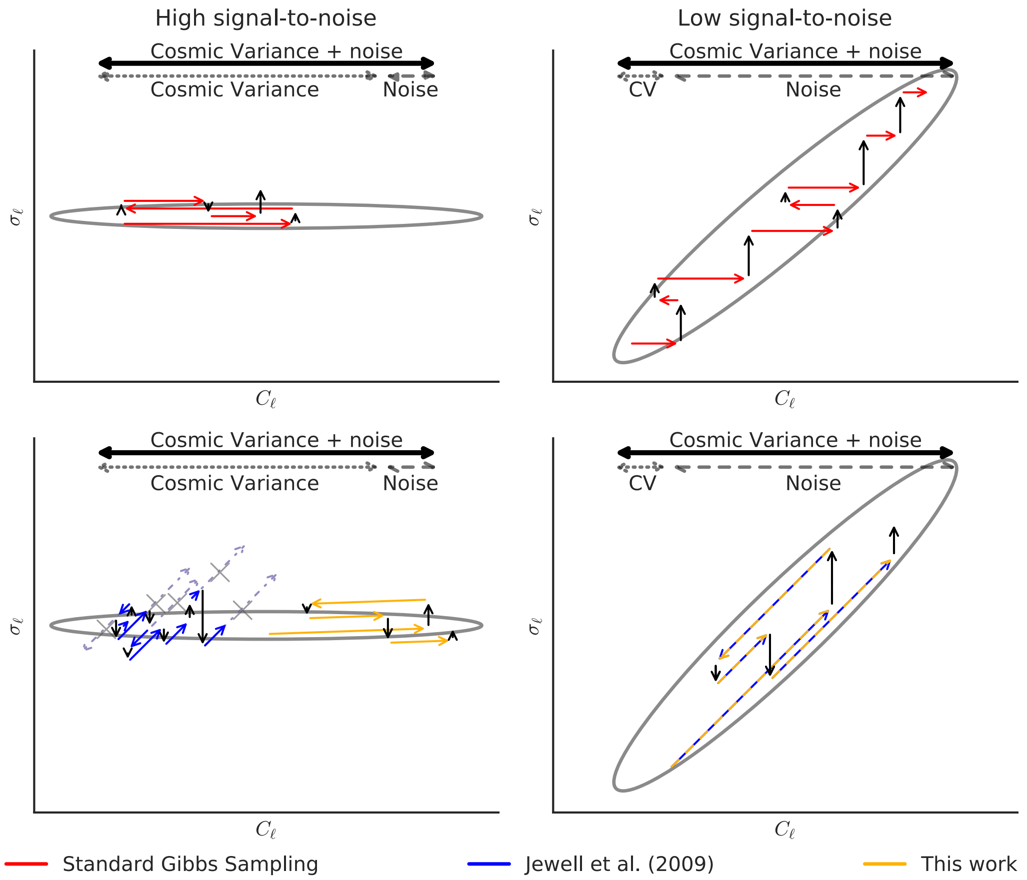

Figure 4.8: Illustration of the performance of different sampling algorithms in different signal-to-noise regimes. We sketch the exploration of the joint distribution of proposed C_ℓ and the signal map's power spectrum $\sigma_\ell = 1/(2\ell+1)\sum|s_{\ell m}|^2$. In the high signal-to-noise limit (left column), standard Gibbs sampling steps (in red) achieve both good acceptance rates and correlation lengths. In the low signal-to-noise limit (right column), the cosmic variance, and therefore the step length, is much smaller than the noise contribution to the posterior, and standard Gibbs sampling results in a long correlation length. Joint sampling steps in which the sky map is rescaled by the power spectrum, as proposed by J. B. Jewell et al. 2009 is illustrated in blue. Our method is shown in yellow, in which we exclude the high signal-to-noise Wiener filter component of the signal from the rescaling operation, and only modify the fluctuations around this mean-field map. The net result is an algorithm that works in both low and high signal-to-noise regimes.

- Showed that the width of the flat priors of A_s on the r constraints for BK data only was negligible.

- Checked that the shift due to opening decorrelation on data was compatible with our simulations that didn't contain decorrelated dust. It was actually marginally significant. I showed that it was not due to the cross-spectrum between BK95 and Planck 353 GHz, as was suggested in the team. I also studied if it could be due to the prior on ϵ, but our simplest simulations did not contain synchrotron, so it was inconclusive. Using more complex magnetohydrodynamic simulations that contained correlated dust and synchrotron, the shift was not remarkable anymore. In the next round of analysis, they included synchrotron in the simulations.

- I also applied the likelihood to all our simulations, letting the decorrelation parameter free, and showed in a plot similar to figure 19 of Keck Array and BICEP2 Collaborations et al. 2018, that even with no decorrelation in the simulation, there is a preferred shift of r towards 0, due to the imposed physical boundaries (r>0 and Δ_d<1) on correlated parameters. This is what we see in my figure 4.5, in yellow. By repeating figure 19 of Keck Array and BICEP2 Collaborations et al. 2018 with decorrelation fit, we see that now 72% of the r curves peak at 0 and many of the decorrelation Δ'_{d} peak at 1. This is one of the reasons why we did not include decorrelation in the baseline.

- I worked on relaxing the constraints on EE/BB ratio when including E data and measured the we are compatible for EE/BB = 2 for the dust, but not constraining for synchrotron. We were seeing a shift in r on the high end of what was seen in simulations and it was suggested that EB could be a source of it. I studied the effect of zeroing the EB spectra to see its impact, but this made me realize that we had some biases in our bandpowers, that were negligible in BB but not anymore in EE. This was not easy to fix in the pipeline at the time and has been improved since I left but still under study.

- I then worked on a detailed study of the BK survey weight, map depth, and effective f_{sky} at bandpower level, as summarized in section 4.2. This is an important piece for the CMB-S4 forecasting (see next chapter) and was also a good metric for all BK sub-datasets.

- In addition to all the data and model variations I studied for BK15 paper, I studied in detail our detection of gravitational lensing from BB only. I used `COSMOMC`, letting the lensing amplitude free, with and without Planck prior, and generated a new figure for the BK15 paper. I also used the maximum likelihood method on simulations to study the effect on $\sigma(r)$ and our $\sigma(A_L)$. I used a technique "increasing the temperature" of the MCMC, i.e. forcing to explore the parameter space with larger jumps, to explore the tail of the marginal likelihood and get a precise zero-to-peak likelihood ratio to compute our detection significance properly. We had a 8.8σ detection, which was the strongest to date using B-modes only.

- I also ran maximum likelihood on simulations for all the possible data variations we presented in the paper, to get $\sigma(r)$ for all data combination.
- Answering the referee for BK15, I also showed that our first bandpower alone can put strong constraints on r and showed that changing the priors on the α parameter had negligible effect.
- I also studied how the noise in our maps depends on the elevation and compared it to prediction from analytical tools we use in CMB-S4.

For the project on sampling cosmological parameters from maps, the idea stemmed from Jeff Jewell, who had been working on similar issues a few years before, while Hans Kristian and Ingunn were the local experts in Oslo on this Gibbs sampling for CMB. I wrote the full code and the paper, with Jeff's contribution mostly on the statistical aspect of appendix A.2.

5 Future of the CMB

Sommaire

To search for very faint signals in the microwave sky such as the primordial B-modes, we need to have a multi-frequency, multi-scale observation with the best possible sensitivity, i.e. involving many thousands of detectors in multiple telescopes. This is one of the goal of the CMB-S4 collaboration.

In this chapter, I will describe what is the observational status of the B-modes and then describe my work in Harvard, as one of the most active members of the CMB-S4 B-modes forecasting group. Some of this work is reported the next section, the rest being mostly shown in public postings [1] and collaboration meetings.

5.1 Summary of B-modes experiments in 2022

As we discussed in the last chapter, BICEP2/Keck results using all available data up to 2015 put the very tight constraints on primordial gravitational waves. Since then

---

[1] `https://cmb-s4.uchicago.edu/wiki/index.php/Simulation_and_Forecasting_Logbook`

the collaboration published new results (BK18, Keck Array and BICEP2 Collaborations 2021), using data from 2011 to 2018, from BICEP2, BICEP3 and Keck Array experiments. There are also other instruments measuring the polarized CMB, and in this section, we will summarize the main ones.

While BICEP/Keck is targeting the large scale primordial B-modes, other bigger telescopes are observing smaller scales where the lensing B-modes dominate. While we here focus on B-modes, these large-aperture telescopes make high resolution temperature and polarization maps, sensitive to many secondary anisotropies (lensing, Sunyaev-Zeldovitch effect from clusters, etc.) which can be correlated to the optical and infrared surveys. This can allow to measure the mass of neutrinos, test models of dark energy, study galaxy evolution as well as the reionization era.

The B-mode summary plot is in figure 5.1. As we have seen in chapter 2, these are located in high altitude, dry areas, and they target different scales and frequencies. These are so called Stage-2 experiments, with $\mathcal{O}(1000)$ detectors.

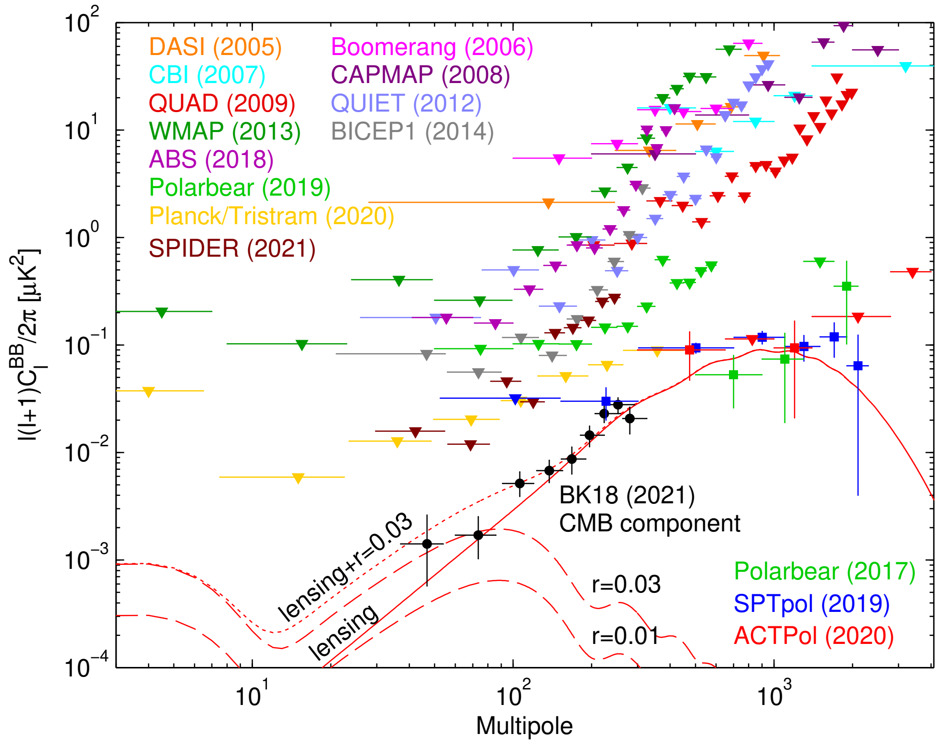

Figure 5.1: Most recent measurements, as of Fall 2021, extracted from Keck Array and BICEP2 Collaborations 2021.

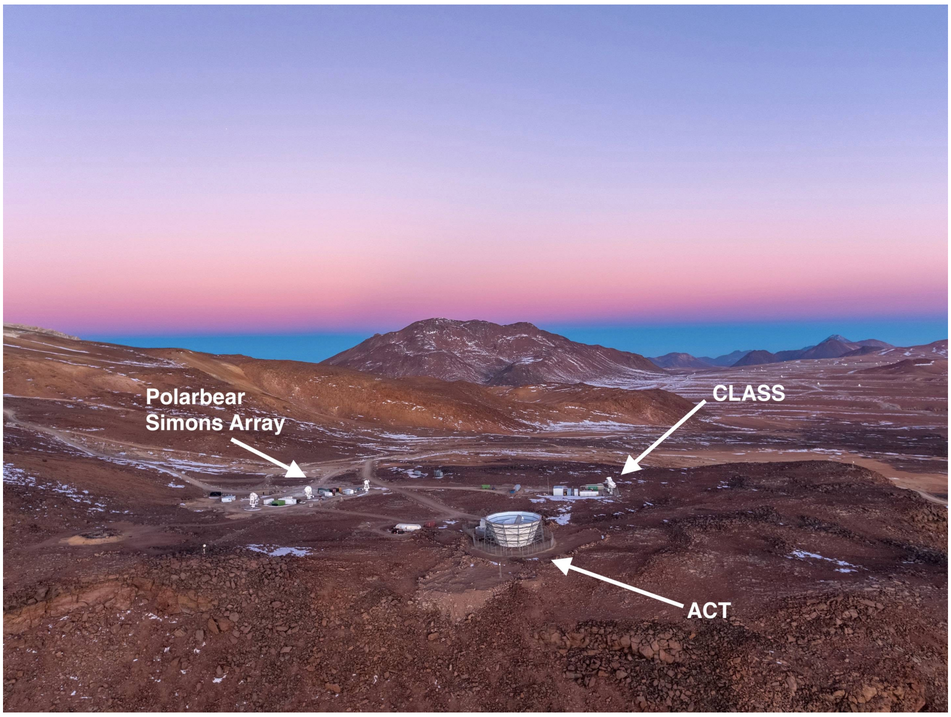

Figure 5.2: CMB observatory at the Cerro Toco in Atacama desert in Chile, altitude: 5190 meter. Credit: Debra Kellner

Figure 5.3: CMB observatory at the Amundsen–Scott South Pole Station in Antartica, altitude: 2835 meter. Credit: Sasha Rahlin

5.1.1 Stage-2 experiments with published results

BICEP3 and BICEP Array

While the results presented in the previous chapter are based on the BICEP2 and Keck Array telescopes, these telescopes have now been replaced by newer larger refractor telescopes, BICEP3 and the BICEP Array, which can be seen in figure 5.3. BICEP3 consists of 2500 Antenna-coupled transition-edge sensor bolometers in a larger optical tube (52 cm diameter), observing at 95 GHz. BICEP Array has a larger mount containing 4 wide-field receivers, at 30/40 GHz, 95 GHz (already observing), 150 GHz, and 220/270 GHz (planned detector deployment can be found here Moncelsi et al. 2020).

South Pole Telescope (SPT)

SPT is a 10 m telescope located at the Amundsen–Scott South Pole Station in Antarctica, on the same building as the BICEP3 (previously BICEP2) telescope, as is seen in figure 5.3. Its current version, SPT-3G, consists of more than 16000 lenslet-coupled detectors at 90, 150 and 220 GHz (Benson et al. 2014; Sobrin et al. 2021).

Atacama Cosmology Telescope (ACT)

ACT is a 6 m telescope located at the Cerro Toco in Atacama desert in Chile, at an altitude of 5190 m, as can be seen in figure 5.2, with its ground shield. Its current version, AdvACT, consists of more than 5000 bolometers coupled with spline-profiled feedhorns on multichroic arrays at 27/39 GHz, 90/150 GHz, and 150/230 GHz (Simon et al. 2016; Henderson et al. 2016)

POLARBEAR/Simons Array

POLARBEAR-1 is an off-axis Gregorian telescope, in Atacama, with a 2.5 m primary mirror. With three more 3.5 m diameter telescopes, Simons Array will observe with more than 20000 detectors at 95 GHz, 150 GHz and 220 GHz Stebor et al. 2016; Arnold et al. 2014; Suzuki et al. 2016. POLARBEAR-2a has been deployed with an ambient temperature half-wave plate (HWP), and 2b and 2c will have cryogenically cooled HWP.

5.1.2 Future stage-2 B-modes experiments

Here we review experiments that have not yet published B-modes results in 2022 but are observing or close to first light.

CLASS

The CLASS experiment, in Atacama, consists of one telescope at 40 GHz, two at 90 GHz, and a dichroic telescope observing at 150/220 GHz, respectively with 72, 512, and 2000 feedhorn-coupled bolometers (Essinger-Hileman et al. 2014). For now only the lowest frequency has been deployed. One of the main specificities of CLASS is a variable-delay polarization modulators (VPM), which modulates polarization and allows to remove a lot of the $1/f$ noise. This should allow a measurement of the really large scales, close to the reionization bump. To measure these modes, CLASS is observing 70 percent of the sky. This VPM also unlocks sensitivity to circular polarization (Stokes V).

QUBIC

QUBIC is a European lead telescope which is based on a new technique called bolometric interferometry (Hamilton et al. 2022). It uses a back-to-back horn array, which will allow the formation of interferences on two focal planes (each with 992 bolometers at 150 and 220 GHz). It combines the sensitivity of bolometers and the control of systematic errors thanks to the redundant measurements of interference baselines. Its frequency dependent beam should also allow for spectro-imaging, where a single band will have access to sub-band frequency resolution. This has been verified in the Technological Demonstrator (Torchinsky et al. 2022). The instrument has now been installed in Argentina, and the observatory was just inaugurated in November 2022.

5.1.3 Stage-3 B-modes experiments

Most of the experiments above are either at South Pole or on the same site in Atacama, see figure 5.2 and 5.3. While BICEP/Keck has now delivered very deep maps of the polarized CMB on large scales, we are now getting limited by the lensing B-modes. Stage-3 experiments combine degree-scale telescopes with much higher resolution ones to delens.

Simons Observatory (SO)

SO is an effort to put together the Atacama collaborations mentioned above to build new telescopes. The plan is to deploy a total of 60,000 dichroic polarization sensitive bolometers, evenly split between a one 6 m large-aperture telescope and three 0.5 m small-aperture telescopes. It will observe at 27, 39, 93, 145, 225 and 280 GHz to constrain galactic foreground and should constrain r with $\sigma(r) = 0.003$ (The Simons Observatory Collaboration 2018).

South Pole Observatory (SPO)

SPO puts together the SPT-3G and BICEP3/BICEP-Array collaborations combining existing facilities to design an ideal strategy to observe the CMB, using the large aperture SPT telescope to delens the small aperture telescopes maps.

5.2 Forecasting the stage-4 B-mode experiment

The next generation (stage-4) ground-based experiment (CMB-S4) aims at gathering SO and SPO into a mega-project at South Pole and in Atacama. It was conceived in the Snowmass Physics Planning exercise in 2013 and its concept has greatly evolved since then. The first extensive work was published in the CMB-S4 Science Book First Edition (CMB-S4 collaboration 2016), where a "Science Book Configuration" was laid out to set the science goals and estimate the necessary sensitivity.

I joined the CMB-S4 collaboration where we had to wrap up the first following iteration of the forecasts for the report of the Concept Definition Task force (CDT) (Lawrence et al. 2017) in which I participated in. After that, the goal was to refine the science case, and define the "reference design", to reach milestones from major public funding from the United States: the National Science Foundation (NSF) pre-conceptual design and Department Of Energy (DOE) critical decision CD-0. This lead to a major report introducing the reference design (CMB-S4 collaboration 2019b) as well as a summary published for the Astro2020 Decadal Survey Report (DSR) (CMB-S4 collaboration 2019a). We published this whole effort concerning the primordial B-modes into a separate, more detailed paper, the first official paper from the CMB-S4 collaboration: CMB-S4 Collaboration 2020.

CMB-S4 has many science goals, mentioned in section 5.1, with a very nice summary for instance in CMB-S4 collaboration 2019a. While some of these (neutrino science, relativistic species, etc.) require observation of a large part of the sky overlapping optical surveys, in this section, I will summarize the forecasting framework we used to define the baseline r survey, aiming the detection of primordial gravitational waves. The goal of this framework is to test what kind of configuration (number of telescopes, number of detectors at each frequencies, sensitivity of the detectors, siting: Chile versus Pole, etc.) will be needed to reach our science goal: detecting the B-modes at $r > 0.003$ at greater than 5σ or, in the absence of such signal, constrain $r < 0.001$ at 95% confidence level.

While most of the text here is re-written with a slightly different approach, it is highly inspired by our published works (CMB-S4 collaboration 2019a; CMB-S4 Collaboration 2020).

5.2.1 Summary of our forecasting

The CMB-S4 baseline r survey is evolving, based on our understanding of the impact of astrophysical foregrounds, instrumental systematics, delensing non-idealities, and analysis methodology. It is also highly constrained by budget limits. The forecasting effort is then naturally iterative, with steps as follows.

1. Develop a semi-analytic power-spectrum-level Fisher forecast, assuming noise performance scaled from analyses of real experiments.
2. Use this forecasting tool to optimize the allocation of detector effort across observing frequencies.
3. Use these configurations to create map-based data challenges (DCs) for validation.
4. Estimate science parameters from the DC maps with independent component-separation analysis methods.
5. Check that we recover analytic forecasts, in terms of variance and bias.
6. Iterate steps 1–5, injecting increasing realism.

I worked mostly on step 4-5 of the fourth Data Challenge (DC-4), and on the following step-1, where we included more realistic observing strategies for Pole and Chile.

In our forecasting paper, we followed the chronology. We described **the early Fisher forecast**, which was used to define the number of detectors needed at each frequency, and was the input to generate the maps from step 3. We then at the end describe **the late Fisher forecast**, which used more realistic observing strategies at Chile and Pole and was used to decide of the siting of the telescope. Here I will separate the Fisher forecast from the map based analysis, breaking a bit of the chronology. I will underline when necessary the difference between the two versions of the Fisher forecast.

For the map based analysis, we had two pipeline. One, developed by Raphael Flauger, was using the Internal Linear Combination (ILC) method (e.g., Tegmark and Efstathiou 1996), which determines the linear combination of multipole coefficients that minimizes the foreground and noise power without altering the CMB contribution. The other, which I worked on, building on previous work from Colin Bischoff, Victor Buza, Justin Willmert, Steve Palladino and others, was using a cross-spectrum likelihood based on the BK framework described in the previous chapter.

5.2.2 Semi-analytic Fisher Forecasting Framework

For the CMB-S4 Science Book (CMB-S4 collaboration 2016), people mostly based at Harvard developed a semi-analytic forecasting framework specifically targeted towards optimizing sensitivity to the tensor-to-scalar ratio, r, in the presence of Galactic foregrounds and gravitational lensing of the CMB.

Our forecasts rely on assuming that we can scale down the achieved noise (see section 4.2) based on increased detector count and integration time and that we can apply beam-size and Noise-Equivalent Temperature (NET) rescalings to account for the differences in experimental design.

As we have seen in chapter 4, Small Aperture Telescope (SAT) from BICEP/Keck are the only one to have reached the level of systematics control and noise performance necessary to pursue a ground-based, high-precision measurement of B-mode polarization down to low multipoles ($\ell \simeq 30$), targeting the $\ell \simeq 80$ peak from the polarization signature generated by primordial gravitational waves at the epoch of recombination. Therefore, to forecast the performance of next-generation SATs, the machinery is based on scaling the achieved performance of current published BK SATs, namely the bandpower covariance matrices (BPCMs, see 4.3.1) and noise power spectra (N_ℓ). This automatically builds into the forecast all real-world inefficiencies including (but not limited to): imperfect detector yield, non-uniform detector performance, read-out noise, observing inefficiency, losses due to timestream filtering, beam smoothing, and non-uniform sky coverage. For the delensing survey, mentioned after, we will use SPTPol performance.

At its core, the code is based on the BICEP/Keck parametric power-spectrum-based likelihood analysis (see section 4.3).

5.2.2.1 Fisher Formalism

Given a likelihood function of the form

$$L(\theta; d) \propto \frac{\exp\{[-\frac{1}{2}(d-\mu(\theta))^{\mathsf{T}}\Sigma(\theta)^{-1}(d-\mu(\theta))]\}}{\sqrt{\det(\Sigma(\theta))}}, \tag{5.1}$$

where d are the data bandpowers, θ are the theory parameters, and $\mu(\theta)$ and $\Sigma(\theta)$ are the bandpower expectation values and the bandpower covariance matrix given the parameters, we can calculate the expectation value of the log-likelihood curvature, evaluated at the position of the best fit model:

$$F_{ij} = -\left\langle \frac{\partial^2 \log L(\theta; d)}{\partial\theta_i \partial\theta_j} \right\rangle. \tag{5.2}$$

This quantity is called the Fisher information matrix. It measures how steeply the likelihood falls as we move away from the best-fit model, and F^{-1} can be thought of as the best possible covariance matrix for the measurement errors on the parameters θ_i.

Inserting Equation 5.1 into Equation 5.2 yields

$$F_{ij} = \frac{\partial\mu^{\mathsf{T}}}{\partial\theta_i}\Sigma^{-1}\frac{\partial\mu}{\partial\theta_j} + \frac{1}{2}\mathrm{Tr}(\Sigma^{-1}\frac{\partial\Sigma}{\partial\theta_i}\Sigma^{-1}\frac{\partial\Sigma}{\partial\theta_j}). \tag{5.3}$$

We then calculate our parameter constraints as

$$\sigma_i = \sqrt{(F^{-1})_{ii}}. \tag{5.4}$$

$\sqrt{(F^{-1})_{ii}}$ is the minimum obtainable standard deviation on the desired parameters (Cramér 1946; Kendall 1979; Tegmark et al. 1997). Note that we can add external priors of width σ_i to a given parameter θ_i by adding $P_i = 1/\sigma_i$ to F_{ii}.

Note that as we do for the BK analysis, we fix $\Sigma(\theta) = \Sigma$, making the second term of Equation 5.3 identically zero. While in most Fisher analyses, people build the covariance matrix from analytical models assuming some achievable observing efficiency, filterings, etc., here we scale our BPCM from the achieved BK one (see section 4.3).

To build the Fisher information matrix (eq 5.3), we need to build bandpower expectation values μ and the BPCM. We will first define a basic instrument setup, then scale the achieved performance from BK to this new instrument, use a fiducial model for the signal and potentially add priors.

Since the forecast uses scaled BICEP/Keck bandpower statistics, we use the same bandpower window functions (see section 4.1), as well as the nine multipole bins with width $\Delta\ell = 35$, with ℓ from 21 to 335.

5.2.2.2 Instrument definition

To be able to remove galactic foreground contamination, we want to cover as many frequencies as possible. As we have seen in section 2.2.4, ground-based experiments are limited to atmospheric windows due to oxygen and water opacity. We then defined 9 frequency bands which are shown in figure 5.4: 20, 30, 40, 85, 95, 145, 155, 220 and 270 GHz. Other configuration with 5 or 7 bands were tried in past iterations but proved to have more significant biases.

The 8 highest frequencies are on SATs with 0.52m aperture, based on the achieved BICEP3 technology. As we can see in the second line of table 5.1, the lowest frequencies have a large beam to stay diffraction limited. To avoid the very large beam to wash-out the signal out, it was decided to add the 20 GHz synchrotron channel on a Large Aperture Telescope (LAT)[2].

Note that the choice of split band around 90 and 150 GHz is a conservative decision to be more robust against complex foreground emissions[3].

The ideal per-detector NETs used later for scaling the noise for these telescopes are calculated with NETlib.py[4] at Cerro Toco (Chile) and South Pole. This code uses the 10-year MERRA2 median atmospheric profiles (Gelaro et al. 2017) as well as basic instrument models to compute the photon noise or the detector noise. To simplify, we use the average of NET calculated for detectors at the two sites. One of the departure from achieved performance is due to the fact that we here consider a focal plane cooled at 0.1 K instead of 0.25 K. For our 9 channels, ordered by increasing frequency, we get 214, 177, 224, 270, 238, 309, 331, 747 and 1281 $\mu K\sqrt{s}$.

---

[2] See the work reported here: `https://cmb-s4.uchicago.edu/wiki/index.php/Background_on_20_GHz_channel`.

[3] `https://cmb-s4.uchicago.edu/wiki/index.php/Simulation_and_Forecasting_Logbook` has several postings and presentation on this subject, including mine: `http://bicep.rc.fas.harvard.edu/CMB-S4/analysis_logbook/20190308_MLsearch_no85no145/`.

[4] Code here: `https://github.com/dbarkats/NET_forecast_python`, which can be used online here `https://cmb-s4.uchicago.edu/wiki/index.php/New_NET_Calculator_and_Validation`

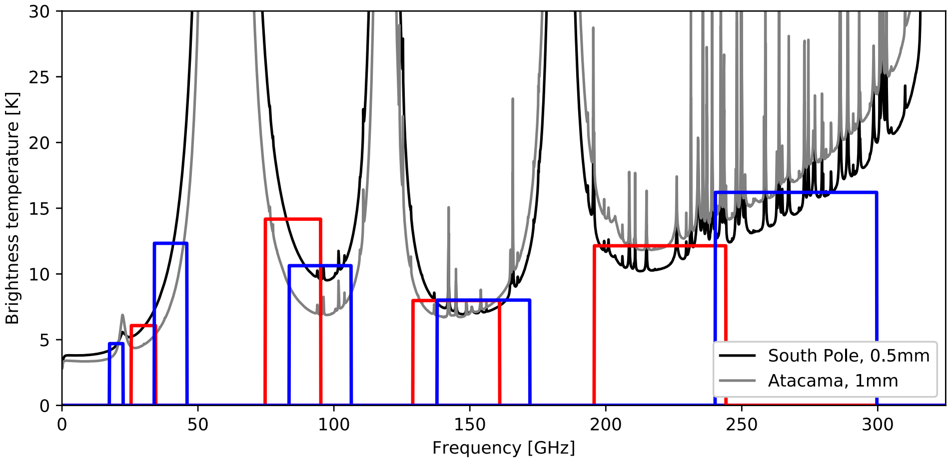

Figure 5.4: Calculated atmospheric brightness temperature spectra (at zenith) for the South Pole at 0.5 mm (PWV) and Atacama at 1.0 mm PWV (both are near the median values). Atmospheric spectra are generated using the am atmospheric model (Paine 2018). The top-hat bands, in red and blue, are plotted on top of these spectra, with the height of each rectangle equal to the band-averaged brightness temperature using the South Pole spectrum. Figure from our paper: CMB-S4 Collaboration 2020.

Table 5.1: Optimized instrument configuration for the r survey, as presented in the CMB-S4 CDT Report. The beam here is the FWHM in arcmin.

		Frequency [GHz]									
Item	20	30	40	85	95	145	155	220	270	DL	Total
N_{det}	130	260	470	17 k	21 k	18 k	21 k	34 k	54 k	84 k	250 k
Beam ...	11′	77′	58′	27′	24′	16′	15′	11′	8.5′	1.0′	

5.2.2.3 Noise Scaling

To build equation 5.3 for any CMB-S4 configuration, we will need to scale down the noise compared to current noise levels. This is done at the level of the covariance matrix. One of the advantages of keeping the six different terms of the BPCM separately, as seen in section 4.3, is that we can rescale the noise and signal separately. We will see in the next section how we treat the signal.

For frequencies already present in the BK datasets, we can simply multiply the BPCM components that contain a noise term using the appropriate power of the ratio of the noise that was used in the BK sims to the new noise for CMB-S4. For new frequencies, short of new results, we use the best proxy available, i.e. we expand the BPCM by adding new columns for the variance and covariance, based on the closest frequencies. For instance, if we add a channel at 145 GHz and one at 270 GHz, we will use the scaled variance from the achieved 220 and the 150 GHz from BK and their covariance will be scaled from 150x220 GHz.

To scale the BK noise spectra to CMB-S4 ones, we scale the survey weight, as well as the beam. The survey weight w will directly scale as the NET and the number of detectors times the number of years $n^{\mathrm{det-yr}}$, and we get :

$$N_{\ell,\mathrm{S4,forecasted}} = N_{\ell,\mathrm{BK,achieved}} \frac{n^{\mathrm{det-yr}}_{\mathrm{BK}}}{n^{\mathrm{det-yr}}_{\mathrm{S4}}} \frac{\mathrm{NET}^2_{\mathrm{S4,ideal}}}{\mathrm{NET}^2_{\mathrm{BK,ideal}}} \frac{B^2_{\ell,\mathrm{S4}}}{B^2_{\ell,\mathrm{BK}}} \tag{5.5}$$

where $B^2_{\ell,\nu} = e^{\frac{-\ell(\ell+1)\Theta^2_\nu}{8\log(2)}}$, Θ_ν is the FWHM in radians, of the Gaussian beam. Note that the BK simulations use non-Gaussian beams, but we rescale using the approximate Gaussian. The beam width are reported in table 5.1.

The achieved performance enter in the form of noise bandpowers, and the NETs are all computed as mentioned in the previous section, relying on the relative realism of NETlib.py rather than its absolute precision.

The results shown here and used for the reference design are scaled from BK14 achieved performance, using preliminary 220 GHz data. For the current analysis, which started after the work described here, I generated new parameters from BK15 (see `http://bicep.rc.fas.harvard.edu/CMB-S4/analysis_logbook/20190829_noise_params_DSR/`).

5.2.2.4 Theoretical model

For the signal part of the Fisher, which enters in μ and Σ of equation 5.1, we use a parametric model very close to the one from BK (see equation 4.11), except that we open the two decorrelation parameters. We end up with a 10-dimensional parameter space: r, A_{dust}, β_{d}, α_{d}, Δ_{d}, A_{sync}, β_{s}, α_{s}, Δ_{s}, ϵ. As in BK analysis fix $T_{\mathrm{d}} = 19.6$K. The parameter A_{L} (see equation 4.10), which just scales how much lensing signal remains after delensing, and its value is fixed depending on the depth of the lensing survey (see section 5.2.2.6).

For most fiducial models in the forecasting exercise, we fix $A_{\mathrm{dust}} = 4.25\mu K^2$ (best-fit value from BK14: see Keck Array and BICEP2 Collaborations 2016b) and $A_{\mathrm{sync}} = 3.8\mu K^2$ (95% upper limit from Keck Array and BICEP2 Collaborations 2016b). For the spatial and spectral variations, we use $\beta_{\mathrm{d}} = 1.59$ (Planck Collaboration XXII 2016), $\beta_{\mathrm{s}} = -3.10$ Fuskeland et al. 2014), $\alpha_{\mathrm{d}} = -0.42$; $\alpha_{\mathrm{s}} = -0.6$; and $\epsilon = 0$. We can also add 3% dust decorrelation $\Delta_{\mathrm{d}} = 0.97$ (Planck Collaboration Int. L 2016[5]) and $\Delta_{\mathrm{s}} = 0.9999$.

We use the same Gaussian prior as BK15 (0.11 for β_{d} and 0.3 for β_{s}, see table 4.1), with flat unbounded priors for the others.

5.2.2.5 Observing strategy

Since the noise spectra come from BK observations of a specific scanning strategy, we also need to rescale the BPCM when observing with different scanning strategies. In equation 5.5, we considered that the survey weight only depends on numbers of detector-year and NET, but if we were to observe a much larger region, the noise would of course be higher. This needs to be taken into account.

The scanning strategy will depend on our observation. As long as we do not detect any r signal, it is better to get deeper maps on a small area. If we start detecting signal with good significance, we should start observing wider to observe more modes, check uniformity, sample different regions, etc.

From South Pole, we can easily follow a small region of the sky with constant elevation scans as we do in BK. This allows to have very deep maps. From Chile, the Earth rotation results in a more extended survey[6]. With the large field of view of the SATs, and the continuous scanning strategy, we will have large edge tapers. There was an effort to find realistic scanning strategies for deep maps in Chile and at Pole[6], targeting 3% of the sky in the south, near the expected foreground minimum, as well as a slightly wider Pole map. These depth maps are shown in figure 5.5. Note that later on, we will treat differently what we call "Chile deep" region, which overlaps the "Pole deep", and "Chile shallow".

This non-uniform coverage of the sky means that we cannot simply consider that the survey weight is a constant value over the sky and that we should just rescale by the ratio of the observed part of the sky. The noise will increase in region with less observing time, while the signal is constant. This effect will also depend on the weighting we apply when computing the bandpowers. As briefly explained in section 3.5, in BK we apply a noise weighting during map making and hence during bandpower computation. In CMB-S4, the maps will not be noise dominated anymore (with a strong detection of foregrounds and lensing).

We will need to rescale the noise power spectrum from equation 5.5, by an additional

---

[5] We use squared logarithmic frequency evolution, and quadratic power spectrum, see equations A8 and A9 of CMB-S4 Collaboration 2020

[6] See `https://cmb-s4.uchicago.edu/wiki/index.php/Deeper_SAT_from_Chile_II` and links to the Pole versions. There are also links to videos with sky rotation.

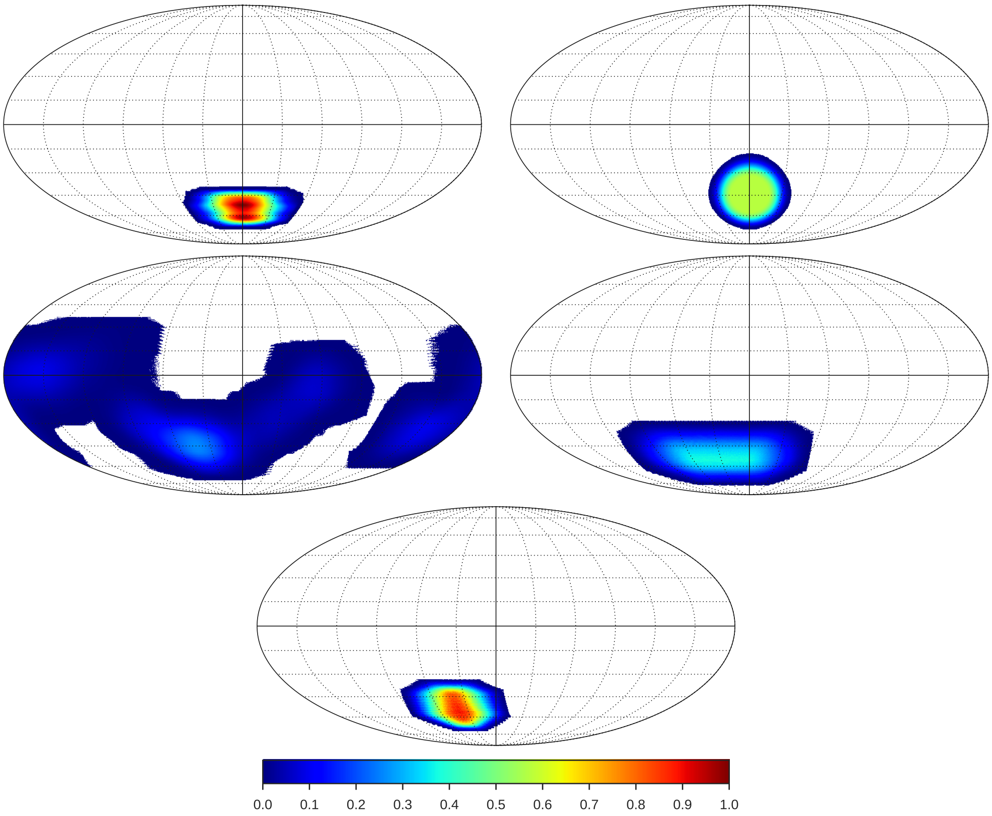

Figure 5.5: Detector-second hit patterns on the sky for small aperture telescope surveys. top left: the actual BICEP3 2017 hit pattern, top right: idealized circular pattern as used the map based analysis, middle left: simulated "Chile full" pattern, middle right: simulated "Pole wide" pattern, and bottom: simulated "Pole deep" pattern. Each pattern is normalized to the same sum and the color scales are equal. (The "Chile deep" and "Chile shallow" regions referred to in the text are sub regions of the "Chile full" pattern.).

ratio $f_{\mathrm{eff}}^{\mathrm{noise,S4}}/f_{\mathrm{eff}}^{\mathrm{noise,BK}}$ of effective sky fractions:

$$f_{\mathrm{eff}}^{\mathrm{noise}} = \frac{\Omega_{\mathrm{pix}}}{4\pi}\frac{\sum_i w_i^2 h_i^{-1} \sum_i h_i}{\sum_i w_i^2}, \tag{5.6}$$

where Ω_{pix} is the solid angle of a single pixel, w_i are the weights for pixel i, and h_i are the hit counts.

We then also need to rescale the signal, noise and cross components of the BPCM (see 4.3.1) by a ratio of the following factors to take into account the different number of modes observed[7]:

$$f_{\mathrm{sky}}^{\mathrm{noise}} = \frac{\Omega_{\mathrm{pix}}}{4\pi}\frac{(\sum_i w_i^2 h_i^{-1})^2}{\sum_i w_i^4 h_i^{-2}}, \tag{5.7}$$

$$f_{\mathrm{sky}}^{\mathrm{signal}} = \frac{\Omega_{\mathrm{pix}}}{4\pi}\frac{(\sum_i w_i^2)^2}{\sum_i w_i^4}, \tag{5.8}$$

$$f_{\mathrm{sky}}^{\mathrm{cross}} = \frac{\Omega_{\mathrm{pix}}}{4\pi}\frac{\sum_i w_i^2 \sum_i w_i^2 h_i^{-1}}{\sum_i w_i^4 h_i^{-1}}. \tag{5.9}$$

In the case of BK, as mentioned above, the weights are the inverse noise variance, i.e., $w_i = h_i$, whereas for CMB-S4, we include the signal too, which is provided by using the residual lensing and residual foreground after ILC. In table 5.2, we show these BPCM effective sky fractions in the simpler case of inverse noise weighting. For comparison, the BICEP2/Keck and BICEP3 values are (1.0, 1.3, 1.1) and (1.9, 2.7, 2.3) for signal, noise, and signal-cross-noise respectively.

Note that in section 5.2.2.4 we use a fixed foreground amplitude in the model. This is an acceptable simplification for this exercise when observing the small patch targeted to have low foregrounds. But in the maps above, some regions with high Galactic emission are also observed. Realistically, we would mask such regions when analyzing the maps. To assess this effect, we used masks based on a smoothed Planck 353 GHz polarized intensity map, keeping the cleanest 30% or 60% of the full sky (28% and 58% after apodization)[8]. We then used these masks to disregard some of the pixels, resulting in a degradation of the constraints on r. We also boost the remaining foreground in the "Chile shallow" case by a factor 3.22 with respect to the deep patch. This scaling is based on the dust amplitude measured in the map-based simulations for surveys observed from the South Pole or from Chile, using a map with spatially

---

[7] I showed this on a 1D toy model, where I compared what the power is for different weightings for signal and noise: `http://bicep.rc.fas.harvard.edu/CMB-S4/analysis_logbook/20181018_1Dmodel_tapering_study/`. For our case, here are some notes from Raphael Flauger: `http://bicep.rc.fas.harvard.edu/CMB-S4/analysis_logbook/20190430_sigmar_vs_r_forDSR/EffectiveFsky.pdf`.

[8] These masks can be seen overlaid on the `Commander` foreground maps in figure 8 here : `http://bicep.rc.fas.harvard.edu/CMB-S4/analysis_logbook/20190511_sigmar_vs_r_galcuts/`

Table 5.2: Effective sky fractions for signal, noise, and signal-cross-noise, as percentages, for the observation patterns shown in Figure 5.5, and the case of inverse noise-variance weighting (i.e., equations 5.7–5.9 with $w_i = h_i$). Here "SP" is the South Pole and "CH" is Chile. Note: the CH Shallow numbers appear larger than CH Full due to the effects of the weighting. We also report the fraction of sky with non zero coverage, $f_{\mathrm{sky}}^{\mathrm{non-zero}}$.

	SP deep	SP wide	CH deep	CH shallow	CH full
$f_{\mathrm{sky}}^{\mathrm{signal}}$	1.9	4.3	2.4	10	5.9
$f_{\mathrm{sky}}^{\mathrm{noise}}$	2.9	6.5	3.4	20	18
$f_{\mathrm{sky}}^{\mathrm{cross}}$	2.5	5.5	3.0	16	12
$f_{\mathrm{sky}}^{\mathrm{non-zero}}$	5.0	12	5.0	47	52

varying foregrounds based on *Planck* data[9].

Note that **in the early loop**, the problem was simplified by assuming a non-realistic uniform 3% coverage, and approximating BK to have a uniform 1% sky fraction, i.e. boosting the BPCM noise and cross terms by a factor 3^2 or 3 to take into account the higher noise and an overall factor of 3 to the whole BPCM to account for the observation of more modes. This is what we get if we use $w_i = h_i =$ constant in equations 5.6–5.9.

The realistic observing strategy scalings were only applied **in the late loop**.

5.2.2.6 Delensing

As we have seen in chapter 4, current measurements are close to reach the lensing floor, i.e. improving the noise sensitivity will not be useful if we do not perform delensing (see section 2.1.3.5).

In the early loop, we considered a high resolution LAT, assumed to have 1-arcminute resolution and noise performance equivalent to the 145 GHz channel from the SATs. Using a similar method than Smith et al. 2012 (figure 3 for instance), we could then translate a given map noise into a delensing efficiency. Technically this was done by scaling down A_L in our model. With the optimized distribution of detectors from table 5.1, we expect 90% efficiency of delensing, i.e. $A_L \simeq 0.1$.

This is of course a strong approximation, as we know that foreground will play a role at small scale (see for instance work on the effect of foregrounds on lensing reconstruction from Fabbian et al. 2019 and Beck et al. 2020). The LAT reference design, which was done independently from the SAT reference design described here,

---

[9] This is a crude estimate described here: `http://bicep.rc.fas.harvard.edu/CMB-S4/analysis_logbook/20181106_site_dep_fg_residual_bias/`

uses two LAT in Chile, which are designed for the other science goals of CMB-S4 and one LAT at Pole, specially tuned for delensing the B-modes (see tables 3-2 of CMB-S4 collaboration 2019b).

In the late loop, considering these LAT configurations, Raphael Flauger used an ILC to derive the noise levels after component separation, assuming that polarized foreground emission is dominated by Galactic synchrotron and thermal dust emission. Using the ILC noise power spectrum, we then forecast the performance expected for iterative EB delensing (Smith et al. 2012), as shown in figure 5.6.

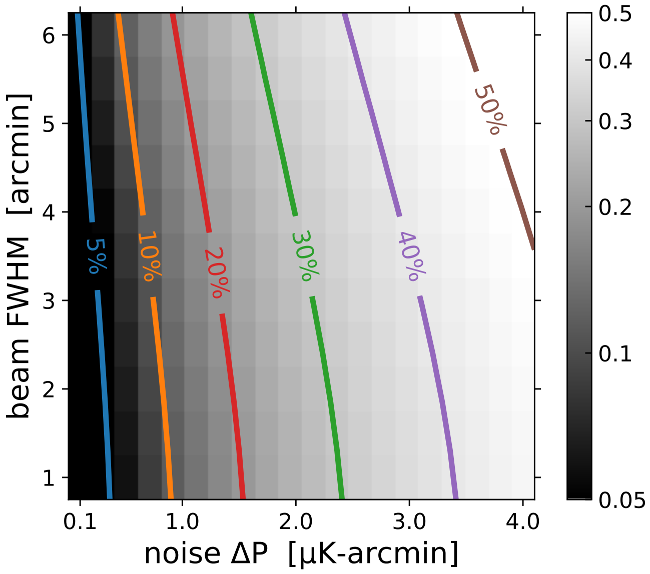

Figure 5.6: Forecasted lensing AL residual (grey scale plus colored contours as labeled) using the EB-only iterative delensing (Smith et al. 2012), as a function of the beam FWHM and noise level in Q and U. Figure from our appendix in CMB-S4 collaboration 2019b.

For the Chile LATs, covering roughly 70% of the sky, the ILC procedure predicts that 73% of the lensing power can be removed after 7 years of observation, while for the South Pole LAT covering the approximately 3% region, we expect to remove close to 90% of the lensing power. Note that we use here the same coverage map as in section 5.2.2.5. Note also that these numbers assume inverse noise-variance weighting rather than a weighting scheme that accounts for both signal and noise. For the reference design inverse noise variance weighting is typically suboptimal, and in all the forecasts presented below we employ weights that account for both signal (e.g., for r = 0 lensing residual after foreground removal) and noise. Even though, for the same survey, this leads to slightly higher noise and lensing residuals, the increase in the number of modes overall reduces the lensing sample variance contribution to $\sigma(r)$, especially for small, deep patches. In practice we determine the optimal weights iteratively, accounting for the effect on the SAT and LAT analyses and find rapid convergence.

5.2.2.7 Forecasting results and instrument definition and siting

We study 4 variations with $r = 0$ and one with $r = 0.003$, which are the two scenarios of our science goals, and with or without decorrelation.

Early loop: optimization of the detector distribution for the CDT report

In that iteration, using a more basic observing strategy scaling and lensing, Victor Buza and others used the machinery to optimize the distribution of effort per frequency. Effort being defined as the equivalent number of detector-year at 150 GHz, scaled as $(\nu/150\text{GHz})^2$ for other channels to approximate the focal plane area dependence, since this is the major cost driver. Using a 10-dimension steepest descent algorithm, they showed that it requires more than a million 150 GHz equivalent detector-years to reach our science goals, i.e. in four years with the distribution from table 5.1. This was the configuration reported to the National Science Fundation, in the CDT Lawrence et al. 2017. See CMB-S4 Collaboration 2020 for more details.

Late loop: optimization of the detector siting with realistic observing strategies for the reference design of the DSR

In that new iteration, we used the more evolved scalings, and a mapping of the detectors from table 5.1 into dichroic optics tubes was performed[10]. We varied the siting (Chile versus Pole), number of tubes, and observing strategies. In all cases, a delensing LAT at Pole concentrates coverage on a small patch of sky, while Chilean LATs provide delensing on larger sky areas. This ends up with the distribution shown in table 5.3, for a total of 18 SATs (+1 LAT) and 153232 (+135)[11] detectors during 7 years, i.e. 1073569 detector-years.

As we have seen in section 5.2.2.5, we have several observing strategy regions: "Pole deep", "Pole wide", "Chile full" and its subregions, "Chile deep", which overlaps with the "Pole deep" region, and call the remainder "Chile shallow". To obtain forecasts for the "Chile full" region, we make separate forecasts for each Chilean sub-region using the appropriate delensing level for that sub-region, we make the approximation of independence of the measured modes, and add the $\sigma(r)$ results in simple inverse quadrature. We can then get a forecast for the five different regions.

When we have a siting with telescopes both at Chile and Pole, and want the full forecasting, we mimic a joint analysis over the overlapping region by taking the sum of the "Pole deep" and "Chile deep" coverage maps and computing the corresponding

---

[10] Multiple possible options were explored here: `https://docs.google.com/spreadsheets/d/1B9A5-IYr1wAbOUgFDcnYv7qO_WXgXNU7EhlfBRqavm4`

[11] Note that we used 135 detector with a NET of 214 $\mu K\sqrt{s}$, whereas in table 3-2 of CMB-S4 collaboration 2019b, we have 160 detectors with NET = $438\mu K\sqrt{s}$. Not sure what happened here, but this should not make a big difference.

Property	LF		CF High		CF Low		HF	
Freq. (GHz)	30	40	85	145	95	155	220	270
Diameter (cm)	55	55	55	55	55	55	44	44
FWHM (')	72.8	72.8	25.5	25.5	22.7	22.7	13	13
Bandwidth	0.3	0.3	0.24	0.22	0.24	0.22	0.22	0.22
NET (μK$\sqrt{s}$)	177	224	270	238	309	331	747	1281
N_{det}	288	288	3524	3524	3524	3524	8438	8438
N_{tubes}	2		6		6		4	
N_{wafers}	24		72		72		36	
N_{wafers} total	204							
$N_{\text{detectors}}$	576	576	21144	21144	21144	21144	33752	33752
$N_{\text{detectors}}$ total	153232							
Data rate	1.7 TB/day							

Table 5.3: Small-aperture telescope (SAT) receiver properties, with center frequency, primary lens diameter, beam FWHM in arcminutes, fractional bandwidth of the beam, NET per detector, number of detector per optics tube, number of tubes and number of wafer (arrays of detectors). We also show the data rate for the 18 tubes.

weights and lensing residuals. We then add the "Chile shallow" results in inverse quadrature.

We also explore the possibility of unmodeled foreground residuals contributing residual power to the cleaned maps. We use the BK foreground minimum (95 GHz) at ell=80 as an estimate of the foregrounds amplitude and translating this into a r-equivalent. We then extrapolate it to the Chile observing strategy with a factor of 3 higher, as mentioned above. We also checked in map-based analysis (see next section) that the unmodeled foregrounds leave a bias that scales linearly with foreground amplitude. Here we consider the foreground residual to be 1% of the total foreground, which is of course a “soft” choice, and add it in quadrature to $\sigma(r)$. This is a crude estimate investigated in this posting: `http://bicep.rc.fas.harvard.edu/CMB-S4/analysis_logbook/20181106_site_dep_fg_residual_bias/` and should be improved in future iterations of the forecasting exercise.

The forecast will of course also depend on the fiducial value of r itself, and we use $r = 0$, 0.003, 0.01, and 0.03. We also check the case with and without decorrelation in the fiducial model.

Results of the forecasting that lead to the reference design

To have a detailed look at our effort, look at this posting and links therein.

In figure 5.7 we show a summary the forecast on $\sigma(r)$ for four values of r and the linear interpolation between these points, sampled on a high-resolution linearly-

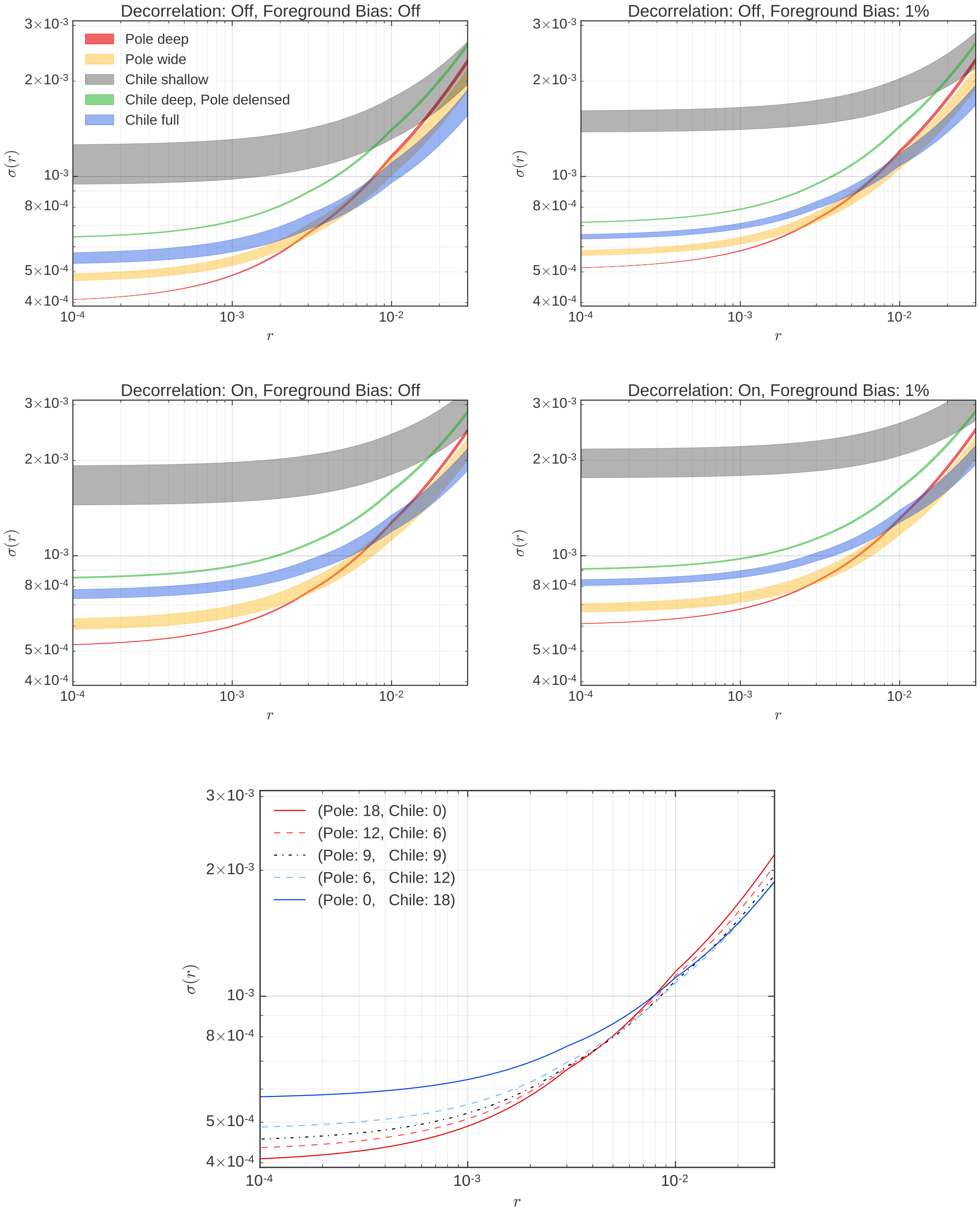

Figure 5.7: Constraints on r as a function of the value of r (see text).

spaced grid. We assume an instrument with 18 SAT optics tubes and an observation time of 7 years, with the five hit maps defined in section 5.2.2.5. Each band shows different Galactic cuts, based on *Planck* polarized foregrounds: the upper edge uses the cleanest 28% of the full sky, whereas the lower edge uses the 58% cleanest. We explore the effect of turning on foreground decorrelation in the forecasting. We also explore adding a foreground bias, in quadrature, with a 1% value of the equivalent r of the current foreground minimum of the BK15 data at $\ell = 80$. In the bottom plot, we show variations of the siting for 18 optics tubes. For clarity, we only show the forecast using the 28% cleanest polarized sky. Note that in the case where all the tubes are at Pole, we use the "Pole wide" pattern for $r \geq 0.01$ since it yields better constraints

Tables 5.4 to 5.7 contain forecasted $\sigma(r)$ for different sitings. We show results for two different variants: (1) with no marginalization over the decorrelation parameters and for the 28% cleanest polarized sky; and (2) the same as (1), but marginalizing over the foreground decorrelation parameters.

The first row represents the Pole only constraints. We consider both Pole wide and Pole deep strategy, and take the best case. In the case where we have a strong signal, it is better to go slightly wider, as can be seen in figure 5.7 for instance. The first column represents the Chile only constraints. Here we use the Chile full constraints, i.e. the quadrature sum of the deep, Pole delensed part and the shallow, Chile LAT delensed part, of the Chile narrow strategy.

For the cross-terms, we use the combined Pole delensed observing strategy constraints, to which we add the Chile delensed constraints in quadrature. We highlight the combinations that sum to 18 tubes in bold. We also present the 95%CL limit in the case where $r = 0$ and the significance of detection in the case where $r = 0.003$.

Remember that our goal is 0.001 at 95%CL and 0.003 at 5σ. Since the output of the Fisher framework is $\sigma(r)$, we need a way to convert these into our final statistics, taking into account the fact that the likelihood is non-Gaussian. Colin Bischoff introduced an ansatz for that step in this posting: `https://cmb-s4.uchicago.edu/wiki/index.php/Analytic_approximation_for_r_likelihood`. Here we use that ansatz to compute the marginalized r likelihood for every single Fisher case. We compute the 95%CL using the cumulative sum of the likelihood, and the significance of detection using the 0-to-peak ratio (see section 4.4.1). When we combine the Pole and Chile, we take the product of the two likelihoods and calculate our statistics. Here we make the approximation that the number of degrees of freedom (k in Colin's posting), just scales with $f_{\rm sky}^{\rm noise}$, with respect to the parameter fitted by Colin for the BICEP3 observation strategy. Note that these statistics correspond to a case where the signal in our patch peaks exactly at $r = 0$ or $r = 0.003$. Of course, a given realization of the a $r = 0.003$ sky, the likelihood will peak at different values. In a future analysis, one would want to then simulate this sample variance and compute the significance of detection and 95%CL for a bunch of simulation and report the median value.

As we anticipated in section 5.2.2.5, the survey strategy from the South Pole is always favored in the limit of small r, but for the highest r, the wider strategies are favored, the turning point between the two depends on our assumptions. Note that the delensing

Table 5.4: Combined $10^4 \times \sigma(r)$ values (*smaller* numbers are better), assuming $r = 0$ after 7 years of observation, keeping only the 28% cleanest part of the sky, assuming no decorrelation and an observing efficiency in Chile the same as at the South Pole. The bold cells conserve the 18 SAT optics tube count of the reference design, while non-bold cells explore other counts at the South Pole and in Chile.

Chile\Pole	0	6	9	12	18	30
0		6.3	5.0	4.5	**4.0**	3.5
6	12	5.5	4.7	**4.3**	3.9	3.5
9	8.7	5.1	**4.5**	4.1	3.8	3.4
12	7.1	**4.8**	4.3	4.0	3.7	3.4
18	**5.7**	4.4	4.1	3.8	3.6	3.3
30	4.4	3.9	3.7	3.6	3.4	3.2

Table 5.5: Same as table 5.4, but assuming additional foreground decorrelation parameters.

Chile\Pole	0	6	9	12	18	30
0		8.4	6.7	6.0	**5.2**	4.4
6	16	7.3	6.2	**5.6**	5.0	4.3
9	12	6.8	**5.9**	5.4	4.9	4.3
12	9.7	**6.4**	5.7	5.3	4.8	4.2
18	**7.8**	5.8	5.3	5.0	4.6	4.1
30	6.0	5.1	4.8	4.6	4.3	4.0

Table 5.6: Combined detection significance (*larger* numbers are better) for $r = 0.003$ after 7 years of observation, but same conditions as table 5.4.

Chile\Pole	0	6	9	12	18	30
0		3.7	4.5	4.9	**5.4**	6.0
6	2.2	4.3	4.8	**5.2**	5.6	6.1
9	3.0	4.6	**5.1**	5.4	5.8	6.3
12	3.6	**4.9**	5.3	5.6	5.9	6.4
18	**4.4**	5.3	5.7	5.9	6.2	6.6
30	5.4	6.0	6.2	6.4	6.6	6.9

Table 5.7: Same as table 5.6, but assuming additional foreground decorrelation paramaters.

Chile\Pole	0	6	9	12	18	30
0		3.0	3.6	4.0	**4.5**	5.1
6	1.7	3.5	3.9	**4.3**	4.7	5.2
9	2.3	3.7	**4.1**	4.4	4.8	5.3
12	2.8	**3.9**	4.3	4.6	4.9	5.4
18	**3.4**	4.3	4.6	4.8	5.1	5.6
30	4.2	4.8	5.0	5.2	5.5	5.8

requirements are stronger for the small surveys.

Short of active SATs that SO will deploy in the next few years, we here considered that the observations from Chile are equivalent from the ones from Pole. Since this has not been demonstrated, we also explored a pessimistic version where the yield at Chile is half the one at Pole, in similar tables that can be found in CMB-S4 collaboration 2019b.

5.2.3 Map-based forecasting

As described in section 5.2.1, during our forecasting loop, we use map-based data challenges to:

1. Check if our Fisher analysis prediction can be confirmed on a real analysis of simulated data.
2. Test the effect of non-Gaussianity and anisotropy of Galactic foregrounds.
3. Simulate residual systematics and propagate their effect to biases and uncertainty on r.
4. Check how inconsistencies between data and our parameter fits will impact r.
5. Study the foreground contamination on the lensing estimation[12].

Noise simulations

To produce map-level simulations it is necessary to translate the BICEP/Keck noise bandpowers into a prescription for map noise. We do this by fitting the BK N_ℓ's, after taking out the beam smoothing, to a white + 1/f model (similar to equation 3.10) :

$$N_{\ell,\mathrm{fit}} = N_0 \left(1 + \left(\frac{\ell}{\ell_{\mathrm{knee}}}\right)^{\gamma}\right). \tag{5.10}$$

We obtain the white noise level N_0, the slope γ, and ℓ_{knee} values. For the small-aperture data, we find $\ell_{\mathrm{knee}} = 50$ (60,60) with γ of -1.5 (-2.8,-2.9) for BK's 95 GHz (150,220). We can then scale the noise level using the same neighboring frequency mapping as in the previous sections, and scaling down the noise using NET and number of detector year as previously[13]. We assume a cut-off at $\ell_{\mathrm{min}} = 30$ below which we do not recover any information

To translate these map spectra to map noise levels, we must pick a specific scanning strategies. We then generated Gaussian noise realizations from the N_ℓ's using `HEALPix`'s synfast algorithm K. M. Gorski et al. 2005 at each band and divide by the square-root of the assumed coverage pattern such that the noise "blows up around the edge" as it does in real maps.

---

[12] The last point was only preliminary in DC-4 on which I worked, but is now a large effort of the forecasting working group.

[13] In http://bicep.rc.fas.harvard.edu/CMB-S4/analysis_logbook/20190829_noise_params_DSR/ we can see more details for DC5, after the late loop.

We studied three strategies: an ideal circular pattern with an effective coverage of 3% (04.00) seen in 5.5, a simulated realistic pattern for Chile (04b.00,an earlier version of "Chile Full" from above) and the achieved strategy from BICEP3 (04c.00). These can be seen here[14].

Note that in CMB-S4 collaboration 2019b and CMB-S4 Collaboration 2020 we only reported results for the nominal circular mask, which corresponds to what was forecasted in the early loop.

Signal simulations

We generate lensed CMB maps with and without r components using `HEALPix` (K. M. Gorski et al. 2005), from power spectra simulated with `CAMB` (A. Lewis et al. 2000). We then add models of the Galactic foregrounds[15]:

0. Simplistic Gaussian realizations of dust and synchrotron with power-law angular power spectra matching the amplitude observed in the BK field, and uniform Spectral Energy Distribution (SED)s from equations 2.18 and 2.17.
1. The PySM (Thorne et al. 2016) model `a1d1f1s1`, with (a) anomalous microwave emission (AME), (d) dust, (f) free-free, and (s) synchrotron. The numbers correspond to the models described in Thorne et al. 2016. Free-free and AME are assumed to be unpolarized in this model and thus do not affect the analysis in this paper.
2. The PySM model `a2d4f1s3`, where the models are also described in Thorne et al. 2016. These include 2% polarized AME, a two-temperature model for dust, and a curvature of the synchrotron SED.
3. The PySM model `a2d7f1s3`, where the dust model is a more sophisticated physical characterization of dust grains as described in Hensley 2015. Interestingly, this model does not necessarily conform to the modified blackbody SED.
4. Here we use model 3, but replace the dust component by a model that incorporates H1 column density maps as tracers of the dust intensity structures, and the polarization is generated using a phenomenological description of the Galactic magnetic field as described in Ghosh et al. 2017. The model is expanded beyond what is described in that paper to produce a modest amount of decorrelation of the dust emission pattern as a function of frequency motivated by the analysis of *Planck* data in Planck Collaboration 2017.
5. A toy model, similar to model 0, but with a strong dust decorrelation suggested in Figure 3 of Planck Collaboration 2017 ($\Delta^{217\times353} = 0.85$, at $\ell = 80$), scaled to other frequencies using the functional form given in appendix B of Vansyngel et al. 2017, with a linear scaling in ℓ. While such a model is not ruled out by current data, it appears to be very hard to produce such strong decorrelation in

---

[14] https://cmb-s4.uchicago.edu/wiki/index.php/Sims_with_nominal_Chile_and_Pole_masks

[15] See more extensive description on my posting: http://bicep.rc.fas.harvard.edu/CMB-S4/analysis_logbook/20181111_dc04_flatpriors/

physics-based models. Note also that as discussed in section 2.2.1, more recent paper do not observe such strong decorrelation.

6. A model based on MHD simulations Kritsuk et al. 2017 of the Galactic magnetic field, which naturally produces non-Gaussian correlated dust and synchrotron emission.
7. This model is a modified version of model 00, where the brightness of the dust varies across the sky. It does not include any decorrelation. It was mostly developed to study the effect of mask variations.
8. Model from Martinez-Solaeche et al. 2018. Using a three-dimensional model of polarized galactic dust emission that takes into account the variation of the dust density, spectral index and temperature along the line of sight, and contains randomly generated small scale polarization fluctuations. It is constrained to match observed dust emission on large scales, and match on smaller scales extrapolations of observed intensity and polarization power spectra. This model naturally produces dust decorrelation, due to a varying SED on the sky. It is also expected to produce a flattening at low frequency, as is briefly reported in figure 19 of the paper.
9. Model developed by Vansyngel et al. 2017. In this model, each layer has the same intensity (constrained by the Planck intensity map), but different magnetic field realizations. It produces Q and U maps by integrating along the line-of-sight over these multiple layers of magnetic fields. This magnetic field, contrary to the previous model, is simulated down to small turbulent scales, which produce more physically motivated non-Gaussian fluctuations in the maps (down to small scales).

We use 500 realizations for models 1, 2, 3, 4, 6, 50 for model 5, 150 for model 7, 8 and 9. Models 1 to 4 use the large-scale modes of the real sky as measured above the noise in the Planck data. Models 4, 6, 8 and 9, also contain a fixed signal realization. This means that these models are intrinsically "single-realization". Models 0, 5 and 7 have different seeds for each signal map and include the (Gaussian) sample variance. The PySM models fill in the small-scale structure with power-law Gaussian extrapolations, while models 4 and 6 naturally produce non-Gaussian small-scale structure. However, all of these models are consistent with current data, and the more complex models are not necessarily more accurate reflections of reality.

Note that in CMB-S4 collaboration 2019b and CMB-S4 Collaboration 2020 we only reported results for models 0 to 6.

Systematics simulations

Systematics are specific to a given instrument and by definition hard to model realistically. In our effort, we have taken the first steps in simulating various generic classes of additive systematic by injecting additional noise-like components into the maps and then re-analyzing them without knowledge of what was put in.

We used components that are both correlated and uncorrelated across frequency bands, with white, $1/\ell$, and white+$1/\ell$ spectra, at varying levels compared to single-frequency map noise or, for correlated cases, combined map noise. The leading-order effects of such components are usually mitigated via explicit modeling or filtering (see for instance section 3.4.1), but they may still produce map-level residuals. Examples of mechanisms in this class include bandpass mismatches, beam and pointing variations, calibration variations, cross-talk effects, half-wave-plate leakage, ground pickup, and readout irregularities. This study was mostly developed by Steve Palladino, Justin Willmert, Colin Bischoff before my time in Harvard: see `https://cmb-s4.uchicago.edu/wiki/index.php/Bias_on_r_from_additive_systematics`.

Delensing simulations

As mentioned above, a lot of the current effort from the working group at the time of writing is to evaluate our delensing capabilities on real map simulations with small scale signal, this was not yet available at the time of my analysis. Instead, we scaled down the lensing component in our maps by simply scaling A_L to 0.03, 0.1, 0.3 and 1.

Analysis of the simulated maps

We produced maps corresponding to the 1.2×10^6 150-GHz-equivalent detector-years, with the distribution of table 5.1. We then have two methods to analyze them, as introduced in section 5.2.1. The ILC, which only relies on the frequency dependence of the CMB and does not rely on assumptions about the spectral dependence of foreground components was ran by Raphael Flauger. I was running the other method, where we were using the parametric multicomponent likelihood method from BK, and computing the maximum likelihood. The model is the one described in section 4.3.

Results from map-based analysis

Using the parametric method, I studied many variations of the analysis:

- r=0 or $r = 0.003$.
- With our without decorrelation in the model.
- With A_L=0.03, 0.1, 0.3 or 1.
- For models 0 to 9.
- For the three strategies mentioned above (04.00, 04.00b, 04.00c).
- Varying the number of bandpower used in the analysis.
- Checking the effect of removing the 85 and 95 GHz channel the recovered bias on r, to study the effect of band splitting.
- Varying the priors on β and A_L.

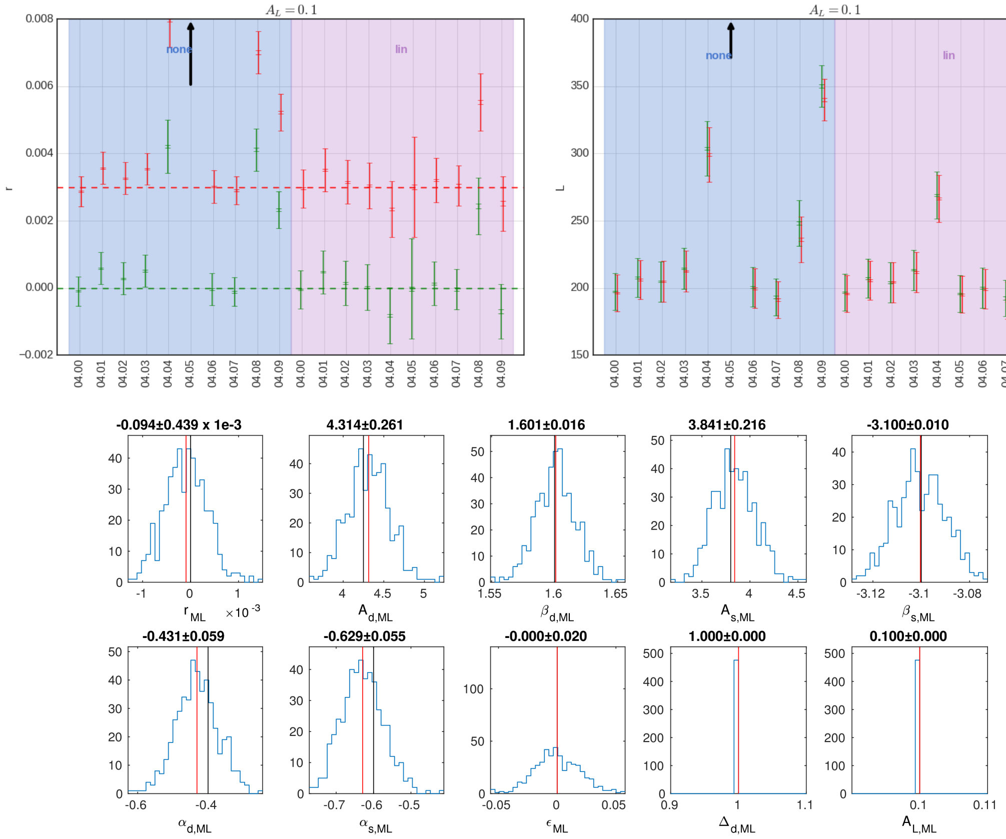

Figure 5.8: On top we show a summary of the results for r with $A_L = 0.1$, where A_L is fixed in the fit, and with a large flat prior on β_d. In red, the analysis of the simulations with $r = 0.003$, in green, the $r = 0$ case. On the left, the case without decorrelation in the parameterization, on the right, with linear-ℓ decorrelation. The outer error bars show the standard deviation σ of the N_{sim} simulations maximum likelihood results, and the inner error bars show the error on the mean: $\sigma/\sqrt{N_{\text{sim}}}$. In the middle we show L=-log(Likelihood). In the bottom, we show the maximum likelhood parameters histograms for models 04.00 without decorrelation. We plot the mean of the distribution as a red line, and the fiducial input value as a black line. We also report the mean and standard deviation of the distribution.

Reporting all these results in this manuscript would be unnecessary, but the interested reader can check my interactive postings here `https://cmb-s4.uchicago.edu/wiki/index.php/Simulation_and_Forecasting_Logbook`.

In figure 5.8, we show in the form of plots a subset of these results. Here we consider a 10% residual delensing ($A_L = 0.1$), for the 3% circular patch, we fix A_L in the fit and let β_d free[16].

Table 5.8: Results of two analysis methods applied to map-based simulation assuming the CMB-S4 CDT Report (Lawrence et al. 2017) configuration and our suite of sky models (DC4). All simulations assume an instrument configuration including a (high-resolution) 20 GHz channel, a survey of 3% of the sky with 1.2×10^6 150-GHz-equivalent detector-years, and $A_{\mathrm{L}} = 0.1$. Note that results for the last three simulations were not published in our papers because not studies but the ILC method. The bias reported for model 0 for the parametric method is described in the text.

		ILC		Parametric (decorr. off)		Parametric (decorr. on)	
r value	Sky model	$\sigma(r)^*$	r bias*	$\sigma(r)^*$	r bias*	$\sigma(r)^*$	r bias*
0	0	4.4	−0.2	4.4	0.2	5.7	0.3
	1	4.6	0.8	4.7	6.8	6.4	5.2
	2	4.7	0.7	4.8	3.8	6.5	1.9
	3	4.6	1.2	4.7	6.0	6.7	0.7
	4	6.5	4.8	7.9	43	8.3	−7.7
	5[a]	18	17	31	340	15	0.2
	6	4.8	−1.8	4.8	0.6	6.5	1.8
	7	.	.	4.2	−0.2	6.0	0.0
	8	.	.	6.3	42	8.5	25
	9	.	.	5.5	24	8.1	6.6
0.003	0	6.6	−0.7	6.2	0.3	8.1	0.4
	1	6.9	0.9	6.5	6.9	8.5	5.4
	2	6.5	−0.1	6.4	3.9	7.9	1.9
	3	7.0	1.4	6.6	6.7	8.7	0.9
	4	11	7.1	10	51	11	−6.2
	5[a]	23	17	34	350	17	0.4
	6	7.5	−0.2	7.1	1.4	8.6	2.5
	7	.	.	6.4	0.3	8.9	0.9
	8	.	.	8.3	41	11	26
	9	.	.	7.7	24	10	-4.5

[*] All these are in units of 10^{-4}

[a] An extreme decorrelation model—see Sect. 5.2.3. The parametric analysis includes a decorrelation parameter. No attempt is made in the ILC analysis to model decorrelation.

In table 5.8, we show results for model 0-6 together with the ILC ones and 7-9 for our method. For model 1-6, the bias is obtained by subtracting the mean of the model 00 (to account for the negligible algorithmic bias of $\simeq \pm 0.1 \times 10^{-4}$). For this Gaussian

---

[16] Other prior choices are shown in `http://bicep.rc.fas.harvard.edu/CMB-S4/analysis_logbook/20181111_dc04_flatpriors/`

foreground case, we report a bias based on the absolute value of the sample variance on the mean for $\simeq 500$ sims[17], which acknowledges statistical limitations exist even for closed-loop tests calibrated by Monte-Carlo simulations.

In general, we see that for $r = 0$ the simple Gaussian foreground model 0 gives $\sigma(r) \approx 5 \times 10^{-4}$, exactly as expected from the semi-analytic formalism. As we progress to the more complex foreground models, $\sigma(r)$ is generally in the range $5\text{–}8 \times 10^{-4}$. The level of biases is generally below 1σ for all the models.

However, the strong decorrelation in model 5, as well as the high-significance detection of decorrelation in the parametric analysis of model 4, do significantly increase $\sigma(r)$ and the level of bias. This is expected for the ILC and the parametric model without decorrelation fit, since they do not try to model it. When fitting for it, the bias disappears, but by construction information is lost and the error bars are larger. In fact if one believed in such a scenario, a different re-optimization to concentrate the sensitivity at closer-in (less decorrelated) frequencies would be called for.

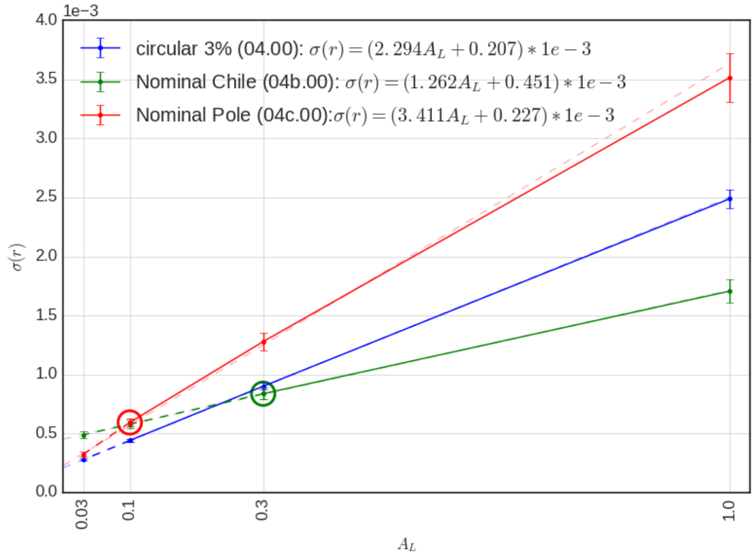

Figure 5.9: Evolution of $\sigma(r)$ as a function of A_L, for the 3 masks. In blue the circular 3% mask, in green the nominal Chile mask and red, the nominal Pole mask. The error bars are an estimate of the error on the standard deviation, estimated as $\sigma/\sqrt{N_{\text{sim}}}$. A linear fit is shown as a faded dashed line and the numbers are reported in the legend. We circled plausible delensing levels for Chile (A_L=0.3, in green) and for Pole (A_L=0.1, in red), to be checked with more realistic delensing simulations.

We also show in figure 5.9 how our constraining power changes with our delensing capabilities, for the three different studied masks. We focus here on the Gaussian

---

[17] For instance for the first line of table 5.8, we report a bias of $4.4/\sqrt{500} \simeq 0.2$

model 0, $r = 0$ and no decorrelation in the fit, but we studied all models and different priors in this posting. The slope is steeper for the Pole mask, meaning that the delensing is a great source of improvement. Overall, it seems like a Chile type observation mask would be a better choice if we do not delens. But once the necessary delensing is applied, a Pole mask performs better.

5.2.4 Conclusion of our forecasts

We have developed a Fisher forecasting tool based on real end-to-end on-sky achieved performance, and checked the predictions with map-based simulations of increasing complexity.

We showed that with a 3% sky fraction, we need 1.2×10^6 detector-years to achieve our science requirement of $\sigma(r) = 5 \times 10^{-4}$, 30% of this effort being dedicated to a delensing survey. The optimal distribution of detectors is shown in table 5.1.

We then generated simulations with noise and delensing levels corresponding to this distribution of detectors. We used different complex foregrounds to show that we can still recover our science goal, as seen in table 5.8.

This was then mapped into telescope tubes with a more realistic distribution based on possible technological designs, ending up in the distribution of table 5.3.

With this reference design, we complexified our framework to incorporate realistic scanning strategies to study different sitings (Chile versus Pole) and see if they could achieve our science goals in seven years. We found that the survey strategy from the South Pole is always favored in the limit of small r, defining our baseline for the reference design, with 18 tubes at pole. This requires a very good delensing which simple simulations seems to achieve. More work is currently ongoing within the collaboration to check this with realistic simulations. In the case of a detection, we could then expand our sky area and deploy telescopes in Chile, where larger sky fractions are achievable, requiring less delensing and observing more modes (if any).

5.2.5 Limitations of our forecasts

While we tried to stay rooted in achieved performance in our forecasts, there are a few limitations and caveat to keep in mind:

- We made the assumption that the CMB-S4 bolometer bath temperature will be 100mK, while BK's is at 250mK. This results in lower NETs than currently achieved. This is a departure from achieved performance.
- In the Fisher forecasting exercise, we assumed constant foreground amplitudes over the observed patches (except for the 3.22 factor in the "Chile shallow" part). Note that we also mask part of the sky based on polarized foreground cuts. This does not reflect the complexity of foreground and their treatment.
- Related to the previous point, our treatment assumes single fits for foreground parameters over the entire surveys (except "Chile shallow" versus "deep"), while

a more realistic treatment would refit the parameters for smaller subregions, which would reduce the sensitivities for larger sky fractions.

- Mitigating systematics and cleaning foreground to high precision will benefit more from high signal-to-noise per mode than from the raw number of modes measured. This would also penalize larger sky fractions.
- Whereas the different atmospheric conditions at the Pole site and Chile site induce different NETs, we currently use the mean of the two sites' NETs.
- Regarding delensing: while the SAT sensitivities have been increased substantially in our last iteration, the delensing levels have remained the same. This means signal-to-noise ratio per mode for the Pole is significantly above 1, and we can gain information by delensing more.
- In the current optimization of the detector allocation (which was fixed in the first iteration here), the delensing survey was assumed to have a NET equal to that of the 145 GHz channel, and no multi-frequency information was used at that level. More realistic optimization are being studied.
- The optimization that was used for the current 18 tubes configuration was based on a constant 3% sky fraction. We could now re-iterate the frequency allocation and the configuration for a given observing strategy.
- The filtering assumed in these forecasts is that of the BK published data, dominated by the polynomial filtering and the ground subtraction. While this is one of the main point in using performance based statistics, future analysis of the BA/SPO and SO data might improve this loss of modes. We will then update the forecasts.
- For wider patches, the neighbouring bandpowers should be less correlated, which is not modeled for now in the off diagonal terms of the bandpower covariance matrix. Only an overall scaling is applied.
- The survey strategies used here do not incorporate data cuts due to turnarounds, sun or moon cuts, etc., which make Chile surveys less efficient. Such simulations exist but need to be compared more carefully to actual survey strategies. The effect roughly cancels with the mean NET assumption.
- The NET used for now are for an elevation of 60 degrees[18], whereas in some of the strategies used here, we push down to 45 degrees. This is also something that could be incorporated but is a subdominant effect for now.
- The achieved performance forecasting is based on BK data at 95 and 150 (and 220 GHz for the survey weight), but extrapolated down to 30 GHz and up to 270 GHz. We could mitigate this using lower frequency observations (CLASS, QUIET, SPASS, or soon BICEP Array), and the latest BK bandpower statistics for higher frequencies.
- We are for now using a simple decorrelation model, with a quadratic ℓ-dependence. There is no data or model backing this choice up as far as I know. As our knowledge evolves, more physical models could be tested.

---

[18] We studied the effect of elevation here: `http://bicep.rc.fas.harvard.edu/CMB-S4/analysis_logbook/20190220_S4_NET_forecasts_III/`

- As mentioned in the section 5.2.2.7, the statistics reported in the tables for now assumes that the likelihood will peak exactly at the real r.
- For now we used the same depth maps for the LATs and SATs, whereas we expect a smaller tapering on the edges with the small beams of the large telescopes.

5.2.6 Development since 2020

Our analysis led to the reference design with seven years of observations using 18 tubes in SATs at Pole and a LAT for delensing. the National Science Foundation stated that this baseline was not supportable and asked for a an analysis of alternatives with a smaller cost, mostly reusing existing facilities at Pole and Chile.

In this process, people complexified the analysis by having different detector NETs at Pole and Chile, depending on PWV, elevation, etc. They also added new types of telescopes, and other site and frequency dependent efficiency factors. They used different models of foreground in the Fisher forecasting framework. Some of the results were presented in `https://indico.cmb-s4.org/event/34/`, but all require observation over more than 10 years and less margin on the science goals.

5.3 My contributions

When I joined the Kovac lab in Harvard, the first version of the Fisher forecasting code was written and used to produce the **the early Fisher forecast**. I worked mostly on the data challenge (DC4), using the maximum likelihood estimator adapted from BK analysis to study simulations. A first version was published in Lawrence et al. 2017. I was then deeply involved in **the late Fisher forecast**, central to two important publications (CMB-S4 collaboration 2019b and CMB-S4 Collaboration 2020).

Most of the work was first reported in our public wiki: `https://cmb-s4.uchicago.edu/wiki/index.php/Simulation_and_Forecasting_Logbook`, where my contribution can be seen in much greater detail.

Bibliography

[Abd+22] Elcio Abdalla et al. “Cosmology intertwined: A review of the particle physics, astrophysics, and cosmology associated with the cosmological tensions and anomalies”. In: *Journal of High Energy Astrophysics* 34 (June 2022), pp. 49–211. DOI: `10.1016/j.jheap.2022.04.002`. URL: `https://doi.org/10.1016%2Fj.jheap.2022.04.002` (cit. on p. 11).

[Arn+14] K. Arnold et al. “The Simons Array: expanding POLARBEAR to three multichroic telescopes”. In: vol. 9153. Aug. 2014, 91531F, 91531F. DOI: `10.1117/12.2057332`. URL: `https://doi.org/10.1117/12.2057332` (cit. on p. 82).

[Bar+14] D. Barkats et al. “DEGREE-SCALE COSMIC MICROWAVE BACKGROUND POLARIZATION MEASUREMENTS FROM THREE YEARS OF BICEP1 DATA”. In: *The Astrophysical Journal* 783.2 (Feb. 2014), p. 67. DOI: `10.1088/0004-637x/783/2/67`. URL: `https://doi.org/10.1088%2F0004-637x%2F783%2F2%2F67` (cit. on p. 64).

[Bau09] Daniel Baumann. “TASI Lectures on Inflation”. In: (2009). arXiv: `0907.5424 [hep-th]` (cit. on pp. 15, 21).

[BES20] Dominic Beck et al. “Impact of polarized galactic foreground emission on CMB lensing reconstruction and delensing of B-modes”. In: *JCAP* 2020.6, 030 (June 2020), p. 030. DOI: `10.1088/1475-7516/2020/06/030`. arXiv: `2001.02641 [astro-ph.CO]` (cit. on p. 93).

[Ben+14] B. A. Benson et al. “SPT-3G: A Next-Generation Cosmic Microwave Background Polarization Experiment on the South Pole Telescope”. In: *Proc. SPIE Int. Soc. Opt. Eng.* 9153 (2014), 91531P. DOI: `10.1117/12.2057305`. arXiv: `1407.2973 [astro-ph.IM]` (cit. on p. 82).

[Bey20] BeyondPlanck Collaboration. *BeyondPlanck I. Global Bayesian analysis of the Planck Low Frequency Instrument data*. 2020. DOI: `10.48550/ARXIV.2011.05609`. URL: `https://arxiv.org/abs/2011.05609` (cit. on pp. 19, 30, 34, 35).

[BIC15a] BICEP2 and SPIDER Collaborations. “ANTENNA-COUPLED TES BOLOMETERS USED IN BICEP2, Keck Array, AND SPIDER”. In: *The Astrophysical Journal* 812.2 (Oct. 2015), p. 176. DOI: `10.1088/0004-637x/812/2/176`. URL: `https://doi.org/10.1088%2F0004-637x%2F812%2F2%2F176` (cit. on p. 43).

[BIC14] BICEP2 Collaboration. "BICEP2. II. EXPERIMENT AND THREE-YEAR DATA SET". In: *The Astrophysical Journal* 792.1 (Aug. 2014), p. 62. DOI: `10.1088/0004-637x/792/1/62`. URL: `https://doi.org/10.1088%2F0004-637x%2F792%2F1%2F62` (cit. on pp. 54, 64).

[BIC15b] BICEP2 Collaboration. "BICEP2 III: Instrumental Systematics". In: *Astrophys. J.* 814.2 (2015), p. 110. DOI: `10.1088/0004-637X/814/2/110`. arXiv: `1502.00608 [astro-ph.IM]` (cit. on p. 56).

[BV89] R. Brandenberger and C. Vafa. "Superstrings in the early universe". In: *Nuclear Physics B* 316.2 (1989), pp. 391–410. ISSN: 0550-3213. DOI: `https://doi.org/10.1016/0550-3213(89)90037-0`. URL: `https://www.sciencedirect.com/science/article/pii/0550321389900370` (cit. on p. 17).

[BP17] Robert Brandenberger and Patrick Peter. "Bouncing Cosmologies: Progress and Problems". In: *Foundations of Physics* 47.6 (Feb. 2017), pp. 797–850. DOI: `10.1007/s10701-016-0057-0`. URL: `https://doi.org/10.1007%2Fs10701-016-0057-0` (cit. on p. 17).

[BRT15] Martin Bucher et al. "The binned bispectrum estimator: template-based and non-parametric CMB non-Gaussianity searches". In: (2015). DOI: `10.48550/ARXIV.1509.08107`. URL: `https://arxiv.org/abs/1509.08107` (cit. on p. 40).

[Buz19] Victor Buza. *Constraining Primordial Gravitational Waves Using Present and Future CMB Experiments.* 2019. URL: `https://dash.harvard.edu/handle/1/42029563` (cit. on pp. 64, 65).

[CL17] Julien Carron and Antony Lewis. "Maximum a posteriori CMB lensing reconstruction". In: *Phys. Rev.* **D** 96.6, 063510 (Sept. 2017), p. 063510. DOI: `10.1103/PhysRevD.96.063510`. arXiv: `1704.08230 [astro-ph.CO]` (cit. on p. 30).

[CLC17] Julien Carron et al. "Internal delensing of Planck CMB temperature and polarization". In: *JCAP* 2017.5, 035 (May 2017), p. 035. DOI: `10.1088/1475-7516/2017/05/035`. arXiv: `1701.01712 [astro-ph.CO]` (cit. on p. 30).

[Chl+21] J. Chluba et al. "New horizons in cosmology with spectral distortions of the cosmic microwave background". In: *Experimental Astronomy* 51.3 (May 2021), pp. 1515–1554. DOI: `10.1007/s10686-021-09729-5`. URL: `https://doi.org/10.1007%2Fs10686-021-09729-5` (cit. on p. 19).

[CGM04] Douglas Clowe et al. "Weak-Lensing Mass Reconstruction of the Interacting Cluster 1E 0657-558: Direct Evidence for the Existence of Dark Matter". In: *The Astrophysical Journal* 604.2 (Apr. 2004), pp. 596–603. DOI: `10.1086/381970`. URL: `https://doi.org/10.1086%2F381970` (cit. on p. 13).

[CMB20] CMB-S4 Collaboration. *CMB-S4: Forecasting Constraints on Primordial Gravitational Waves*. 2020. arXiv: `2008.12619 [astro-ph.CO]` (cit. on pp. 66, 84, 88, 90, 95, 101, 102, 109).

[CMB16] CMB-S4 collaboration. "CMB-S4 Science Book, First Edition". In: (2016). arXiv: `1610.02743 [astro-ph.CO]` (cit. on pp. 84, 85).

[CMB19a] CMB-S4 collaboration. *CMB-S4 Decadal Survey APC White Paper*. 2019. arXiv: `1908.01062 [astro-ph.IM]` (cit. on p. 84).

[CMB19b] CMB-S4 collaboration. *CMB-S4 Science Case, Reference Design, and Project Plan*. 2019. arXiv: `1907.04473 [astro-ph.IM]` (cit. on pp. 84, 94, 95, 100–102, 109).

[CMB22] CMB-S4 collaboration. "CMB-S4: Forecasting Constraints on Primordial Gravitational Waves". In: *The Astrophysical Journal* 926.1 (Feb. 2022), p. 54. DOI: `10.3847/1538-4357/ac1596`. URL: `https://doi.org/10.3847%2F1538-4357%2Fac1596` (cit. on p. 65).

[Col+14] Planck Collaboration et al. *Planck intermediate results. XXX. The angular power spectrum of polarized dust emission at intermediate and high Galactic latitudes*. 2014. arXiv: `1409.5738 [astro-ph.CO]` (cit. on p. 34).

[Col+19] Planck Collaboration et al. *Planck 2018 results. IX. Constraints on primordial non-Gaussianity*. 2019. arXiv: `1905.05697 [astro-ph.CO]` (cit. on p. 40).

[Cra46] H Cramér. *Mathematical Methods of Statistics*. 1st ed. Princeton U. Press, 1946 (cit. on p. 86).

[de 17] W. de Sitter. "Einstein's theory of gravitation and its astronomical consequences. Third paper". In: *Mon. Not. Roy. Astron. Soc.* 78 (Nov. 1917), pp. 3–28 (cit. on p. 10).

[DS20] S. Dodelson and F. Schmidt. *Modern Cosmology*. Elsevier Science, 2020. ISBN: 9780128159484. URL: `https://books.google.com/books?id=GGjfywEACAAJ` (cit. on pp. 21, 23, 24, 26).

[Duc+22] Gabriel Ducrocq et al. "Improved Gibbs samplers for cosmic microwave background power spectrum estimation". In: *Physical Review D* 105.10 (May 2022). DOI: `10.1103/physrevd.105.103501`. URL: `https://doi.org/10.1103%2Fphysrevd.105.103501` (cit. on p. 73).

[Ein05] A. Einstein. "Zur Elektrodynamik bewegter Körper[1]". In: *Annalen der Physik* 322 (1905), pp. 891–921. DOI: `10.1002/andp.19053221004` (cit. on p. 10).

---

[1] An English translation can be found here: `http://en.wikisource.org/wiki/On_the_Electrodynamics_of_Moving_Bodies_(1920_edition)`

[Ein15] A. Einstein. "Die Feldgleichungen der Gravitation [2]". In: *Sitzungsberichte der Königlich Preußischen Akademie der Wissenschaften (Berlin), Seite 844-847.* (1915), pp. 844–847 (cit. on p. 10).

[Ein16] A. Einstein. "Die Grundlage der allgemeinen Relativitätstheorie[3]". In: *Annalen der Physik* 354 (1916), pp. 769–822. DOI: `10.1002/andp.19163540702` (cit. on p. 10).

[Ein17] A. Einstein. "Kosmologische Betrachtungen zur allgemeinen Relativitätstheorie". In: *Sitzungsberichte der Königlich Preußischen Akademie der Wissenschaften (Berlin), Seite 142-152.* (1917), pp. 142–152 (cit. on p. 10).

[Eri+04] H. K. Eriksen et al. "Power Spectrum Estimation from High-Resolution Maps by Gibbs Sampling". en. In: *The Astrophysical Journal Supplement Series* 155.2 (Dec. 2004), pp. 227–241. ISSN: 0067-0049, 1538-4365. DOI: `10.1086/425219`. URL: `https://iopscience.iop.org/article/10.1086/425219` (visited on 02/19/2021) (cit. on pp. 54, 73).

[Eri+08] H. K. Eriksen et al. "Joint Bayesian Component Separation and CMB Power Spectrum Estimation". en. In: *The Astrophysical Journal* 676.1 (Mar. 2008), pp. 10–32. ISSN: 0004-637X, 1538-4357. DOI: `10.1086/525277`. URL: `https://iopscience.iop.org/article/10.1086/525277` (visited on 02/19/2021) (cit. on pp. 54, 73).

[Err+15] J. Errard et al. "MODELING ATMOSPHERIC EMISSION FOR CMB GROUND-BASED OBSERVATIONS". In: *The Astrophysical Journal* 809.1 (Aug. 2015), p. 63. DOI: `10.1088/0004-637x/809/1/63`. URL: `https://doi.org/10.1088%2F0004-637x%2F809%2F1%2F63` (cit. on p. 36).

[Ess+14] Thomas Essinger-Hileman et al. "CLASS: The Cosmology Large Angular Scale Surveyor". In: *Proc. SPIE Int. Soc. Opt. Eng.* 9153 (2014), p. 91531I. DOI: `10.1117/12.2056701`. arXiv: `1408.4788 [astro-ph.IM]` (cit. on p. 83).

[FLB19] Giulio Fabbian et al. "CMB lensing reconstruction biases in cross-correlation with large-scale structure probes". In: *JCAP* 2019.10, 057 (Oct. 2019), p. 057. DOI: `10.1088/1475-7516/2019/10/057`. arXiv: `1906.08760 [astro-ph.CO]` (cit. on p. 93).

[Fil+22] J. P. Filippini et al. "In-Flight Gain Monitoring of SPIDER's Transition-Edge Sensor Arrays". In: *Journal of Low Temperature Physics* (May 2022). DOI: `10.1007/s10909-022-02729-5`. URL: `https://doi.org/10.1007%2Fs10909-022-02729-5` (cit. on p. 45).

---

[2] An English translation can be found here: `http://en.wikisource.org/?curid=735695`

[3] An English translation can be found here: `http://en.wikisource.org/wiki/The_Foundation_of_the_Generalised_Theory_of_Relativity`

[FB02] Fabio Finelli and Robert Brandenberger. "Generation of a scale-invariant spectrum of adiabatic fluctuations in cosmological models with a contracting phase". In: *Physical Review D* 65.10 (May 2002). DOI: `10.1103/physrevd.65.103522`. URL: `https://doi.org/10.1103%2Fphysrevd.65.103522` (cit. on p. 17).

[Fix09] D. J. Fixsen. "THE TEMPERATURE OF THE COSMIC MICROWAVE BACKGROUND". In: *The Astrophysical Journal* 707.2 (Nov. 2009), pp. 916–920. DOI: `10.1088/0004-637x/707/2/916`. URL: `https://doi.org/10.1088%2F0004-637x%2F707%2F2%2F916` (cit. on p. 19).

[Fri22] A. Friedmann. "Über die Krümmung des Raumes". In: *Zeitschrift fur Physik* 10 (1922), pp. 377–386. DOI: `10.1007/BF01332580` (cit. on pp. 8, 10, 11).

[Fro10] Sebastien Fromenteau. "Modélisation et reconstruction et reconstruction des amas de galaxies dans le domaine optique/infrarouge". PhD thesis. Paris Diderot, 2010. URL: `http://www.theses.fr/2010PA077271` (cit. on p. 29).

[Fus+14] U. Fuskeland et al. "SPATIAL VARIATIONS IN THE SPECTRAL INDEX OF POLARIZED SYNCHROTRON EMISSION IN THE 9 yr WMAP SKY MAPS". In: *The Astrophysical Journal* 790.2 (July 2014), p. 104. DOI: `10.1088/0004-637x/790/2/104`. URL: `https://doi.org/10.1088%2F0004-637x%2F790%2F2%2F104` (cit. on pp. 66, 90).

[GV93] M. Gasperini and G. Veneziano. "Pre-big-bang in string cosmology". In: *Astroparticle Physics* 1.3 (July 1993), pp. 317–339. DOI: `10.1016/0927-6505(93)90017-8`. URL: `https://doi.org/10.1016%2F0927-6505%2893%2990017-8` (cit. on p. 17).

[Gel+17] Ronald Gelaro et al. "The Modern-Era Retrospective Analysis for Research and Applications, Version 2 (MERRA-2)". In: *Journal of Climate* 30.14 (2017), pp. 5419–5454. DOI: `10.1175/JCLI-D-16-0758.1`. eprint: `https://doi.org/10.1175/JCLI-D-16-0758.1`. URL: `https://doi.org/10.1175/JCLI-D-16-0758.1` (cit. on p. 87).

[Ger+20] Martina Gerbino et al. "Likelihood Methods for CMB Experiments". In: *Frontiers in Physics* 8 (Feb. 2020), p. 15. ISSN: 2296-424X. DOI: `10.3389/fphy.2020.00015`. URL: `https://www.frontiersin.org/article/10.3389/fphy.2020.00015/full` (visited on 02/19/2021) (cit. on p. 73).

[Gho+17] T. Ghosh et al. "Modelling and simulation of large-scale polarized dust emission over the southern Galactic cap using the GASS Hi data". In: *A & A* 601, A71 (May 2017), A71. DOI: `10.1051/0004-6361/201629829`. arXiv: `1611.02418` (cit. on p. 101).

[GT08] G. W. Gibbons and Neil Turok. “Measure problem in cosmology”. In: *Physical Review D* 77.6 (Mar. 2008). DOI: `10.1103/physrevd.77.063516`. URL: `https://doi.org/10.1103%2Fphysrevd.77.063516` (cit. on p. 17).

[Gje+15] E. Gjerløw et al. “Optimized Large-scale CMB Likelihood and Quadratic Maximum Likelihood Power Spectrum Estimation”. In: *The Astrophysical Journal Supp. Series* 221.1, 5 (Nov. 2015), p. 5. DOI: `10.1088/0067-0049/221/1/5`. arXiv: `1506.04273 [astro-ph.IM]` (cit. on p. 73).

[Gor+05] K. M. Gorski et al. “HEALPix - A Framework for high resolution discretization, and fast analysis of data distributed on the sphere”. In: *Astrophys. J.* 622 (2005), pp. 759–771. DOI: `10.1086/427976`. arXiv: `astro-ph/0409513 [astro-ph]` (cit. on pp. 32, 100, 101).

[Gor+99] Krzysztof M. Gorski et al. *The HEALPix Primer.* 1999. DOI: `10.48550/ARXIV.ASTRO-PH/9905275`. URL: `https://arxiv.org/abs/astro-ph/9905275` (cit. on pp. 21, 22).

[GTS09] J. Grain et al. “Polarized CMB power spectrum estimation using the pure pseudo-cross-spectrum approach”. en. In: *Physical Review D* 79.12 (June 2009), p. 123515. ISSN: 1550-7998, 1550-2368. DOI: `10.1103/PhysRevD.79.123515`. URL: `https://link.aps.org/doi/10.1103/PhysRevD.79.123515` (visited on 02/19/2021) (cit. on p. 73).

[Gut07] Alan H Guth. “Eternal inflation and its implications”. In: *Journal of Physics A: Mathematical and Theoretical* 40.25 (June 2007), pp. 6811–6826. DOI: `10.1088/1751-8113/40/25/s25`. URL: `https://doi.org/10.1088%2F1751-8113%2F40%2F25%2Fs25` (cit. on p. 17).

[Gut81] Alan H. Guth. “The Inflationary Universe: A Possible Solution to the Horizon and Flatness Problems”. In: *Phys.Rev.* D23 (1981), pp. 347–356. DOI: `10.1103/PhysRevD.23.347` (cit. on p. 15).

[Haj07] Amir Hajian. “Efficient cosmological parameter estimation with Hamiltonian Monte Carlo technique”. en. In: *Physical Review D* 75.8 (Apr. 2007), p. 083525. ISSN: 1550-7998, 1550-2368. DOI: `10.1103/PhysRevD.75.083525`. URL: `https://link.aps.org/doi/10.1103/PhysRevD.75.083525` (visited on 02/19/2021) (cit. on p. 73).

[Ham+22] J.-Ch. Hamilton et al. “QUBIC I: Overview and science program”. In: *Journal of Cosmology and Astroparticle Physics* 2022.04 (Apr. 2022), p. 034. DOI: `10.1088/1475-7516/2022/04/034`. URL: `https://doi.org/10.1088%2F1475-7516%2F2022%2F04%2F034` (cit. on p. 83).

[HL08] Samira Hamimeche and Antony Lewis. “Likelihood analysis of CMB temperature and polarization power spectra”. In: *Physical Review D* 77.10 (May 2008). DOI: `10.1103/physrevd.77.103013`. URL: `https://doi.org/10.1103%2Fphysrevd.77.103013` (cit. on pp. 64, 73).

[HL09] Samira Hamimeche and Antony Lewis. "Properties and use of CMB power spectrum likelihoods". en. In: *Physical Review D* 79.8 (Apr. 2009), p. 083012. ISSN: 1550-7998, 1550-2368. DOI: 10.1103/PhysRevD.79.083012. URL: https://link.aps.org/doi/10.1103/PhysRevD.79.083012 (visited on 02/19/2021) (cit. on p. 73).

[Hen+16] S. Henderson et al. "Advanced ACTPol Cryogenic Detector Arrays and Readout". In: *J. Low. Temp. Phys.* 184 (2016), p. 772. DOI: 10.1007/s10909-016-1575-z. arXiv: 1510.02809 [astro-ph.IM] (cit. on p. 82).

[Hen15] Brandon Hensley. "On the nature of interstellar grains". PhD thesis. Princeton University, 2015 (cit. on pp. 71, 101).

[Hiv+02] E. Hivon et al. "Master of the cosmic microwave background anisotropy power spectrum: a fast method for statistical analysis of large and complex cosmic microwave background data sets". In: *Astrophys. J.* 567 (2002), p. 2. DOI: 10.1086/338126. arXiv: astro-ph/0105302 [astro-ph] (cit. on pp. 46, 59, 73).

[Hu00] Wayne Hu. "Reionization Revisited: Secondary Cosmic Microwave Background Anisotropies and Polarization". In: *The Astrophysical Journal* 529.1 (Jan. 2000), pp. 12–25. DOI: 10.1086/308279. URL: https://doi.org/10.1086%2F308279 (cit. on p. 29).

[HW97] Wayne Hu and Martin White. "A CMB polarization primer". In: *New Astronomy* 2.4 (Oct. 1997), pp. 323–344. DOI: 10.1016/s1384-1076(97)00022-5. URL: https://doi.org/10.1016%2Fs1384-1076%2897%2900022-5 (cit. on pp. 21, 25).

[Hub29] E. Hubble. "A Relation between Distance and Radial Velocity among Extra-Galactic Nebulae". In: *Proceedings of the National Academy of Science* 15 (Mar. 1929), pp. 168–173. DOI: 10.1073/pnas.15.3.168 (cit. on p. 10).

[IS18] Anna Ijjas and Paul J Steinhardt. "Bouncing cosmology made simple". In: *Classical and Quantum Gravity* 35.13 (June 2018), p. 135004. DOI: 10.1088/1361-6382/aac482. URL: https://doi.org/10.1088%2F1361-6382%2Faac482 (cit. on p. 17).

[IS16] Anna Ijjas and Paul J. Steinhardt. "Inflation cheat sheet, unpublished". In: (2016). DOI: 10.1016/j.physletb.2014.07.012 (cit. on p. 16).

[ISL14] Anna Ijjas et al. "Inflationary schism". In: *Physics Letters B* 736 (Sept. 2014), pp. 142–146. DOI: 10.1016/j.physletb.2014.07.012. URL: https://doi.org/10.1016%2Fj.physletb.2014.07.012 (cit. on p. 16).

[JR75] F. James and M. Roos. "Minuit - a system for function minimization and analysis of the parameter errors and correlations". In: *Computer Physics Communications* 10.6 (Dec. 1975), pp. 343–367. DOI: 10.1016/0010-4655(75)90039-9 (cit. on p. 68).

[JLA04] J. Jewell et al. “Application of Monte Carlo Algorithms to the Bayesian Analysis of the Cosmic Microwave Background”. en. In: *The Astrophysical Journal* 609.1 (July 2004), pp. 1–14. ISSN: 0004-637X, 1538-4357. DOI: 10.1086/383515. URL: https://iopscience.iop.org/article/10.1086/383515 (visited on 02/19/2021) (cit. on p. 74).

[Jew+09] J. B. Jewell et al. “A Markov chain Monte Carlo algorithm for analysis of low signal-to-noise Cosmic Microwave Background data”. In: *The Astrophysical Journal* 697.1 (May 2009), pp. 258–268. ISSN: 0004-637X, 1538-4357. DOI: 10.1088/0004-637X/697/1/258. URL: https://iopscience.iop.org/article/10.1088/0004-637X/697/1/258 (visited on 02/19/2021) (cit. on pp. 73, 74, 76).

[JRT18] Gabriel Jung et al. “The bispectra of galactic CMB foregrounds and their impact on primordial non-Gaussianity estimation”. In: *Journal of Cosmology and Astroparticle Physics* 2018.11 (Nov. 2018), pp. 047–047. DOI: 10.1088/1475-7516/2018/11/047. URL: https://doi.org/10.1088%2F1475-7516%2F2018%2F11%2F047 (cit. on p. 41).

[KK15] Marc Kamionkowski and Ely D. Kovetz. “The Quest for B Modes from Inflationary Gravitational Waves”. In: (2015). arXiv: 1510.06042 [astro-ph.CO] (cit. on pp. 23, 29, 30).

[Kec16a] Keck Array and BICEP2 Collaborations. “BICEP2/KECK ARRAY. VII. MATRIX BASED E/BSEPARATION APPLIED TO BICEP2 AND THE KECK ARRAY”. In: *The Astrophysical Journal* 825.1 (June 2016), p. 66. DOI: 10.3847/0004-637x/825/1/66. URL: https://doi.org/10.3847%2F0004-637x%2F825%2F1%2F66 (cit. on p. 58).

[Kec16b] Keck Array and BICEP2 Collaborations. “Improved Constraints on Cosmology and Foregrounds from BICEP2 and Keck Array Cosmic Microwave Background Data with Inclusion of 95 GHz Band”. In: *Physical Review Letters* 116.3 (Jan. 2016). DOI: 10.1103/physrevlett.116.031302. URL: https://doi.org/10.1103%2Fphysrevlett.116.031302 (cit. on pp. 70, 90).

[Kec21] Keck Array and BICEP2 Collaborations. “Improved Constraints on Primordial Gravitational Waves using Planck , WMAP, and BICEP/ Keck Observations through the 2018 Observing Season”. In: *Physical Review Letters* 127.15 (Oct. 2021). DOI: 10.1103/physrevlett.127.151301. URL: https://doi.org/10.1103%2Fphysrevlett.127.151301 (cit. on pp. 57, 80).

[Kec+18] Keck Array and BICEP2 Collaborations et al. “Constraints on Primordial Gravitational Waves Using Planck , WMAP, and New BICEP2/Keck Observations through the 2015 Season”. In: *Physical Review Letters* 121.22 (Nov. 2018). DOI: 10.1103/physrevlett.121.221301. URL: https:

//doi.org/10.1103%2Fphysrevlett.121.221301 (cit. on pp. 57, 60, 63–67, 69, 70, 75, 77).

[Kec15] Keck Array, BICEP2 and Planck Collaborations. "Joint Analysis of BICEP2/Keck Array and Planck Data". In: *Physical Review Letters* 114.10 (Mar. 2015). DOI: 10.1103/physrevlett.114.101301. URL: https://doi.org/10.1103%2Fphysrevlett.114.101301 (cit. on pp. 64, 66).

[Ken79] A. Kendall M. amd Stuart. *Advanced Theory of Statistics*. 4th ed. Oxford U. Press, 1979 (cit. on p. 86).

[Kho+01] Justin Khoury et al. "Ekpyrotic universe: Colliding branes and the origin of the hot big bang". In: *Physical Review D* 64.12 (Nov. 2001). DOI: 10.1103/physrevd.64.123522. URL: https://doi.org/10.1103%2Fphysrevd.64.123522 (cit. on p. 17).

[Kno95] Lloyd Knox. "Determination of inflationary observables by cosmic microwave background anisotropy experiments". In: *Physical Review D* 52.8 (Oct. 1995), pp. 4307–4318. DOI: 10.1103/physrevd.52.4307. URL: https://doi.org/10.1103%2Fphysrevd.52.4307 (cit. on p. 60).

[KS02] Lloyd Knox and Yong-Seon Song. "A Limit on the detectability of the energy scale of inflation". In: *Phys. Rev. Lett.* 89 (2002), p. 011303. DOI: 10.1103/PhysRevLett.89.011303. arXiv: astro-ph/0202286 [astro-ph] (cit. on p. 30).

[Kos96] Arthur Kosowsky. "Cosmic Microwave Background Polarization". In: *Annals of Physics* 246.1 (Feb. 1996), pp. 49–85. DOI: 10.1006/aphy.1996.0020. URL: https://doi.org/10.1006%2Faphy.1996.0020 (cit. on p. 21).

[Kov+02] J. M. Kovac et al. "Detection of polarization in the cosmic microwave background using DASI". In: *Nature* 420.6917 (Dec. 2002), pp. 772–787. DOI: 10.1038/nature01269. URL: https://doi.org/10.1038%2Fnature01269 (cit. on pp. 25, 37).

[Kra+18] N. Krachmalnicoff et al. "S–PASS view of polarized Galactic synchrotron at 2.3 GHz as a contaminant to CMB observations". In: *Astronomy & Astrophysics* 618 (Oct. 2018), A166. DOI: 10.1051/0004-6361/201832768. URL: https://doi.org/10.1051%2F0004-6361%2F201832768 (cit. on pp. 35, 66).

[KUN17] A. G. Kritsuk et al. "The structure and statistics of interstellar turbulence". In: *New Journal of Physics* 19.6, 065003 (June 2017), p. 065003. DOI: 10.1088/1367-2630/aa7156. arXiv: 1705.01912 (cit. on pp. 71, 102).

[Lar+07] D. L. Larson et al. "Estimation of Polarized Power Spectra by Gibbs Sampling". en. In: *The Astrophysical Journal* 656.2 (Feb. 2007), pp. 653–660. ISSN: 0004-637X, 1538-4357. DOI: 10.1086/509802. URL: https://iopscience.iop.org/article/10.1086/509802 (visited on 02/19/2021) (cit. on p. 73).

[Law+17] Lawrence et al. *CMB-S4 Concept Definition Task Force Report*. https://www.nsf.gov/mps/ast/aaac/cmb_s4/report/CMBS4_final_report_NL.pdf. 2017. URL: https://www.nsf.gov/mps/ast/aaac/cmb_s4/report/CMBS4_final_report_NL.pdf (visited on 10/23/2017) (cit. on pp. 84, 95, 105, 109).

[LD00] A. Lazarian and B. T. Draine. "Resonance Paramagnetic Relaxation and Alignment of Small Grains". In: *The Astrophysical Journal* 536.1 (June 2000), pp. L15–L18. ISSN: 0004-637X. DOI: 10.1086/312720. URL: http://dx.doi.org/10.1086/312720 (cit. on p. 30).

[LP12] Henrietta S. Leavitt and Edward C. Pickering. "Periods of 25 Variable Stars in the Small Magellanic Cloud." In: *Harvard College Observatory Circular* 173 (Mar. 1912), pp. 1–3 (cit. on p. 10).

[Lem27] G. Lemaître. "Un Univers homogène de masse constante et de rayon croissant rendant compte de la vitesse radiale des nébuleuses extragalactiques". In: *Annales de la Societe Scietifique de Bruxelles* 47 (1927), pp. 49–59 (cit. on pp. 8, 10, 11).

[Lem31] G. Lemaître. "The Beginning of the World from the Point of View of Quantum Theory." In: *Nat.* 127 (May 1931), p. 706. DOI: 10.1038/127706b0 (cit. on p. 11).

[LC06] A Lewis and A Challinor. "Weak gravitational lensing of the CMB". In: *Physics Reports* 429.1 (June 2006), pp. 1–65. DOI: 10.1016/j.physrep.2006.03.002. URL: https://doi.org/10.1016%2Fj.physrep.2006.03.002 (cit. on p. 29).

[LCL00] A. Lewis et al. "Efficient Computation of Cosmic Microwave Background Anisotropies in Closed Friedmann-Robertson-Walker Models". In: *The Astrophysical Journal* 538.2 (Aug. 2000), pp. 473–476. DOI: 10.1086/309179. URL: https://doi.org/10.1086%2F309179 (cit. on pp. 31, 65, 101).

[LB02] Antony Lewis and Sarah Bridle. "Cosmological parameters from CMB and other data: a Monte- Carlo approach". In: *Phys. Rev.* D66 (2002), p. 103511. eprint: astro-ph/0205436 (cit. on pp. 66, 73).

[LW06] Yen-Ting Lin and Benjamin D. Wandelt. "A beginner's guide to the theory of CMB temperature and polarization power spectra in the line-of-sight formalism". In: *Astroparticle Physics* 25.2 (Mar. 2006), pp. 151–166. DOI: `10.1016/j.astropartphys.2005.12.002`. URL: `https://doi.org/10.1016%2Fj.astropartphys.2005.12.002` (cit. on p. 20).

[Lin82] Andrei D. Linde. "A New Inflationary Universe Scenario: A Possible Solution of the Horizon, Flatness, Homogeneity, Isotropy and Primordial Monopole Problems". In: *Phys.Lett.* B108 (1982), pp. 389–393. DOI: `10.1016/0370-2693(82)91219-9` (cit. on p. 15).

[Lor03] H. A. Lorentz. "Electromagnetic phenomena in a system moving with any velocity smaller than that of light". In: *Koninklijke Nederlandse Akademie van Wetenschappen Proceedings Series B Physical Sciences* 6 (1903), pp. 809–831. URL: `http://adsabs.harvard.edu/abs/1903KNAB....6..809L` (cit. on p. 10).

[MKD18] Gines Martinez-Solaeche et al. "A 3D model of polarized dust emission in the Milky Way". In: *Monthly Notices of the Royal Astronomical Society* 476.1 (Jan. 2018), pp. 1310–1330. DOI: `10.1093/mnras/sty204`. URL: `https://doi.org/10.1093%2Fmnras%2Fsty204` (cit. on p. 102).

[Max65] J. Clerk Maxwell. "A Dynamical Theory of the Electromagnetic Field". In: *Philosophical Transactions of the Royal Society of London* 155 (1865), pp. 459–512. DOI: `10.1098/rstl.1865.0008`. eprint: `http://rstl.royalsocietypublishing.org/content/155/459.full.pdf+html`. URL: `http://rstl.royalsocietypublishing.org/content/155/459.short` (cit. on p. 10).

[MM87] A. A. Michelson and E. W. Morley. "On the Relative Motion of the Earth and of the Luminiferous Ether". In: *Sidereal Messenger, vol. 6, pp.306-310* 6 (Nov. 1887), pp. 306–310. URL: `http://adsabs.harvard.edu/abs/1887SidM....6..306M` (cit. on p. 10).

[MHM04] Silvia Mollerach et al. "CMB polarization from secondary vector and tensor modes". In: *Physical Review D* 69.6 (Mar. 2004). DOI: `10.1103/physrevd.69.063002`. URL: `https://doi.org/10.1103%2Fphysrevd.69.063002` (cit. on p. 16).

[Mon+20] L. Moncelsi et al. *Receiver development for BICEP Array, a next-generation CMB polarimeter at the South Pole.* 2020. arXiv: `2012.04047 [astro-ph.IM]` (cit. on p. 82).

[MC81] Viatcheslav F. Mukhanov and G. V. Chibisov. "Quantum Fluctuation and Nonsingular Universe. (In Russian)". In: *JETP Lett.* 33 (1981), pp. 532–535 (cit. on p. 15).

[N A+16] and N. Aghanim et al. "Planck intermediate results". In: *Astronomy & Astrophysics* 596 (Dec. 2016), A107. DOI: `10.1051/0004-6361/201628890`. URL: `https://doi.org/10.1051%2F0004-6361%2F201628890` (cit. on p. 72).

[Nae12] Sigurd Kirkevold Naess. *Maximum likelihood analysis with the Q/U Imaging ExperimenT.* 2012. URL: `http://quiet.uchicago.edu/depot/pdf/thesis-2012_nass.pdf` (cit. on pp. 46, 48).

[Nag+17] J. M. Nagy et al. "A New Limit on CMB Circular Polarization from SPIDER". In: *The Astrophysical Journal* 844.2 (Aug. 2017), p. 151. ISSN: 1538-4357. DOI: `10.3847/1538-4357/aa7cfd`. URL: `http://dx.doi.org/10.3847/1538-4357/aa7cfd` (cit. on p. 21).

[Oor32] J. H. Oort. "The force exerted by the stellar system in the direction perpendicular to the galactic plane and some related problems". In: *Bulletin of the Astronomical Institutes of the Netherlands* 6 (Aug. 1932), p. 249. URL: `http://adsabs.harvard.edu/abs/1932BAN.....6..249O` (cit. on p. 13).

[P A+15] and P. A. R. Ade et al. "Planck intermediate results. XXII. Frequency dependence of thermal emission from Galactic dust in intensity and polarization". In: *Astronomy & Astrophysics* 576 (Apr. 2015), A107. DOI: `10.1051/0004-6361/201424088`. URL: `https://doi.org/10.1051%2F0004-6361%2F201424088` (cit. on p. 66).

[P A+16] and P. A. R. Ade et al. "Planck 2015 results". In: *Astronomy & Astrophysics* 594 (Sept. 2016), A2. DOI: `10.1051/0004-6361/201525818`. URL: `https://doi.org/10.1051%2F0004-6361%2F201525818` (cit. on p. 69).

[Pad+20] Ivan L. Padilla et al. "Two-year Cosmology Large Angular Scale Surveyor (CLASS) Observations: A Measurement of Circular Polarization at 40 GHz". In: *The Astrophysical Journal* 889.2 (Jan. 2020), p. 105. DOI: `10.3847/1538-4357/ab61f8`. URL: `https://doi.org/10.3847%2F1538-4357%2Fab61f8` (cit. on p. 21).

[Pai18] Scott Paine. *The am atmospheric model.* Mar. 2018. DOI: `10.5281/zenodo.1193646`. URL: `https://doi.org/10.5281/zenodo.1193646` (cit. on p. 88).

[Pee22] Phillip James E. Peebles. *Anomalies in Physical Cosmology.* 2022. DOI: `10.48550/ARXIV.2208.05018`. URL: `https://arxiv.org/abs/2208.05018` (cit. on p. 15).

[Pen89] Roger Penrose. "Difficulties with Inflationary Cosmology". In: *Annals of the New York Academy of Sciences* 571.1 (1989), pp. 249–264. DOI: `https://doi.org/10.1111/j.1749-6632.1989.tb50513.x`. eprint: `https://nyaspubs.onlinelibrary.wiley.com/doi/pdf/10.1111/j.1749-6632.1989.tb50513.x`. URL: `https://nyaspubs.onlinelibrary.`

wiley.com/doi/abs/10.1111/j.1749-6632.1989.tb50513.x (cit. on p. 16).

[Per+99] S. Perlmutter et al. “Measurements of Ω and Λ from 42 High-Redshift Supernovae”. In: *Ap. J.* 517 (June 1999), pp. 565–586. DOI: 10.1086/307221. eprint: astro-ph/9812133 (cit. on p. 13).

[Pla14a] Planck Collaboration. “Planck 2013 results. VIII. HFI photometric calibration and mapmaking”. In: *Astronomy & Astrophysics* 571 (Oct. 2014), A8. DOI: 10.1051/0004-6361/201321538. URL: https://doi.org/10.1051%2F0004-6361%2F201321538 (cit. on p. 46).

[Pla17] Planck Collaboration. “Planck intermediate results. L. Evidence of spatial variation of the polarized thermal dust spectral energy distribution and implications for CMB B-mode analysis”. In: *A & A* 599, A51 (Mar. 2017), A51. DOI: 10.1051/0004-6361/201629164. arXiv: 1606.07335 (cit. on p. 101).

[Pla20a] Planck Collaboration. “Planck 2018 results. IV. Diffuse component separation”. In: *A & A* 641, A4 (Sept. 2020), A4. DOI: 10.1051/0004-6361/201833881. arXiv: 1807.06208 [astro-ph.CO] (cit. on pp. 33, 35).

[Pla20b] Planck Collaboration. “Planck 2018 results. XI. Polarized dust foregrounds”. In: *A & A* 641, A11 (Sept. 2020), A11. DOI: 10.1051/0004-6361/201832618. arXiv: 1801.04945 [astro-ph.GA] (cit. on pp. 34, 66).

[Pla16a] Planck Collaboration Int. L. “Planck intermediate results. L. Evidence for spatial variation of the polarized thermal dust spectral energy distribution and implications for CMB *B*-mode analysis”. In: (2016). arXiv: 1606.07335 [astro-ph.CO] (cit. on pp. 34, 90).

[Pla16b] Planck Collaboration Int. XLVII. “Planck intermediate results. XLVII. Planck constraints on reionization history”. In: (2016). arXiv: 1605.03507 [astro-ph.CO] (cit. on p. 29).

[Pla15a] Planck Collaboration X. “Planck 2015 results. X. Diffuse component separation: Foreground maps”. In: (2015). arXiv: 1502.01588 [astro-ph.CO] (cit. on p. 30).

[Pla16c] Planck Collaboration XII. “Planck 2015 results. XIII. Cosmological parameters”. In: *Astron. Astrophys.* 594 (2016), A13. DOI: 10.1051/0004-6361/201525830. arXiv: 1502.01589 [astro-ph.CO] (cit. on p. 72).

[Pla15b] Planck Collaboration XVII. “Planck 2015 results. XVII. Constraints on primordial non-Gaussianity”. In: (2015). arXiv: 1502.01592 [astro-ph.CO] (cit. on p. 40).

[Pla16d] Planck Collaboration XXII. “Planck 2015 results. XXII. A map of the thermal Sunyaev-Zeldovich effect”. In: *A & A* 594, A22 (Sept. 2016), A22. DOI: 10.1051/0004-6361/201525826. arXiv: 1502.01596 (cit. on p. 90).

[Pla14b] Planck Collaboration XXIV. “Planck 2013 Results. XXIV. Constraints on primordial non-Gaussianity”. In: *Astron. Astrophys.* 571 (2014), A24. DOI: `10.1051/0004-6361/201321554`. arXiv: `1303.5084 [astro-ph.CO]` (cit. on p. 40).

[Poi06] Henri Poincaré. “Sur la dynamique de l’électron”. In: *Rendiconti del circolo matematico di Palermo* 21 (1906), pp. 129–176 (cit. on p. 10).

[Pol+17] Davide Poletti et al. “Making maps of cosmic microwave background polarization for B-mode studies: the POLARBEAR example”. In: *Astronomy & Astrophysics* 600 (Mar. 2017), A60. DOI: `10.1051/0004-6361/201629467`. URL: `https://doi.org/10.1051%2F0004-6361%2F201629467` (cit. on p. 46).

[Rac+16] B. Racine et al. “Cosmological Parameters from CMB Maps without Likelihood Approximation”. In: *The Astrophysical Journal* 820.1 (Mar. 2016), p. 31. ISSN: 1538-4357. DOI: `10.3847/0004-637X/820/1/31`. URL: `https://iopscience.iop.org/article/10.3847/0004-637X/820/1/31` (visited on 02/19/2021) (cit. on pp. 73, 75).

[Rac14] Benjamin Racine. “Étude des non-gaussianités dans les données du satellite Planck”. Theses. Université Paris Diderot, Sept. 2014. URL: `https://tel.archives-ouvertes.fr/tel-01420188` (cit. on pp. 11, 40).

[Rah+14] A. S. Rahlin et al. “Pre-flight integration and characterization of the SPIDER balloon-borne telescope”. In: *SPIE Proceedings*. Ed. by Wayne S. Holland and Jonas Zmuidzinas. SPIE, July 2014. DOI: `10.1117/12.2055683`. URL: `https://doi.org/10.1117%2F12.2055683` (cit. on p. 39).

[Rah16] Alexandra Rahlin. *The First Flight of the SPIDER Balloon-Borne Telescope*. 2016. URL: `https://dataspace.princeton.edu/handle/88435/dsp01tm70mx65g` (visited on 09/30/2010) (cit. on pp. 39, 44, 45, 49).

[RF+98] A. G. Riess, A. V. Filippenko, et al. “Observational Evidence from Supernovae for an Accelerating Universe and a Cosmological Constant”. In: *Astron. J.* 116 (Sept. 1998), pp. 1009–1038. DOI: `10.1086/300499`. eprint: `astro-ph/9805201` (cit. on p. 13).

[Rio02] Antonio Riotto. *Inflation and the Theory of Cosmological Perturbations*. 2002. DOI: `10.48550/ARXIV.HEP-PH/0210162`. URL: `https://arxiv.org/abs/hep-ph/0210162` (cit. on p. 15).

[Rob35] H. P. Robertson. “Kinematics and World-Structure”. In: *Ap. J.* 82 (Nov. 1935), p. 284. DOI: `10.1086/143681` (cit. on pp. 8, 11).

[RTF78] V. C. Rubin et al. “Extended rotation curves of high-luminosity spiral galaxies. IV - Systematic dynamical properties, SA through SC”. In: *Ap. J. Lett.* 225 (Nov. 1978), pp. L107–L111. DOI: `10.1086/182804` (cit. on p. 13).

[RL85] George B Rybicki and Alan P Lightman. *Radiative Processes in Astrophysics.* New York, NY: Wiley, 1985. DOI: 10.1002/9783527618170. URL: https://cds.cern.ch/record/847173 (cit. on p. 34).

[SH04] Uros Seljak and Christopher M. Hirata. "Gravitational lensing as a contaminant of the gravity wave signal in CMB". In: *Phys.Rev.* D69 (2004), p. 043005. DOI: 10.1103/PhysRevD.69.043005. arXiv: astro-ph/0310163 [astro-ph] (cit. on p. 30).

[SZ96] Uros Seljak and Matias Zaldarriaga. "A Line-of-Sight Integration Approach to Cosmic Microwave Background Anisotropies". In: *The Astrophysical Journal* 469 (Oct. 1996), p. 437. ISSN: 1538-4357. DOI: 10.1086/177793. URL: http://dx.doi.org/10.1086/177793 (cit. on p. 23).

[SS17] C. Sheehy and A. Slosar. "No evidence for dust B-mode decorrelation in Planck data". In: *ArXiv e-prints* (Sept. 2017). arXiv: 1709.09729 (cit. on p. 34).

[Sim+16] S. M. Simon et al. "The design and characterization of wideband spline-profiled feedhorns for Advanced ACTPol". In: *Millimeter, Submillimeter, and Far-Infrared Detectors and Instrumentation for Astronomy VIII.* Vol. 9914. Proc. SPIE. July 2016, 991416, p. 991416. DOI: 10.1117/12.2233603 (cit. on p. 82).

[Sli15] V. M. Slipher. "Spectrographic Observations of Nebulae". In: *Popular Astronomy* 23 (Jan. 1915), pp. 21–24 (cit. on p. 10).

[Smi+12] Kendrick M Smith et al. "Delensing CMB polarization with external datasets". In: *Journal of Cosmology and Astroparticle Physics* 2012.06 (June 2012), pp. 014–014. DOI: 10.1088/1475-7516/2012/06/014. URL: https://doi.org/10.1088%2F1475-7516%2F2012%2F06%2F014 (cit. on pp. 93, 94).

[Smo+92] G. F. Smoot et al. "Structure in the COBE Differential Microwave Radiometer First-Year Maps". In: *Ap. J. Lett.* 396 (Sept. 1992), p. L1. DOI: 10.1086/186504 (cit. on p. 19).

[Sob+21] J. A. Sobrin et al. *The Design and Integrated Performance of SPT-3G.* 2021. arXiv: 2106.11202 [astro-ph.IM] (cit. on p. 82).

[SPI21] SPIDER Collaboration. "A Constraint on Primordial *B*-Modes from the First Flight of the SPIDER Balloon-Borne Telescope". In: *arXiv e-prints*, arXiv:2103.13334 (Mar. 2021), arXiv:2103.13334. arXiv: 2103.13334 [astro-ph.CO] (cit. on pp. 40, 46).

[Sta80] Alexei A. Starobinsky. "A New Type of Isotropic Cosmological Models Without Singularity". In: *Phys.Lett.* B91 (1980), pp. 99–102. DOI: 10.1016/0370-2693(80)90670-X (cit. on p. 15).

[Ste+16] N. Stebor et al. “The Simons Array CMB polarization experiment”. In: *Millimeter, Submillimeter, and Far-Infrared Detectors and Instrumentation for Astronomy VIII*. Ed. by Wayne S. Holland and Jonas Zmuidzinas. Vol. 9914. Society of Photo-Optical Instrumentation Engineers (SPIE) Conference Series. July 2016, 99141H, 99141H. DOI: `10.1117/12.2233103` (cit. on p. 82).

[Suz+16] A. Suzuki et al. “The Polarbear-2 and the Simons Array Experiments”. In: *Journal of Low Temperature Physics* 184.3-4 (Jan. 2016), pp. 805–810. DOI: `10.1007/s10909-015-1425-4`. URL: `https://doi.org/10.1007%2Fs10909-015-1425-4` (cit. on p. 82).

[Sva+20] T. L. Svalheim et al. *BeyondPlanck XV. Polarized foreground emission between 30 and 70 GHz*. 2020. arXiv: `2011.08503 [astro-ph.CO]` (cit. on p. 30).

[TAH08] J. F. Taylor et al. “Fast optimal CMB power spectrum estimation with Hamiltonian sampling”. en. In: *Monthly Notices of the Royal Astronomical Society* 389.3 (Sept. 2008), pp. 1284–1292. ISSN: 00358711, 13652966. DOI: `10.1111/j.1365-2966.2008.13630.x`. URL: `https://academic.oup.com/mnras/article-lookup/doi/10.1111/j.1365-2966.2008.13630.x` (visited on 02/19/2021) (cit. on p. 73).

[Teg97] Max Tegmark. “CMB mapping experiments: A designer’s guide”. In: *Physical Review D* 56.8 (Oct. 1997), pp. 4514–4529. DOI: `10.1103/physrevd.56.4514`. URL: `https://doi.org/10.1103%2Fphysrevd.56.4514` (cit. on pp. 60, 62).

[TE96] Max Tegmark and George Efstathiou. “A method for subtracting foregrounds from multi-frequency cmb sky maps”. In: *Mon. Not. Roy. Astron. Soc.* 281 (1996), p. 1297. DOI: `10.1093/mnras/281.4.1297`. arXiv: `astro-ph/9507009 [astro-ph]` (cit. on p. 85).

[TO00] Max Tegmark and Angelica de Oliveira-Costa. “How to measure CMB polarization power spectra without losing information”. In: *Phys.Rev.D64:063001,2001* (Dec. 2000). DOI: `10.1103/PhysRevD.64.063001`. arXiv: `astro-ph/0012120 [astro-ph]` (cit. on p. 73).

[TTH97] Max Tegmark et al. “Karhunen-Loève Eigenvalue Problems in Cosmology: How Should We Tackle Large Data Sets?” In: *Ap. J.* 480.1 (May 1997), pp. 22–35. DOI: `10.1086/303939`. arXiv: `astro-ph/9603021 [astro-ph]` (cit. on p. 86).

[The18] The Simons Observatory Collaboration. “The Simons Observatory: Science goals and forecasts”. In: *ArXiv e-prints* (Aug. 2018). arXiv: `1808.07445` (cit. on p. 83).

[Tho19] Harald Thommesen. *Observing the CMB Sky with GreenPol, SPIDER and Planck*. 2019. URL: `https://www.duo.uio.no/handle/10852/70416?locale-attribute=en` (visited on 09/30/2010) (cit. on p. 54).

[Tho+16] Ben Thorne et al. "The Python Sky Model: software for simulating the Galactic microwave sky". In: (2016). arXiv: `1608.02841 [astro-ph.CO]` (cit. on pp. 71, 101).

[TN17] Alexandre Le Tiec and Jérôme Novak. "Theory of Gravitational Waves". In: *An Overview of Gravitational Waves*. WORLD SCIENTIFIC, Feb. 2017, pp. 1–41. DOI: `10.1142/9789813141766_0001`. URL: `https://doi.org/10.1142%2F9789813141766_0001` (cit. on pp. 25, 27).

[Tor+22] S.A. Torchinsky et al. "QUBIC III: Laboratory characterization". In: *Journal of Cosmology and Astroparticle Physics* 2022.04 (Apr. 2022), p. 036. DOI: `10.1088/1475-7516/2022/04/036`. URL: `https://doi.org/10.1088%2F1475-7516%2F2022%2F04%2F036` (cit. on p. 83).

[UWB19] Robin E Upham et al. "Exact joint likelihood of pseudo-Cℓ estimates from correlated Gaussian cosmological fields". In: *Monthly Notices of the Royal Astronomical Society* 491.3 (Nov. 2019), pp. 3165–3181. DOI: `10.1093/mnras/stz3225` (cit. on p. 73).

[Van+17] Flavzouille Vansyngel et al. "Statistical simulations of the dust foreground to cosmic microwave background polarization". In: *A & A* 603, A62 (July 2017), A62. DOI: `10.1051/0004-6361/201629992`. arXiv: `1611.02577` (cit. on pp. 101, 102).

[Wal37] A. G. Walker. "On Milne's Theory of World-Structure". In: *Proceedings of the London Mathematical Society* s2-42.1 (1937), pp. 90–127. DOI: `10.1112/plms/s2-42.1.90`. eprint: `http://plms.oxfordjournals.org/content/s2-42/1/90.full.pdf+html`. URL: `http://plms.oxfordjournals.org/content/s2-42/1/90.short` (cit. on pp. 8, 11).

[WLL04] Benjamin D. Wandelt et al. "Global, exact cosmic microwave background data analysis using Gibbs sampling". en. In: *Physical Review D* 70.8 (Oct. 2004), p. 083511. ISSN: 1550-7998, 1550-2368. DOI: `10.1103/PhysRevD.70.083511`. URL: `https://link.aps.org/doi/10.1103/PhysRevD.70.083511` (visited on 02/19/2021) (cit. on p. 73).

[Wil38] S. S. Wilks. "The Large-Sample Distribution of the Likelihood Ratio for Testing Composite Hypotheses". In: *The Annals of Mathematical Statistics* 9.1 (1938), pp. 60–62. DOI: `10.1214/aoms/1177732360`. URL: `https://doi.org/10.1214/aoms/1177732360` (cit. on p. 68).

[Wil19] Justin Willmert. *Constraining Inflationary B-modes with the BICEP/Keck Array Telescopes*. 2019. URL: `https://conservancy.umn.edu/handle/11299/211821` (visited on 09/30/2010) (cit. on pp. 37, 38, 45, 54, 56, 58, 59).

[Wra+09] Darren Wraith et al. “Estimation of cosmological parameters using adaptive importance sampling”. en. In: *Physical Review D* 80.2 (July 2009), p. 023507. ISSN: 1550-7998, 1550-2368. DOI: `10.1103/PhysRevD.80.023507`. URL: `https://link.aps.org/doi/10.1103/PhysRevD.80.023507` (visited on 02/18/2021) (cit. on p. 73).

[You18] Edward Young. “Studying the cosmic microwave background with Spider’s first flight”. PhD thesis. Princeton University, New Jersey, Jan. 2018. URL: `https://ui.adsabs.harvard.edu/abs/2018PhDT........13Y` (cit. on p. 44).

[ZS97] Matias Zaldarriaga and Uroš Seljak. “All-sky analysis of polarization in the microwave background”. In: *Physical Review D* 55.4 (Feb. 1997), pp. 1830–1840. ISSN: 1089-4918. DOI: `10.1103/physrevd.55.1830`. URL: `http://dx.doi.org/10.1103/PhysRevD.55.1830` (cit. on p. 23).

[Zon+19] Andrea Zonca et al. “healpy: equal area pixelization and spherical harmonics transforms for data on the sphere in Python”. In: *Journal of Open Source Software* 4.35 (Mar. 2019), p. 1298. DOI: `10.21105/joss.01298`. URL: `https://doi.org/10.21105/joss.01298` (cit. on p. 32).

[Zwi33] F. Zwicky. “Die Rotverschiebung von extragalaktischen Nebeln [4]”. In: *Helvetica Physica Acta* 6 (1933), pp. 110–127 (cit. on p. 13).

---

[4] An English translation of part of this manuscript can be found here: `http://arxiv.org/pdf/astro-ph/9904251.pdf`